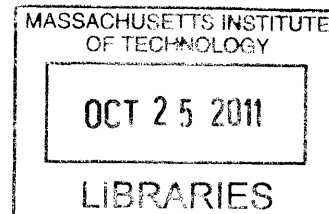


**The Effect of Trivalent Cations on the Major Lower
Mantle Silicates**

by

Krystle Carina Catalli



Submitted to the Department of Earth, Atmospheric & Planetary Sciences
in partial fulfillment of the requirements for the degree of

Doctor of Philosophy in Geophysics

at the

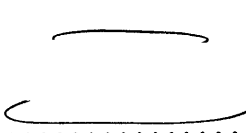
MASSACHUSETTS INSTITUTE OF TECHNOLOGY

June 2011

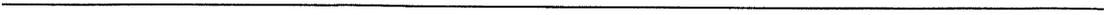
ARCHIVES

© Massachusetts Institute of Technology 2011. All rights reserved.

Author 
Department of Earth, Atmospheric & Planetary Sciences
March 17, 2011

Certified by  
Sang-Heon Shim
Associate Professor
Thesis Supervisor

Accepted by 
Maria Zuber
Head of the Department of Earth, Atmospheric & Planetary Sciences



The Effect of Trivalent Cations on the Major Lower Mantle Silicates

by

Krystle Carina Catalli

Submitted to the Department of Earth, Atmospheric & Planetary Sciences
on March 17, 2011, in partial fulfillment of the
requirements for the degree of
Doctor of Philosophy in Geophysics

Abstract

I have investigated the effect of composition, especially ferric iron and aluminum, on the equations of state and phase stability of perovskite and post-perovskite. The presence of trivalent cations decreases the bulk modulus of perovskite at pressures corresponding to the upper lower mantle. Ferric iron in perovskite undergoes a spin-pairing transition from the high spin state to low spin in the octahedral site. Ferric iron in the dodecahedral site remains high spin. In the absence of aluminum, the spin transition is gradual between 0 and 55 GPa, and bulk modulus increases at the completion of the spin transition. In the presence of aluminum, there is an abrupt increase in the amount of low spin ferric iron near 70 GPa, likely the result of site mixing. The high compressibility of the structure below 70 GPa results in the volume nearing that of magnesium endmember, MgSiO_3 , perovskite. Concurrent with the spin transition in aluminum-bearing perovskite, the structure stiffens. The increase in density and bulk modulus at ~ 70 GPa results in an increase in bulk sound speed that may be related to heterogeneities in bulk sound speed observed seismically at 1200-2000 km depth in the Earth. The effect of composition on the perovskite to post-perovskite phase transition was also investigated. No change in the spin state of ferric iron was found at the perovskite to post-perovskite phase transition: ferric iron is low spin in the octahedral site and high spin in the dodecahedral site. At the phase transition, ferric iron only slightly broadens the perovskite plus post-perovskite mixed phase region while ferrous iron and aluminum were each found to significantly broaden the mixed phase region to hundreds of kilometers thick. The effect of background mineral phases was assessed for a basaltic system, rich in aluminum. The coexisting minerals were found to significantly reduce the effect of the aluminum, producing a boundary that is potentially sharp enough for seismic detection in silicon-rich systems, such as basalt.

Thesis Supervisor: Sang-Heon Shim

Title: Associate Professor

Acknowledgments

Personal Thanks

I am very thankful to my advisor, Dan, for being a wonderful teacher and source of inspiration and support over the past six years. I have no doubt that Dan and MIT were the best choice for me for graduate school. He has been a very giving advisor, both of his time and his knowledge. I have learned a great deal from him over the years, and he has been nothing but supportive. His energy and excitement over science could inspire anyone.

I thank Javier and Laura for being my surrogate family in Cambridge my first two years at MIT and for being so supportive of my graduate education. Javier deserves special thanks for hiring me as a research assistant in the Mineral Physics Lab at UCSC when he was finishing his PhD. Without that experience I certainly never would have ended up at MIT or in this field. He continues to be a great mentor for me. In that same vein I must thank Quentin for being a great undergraduate research advisor who also encouraged me to continue in science.

Brent deserves plenty of thanks for being an excellent partner at the synchrotron; we used up just about every minute of beamtime. I also thank Brent for letting me always take the day shift even if that meant it threw his sleeping schedule all out of whack for a week after that.

My many friends in the Department of Earth, Atmospheric and Planetary Sciences at MIT were not only wonderful support during my time in graduate school but who also taught me so much about geology, geobiology, geochemistry, and geophysics.

I thank my family, especially my mom, for giving me the support and opportunities over the years that encouraged me to pursue my education to such a degree.

I thank my partner, Scott, for all of his emotional support. Scott came along after my general exam and introduced the fun back into my day-to-day life. We have walked miles and miles together around the cities of Cambridge and Boston, exploring restaurants and

having fun and complaining about not getting enough time out in nature.

Fellowship

During my third through final year of graduate school, I was supported by the Department of Energy National Nuclear Security Administration Stewardship Science Graduate Fellowship, administered by the Krell Institute. The Krell Institute has been a wonderful source of support, both financially and in career development.

Chapter 2

We thank N. Chatterjee, J. Hustoft, B. Grocholski, S. Slotznick, and D. LaBounty for assistance running the experiments. Experiments for Chapter 2 were performed using facilities at MIT, Lawrence Livermore National Lab (LLNL), and the Advanced Photon Source (APS). The use of the GSECARS sector of APS was supported by the NSF (EAR-0622171) and DOE (DE-FG02-94ER14466). Use of Sector 3 was partially supported by COMPRES. Portions of this work were performed under the auspices of the DOE by the Univ. of Calif., LLNL (W-7405-Eng-48). Use of HPCAT was supported by DOE-BES, DOE-NNSA, NSF, DOD-TACOM, and the W.M. Keck Foundation. Use of the APS was supported by the DOE (DE-AC02-06CH11357). K.C. was supported by the DOE NNSA Stewardship Science Graduate Fellowship. This work was supported by an NSF grant to S.H.S. (EAR0738655).

Chapter 3

J. Hustoft and N. Chatterjee assisted in data collection for Chapter 3. Use of GSECARS was supported by the NSF (EAR-0622171) and DOE (DE-FG02-94ER14466). Use of Sector 3 was partially supported by COMPRES under NSF Cooperative Agreement EAR 06-49658. K.C. was supported by the DOE NNSA SSG Fellowship. This work was supported by an NSF grant to S.H.S. (EAR0738655). Use of the APS was supported by the DOE under

Contract No. DE-AC02-06CH11357.

Chapter 4

Experiments for Chapter 4 were performed using facilities at MIT, Lawrence Livermore National Lab (LLNL), and the Advanced Photon Source (APS). The use of the GSECARS sector of APS was supported by the NSF (EAR-0622171) and DOE (DE-FG02-94ER14466). Use of Sector 3 was partially supported by COMPRES. Portions of this work were performed under the auspices of the DOE by the Univ. of Calif., LLNL (W-7405-Eng-48). Use of HPCAT was supported by DOE-BES, DOE-NNSA, NSF, DOD-TACOM, and the W.M. Keck Foundation. Use of the APS was supported by the DOE (DE-AC02-06CH11357). K.C. was supported by the DOE NNSA Stewardship Science Graduate Fellowship. This work was supported by an NSF grant to S.H.S. (EAR0738655).

Chapter 5

The work in Chapter 5 was supported by a National Science Foundation (NSF) grant to S.H.S. (EAR0738655). K.C. was supported by the DOE NNSA SSGF. A. Kubo and B. Grocholski assisted with X-ray measurements. Discussion with T. L. Grove and R. D. van der Hilst improved the paper. This work was performed at the GSECARS sector at APS. GSECARS is supported by the NSF and Department of Energy (DOE). Use of APS is supported by the DOE.

Chapter 6

The work in Chapter 6 was supported by a National Science Foundation (NSF) grant to S.H.S. (EAR0738655). K.C. was supported by the DOE NNSA SSGF. Discussion with R. D. van der Hilst improved the paper. This work was performed at the GSECARS sector at APS. GSECARS is supported by the NSF and Department of Energy (DOE). Use of APS

is supported by the DOE.

Appendix A

The work in Appendix A was supported by the NSF (EAR0337005, EAR0337156). We thank J. Santillán, H. P. Scott, J. Reed, and M. Kunz for assistance with XRD measurements and B. Kiefer, S. Speziale, and two anonymous reviewers for helpful discussions. Beamline 12.2.2 is supported by the COMPRES and DOE. GSECARS is supported by NSF and the State of Illinois. K. Catalli was supported by the DOE NNSA Stewardship Science Graduate Fellowship.

Biography

Education

Ph.D., Massachusetts Institute of Technology, Cambridge, MA June 2011

“The Effect of Trivalent Cations on the Major Lower Mantle Silicates”

Research advisor: Sang-Heon Shim

Thesis committee: Samuel A. Bowring, William Durham, William J. Evans,

Timothy L. Grove, and Robert D. van der Hilst

B.S., University of California, Santa Cruz, Santa Cruz, CA March 2005

“High pressure infrared spectroscopic studies of carbonates: Phase transitions in CaCO₃-III and PbCO₃” – highest honors

Research advisor: Quentin C. Williams

John Swett High School, Crockett, CA June 2001

Professional Societies

American Geophysical Union 2003 - Present

Association for Women Geoscientists 2005 - Present

Mineralogical Society of America 2006 - Present

Consortium for Materials Properties Research in Earth Sciences 2006 - Present

Geological Society of America 2007 - Present

Awards & Fellowships

- Department of Energy National Nuclear Security Administration
Stewardship Science Graduate Fellowship 2007 - 2011
- American Geophysical Union Mineral and Rock Physics
Graduate Research Award 2010
- Stewardship Science Graduate Fellowship Conference,
Best Presentation, Runner Up 2010
- Outstanding Student Paper Award, Study of the Earth’s Deep Interior Session,
American Geophysical Union Annual Fall Meeting 2009
- Stewardship Science Graduate Fellowship Conference,
Best Presentation, Runner Up 2009
- Research Assistantship, MIT, Department of Earth, Atmospheric,
and Planetary Science 2006 - 2007
- Grayce B. Kerr Fellowship, MIT, Department of Earth, Atmospheric
and Planetary Science 2005 - 2006
- National Science Foundation Graduate Research Fellowship,
Honorable Mention 2006
- National Science Foundation Graduate Research Fellowship,
Honorable Mention 2005
- Outstanding Student Award, Association for Women Geoscientists,
San Francisco Bay Area Chapter 2005
- UC Santa Cruz Dean’s Award for Outstanding Achievement in the
Physical and Biological Sciences Division (based on senior thesis) 2005
- UC Santa Cruz Chancellor’s Award for Outstanding Achievement in the
Physical and Biological Sciences Division (based on senior thesis) 2005
- Outstanding Student Employee Performance Award, UC Santa Cruz 2003

Publications

- B. Grocholski, K. Catalli, S.-H. Shim, V.B. Prakapenka (2011). Mineralogical effects on the post-perovskite transition. *In prep.*
- K. Catalli, S.-H. Shim, P. Dera, V.B. Prakapenka, J. Zhao, W. Sturhahn, P. Chow, Y. Xiao, H. Cynn, and W.J. Evans (2011). Effects of the Fe^{3+} spin transition on the properties of aluminous perovskite and new insights for lower-mantle seismic heterogeneities. *In prep.*
- K. Catalli, S.-H. Shim, V.B. Prakapenka, J. Zhao, and W. Sturhahn (2010). X-ray diffraction and Mössbauer spectroscopy of Fe^{3+} -bearing Mg-silicate post-perovskite at 128-138 GPa. *American Mineralogist*, 95, 418-421.
- K. Catalli, S.-H. Shim, V.B. Prakapenka, J. Zhao, W. Sturhahn, P. Chow, Y. Xiao, H. Liu, H. Cynn, and W.J. Evans (2010). Spin state of ferric iron in MgSiO_3 perovskite and its effect on elastic properties. *Earth and Planetary Science Letters*, 289, 68-75.
- K. Catalli, S.-H. Shim, and V.B. Prakapenka (2009). Thickness and Clapeyron slope of the post-perovskite boundary. *Nature*, 462, 782-785.
- S.-H. Shim and K. Catalli (2009). Compositional dependence of the amorphous-amorphous transition in mantle-related systems, *Earth and Planetary Science Letters*, 283, 174-180.
- S.-H. Shim, A. Bengtson, D. Morgan, W. Sturhahn, K. Catalli, J. Zhao, M. Lerche, and V.B. Prakapenka (2009). Electronic and magnetic properties of the postperovskite-type Fe_2O_3 - Implications for planetary magnetic records and deep interior transitions. *Proceedings of the National Academy of Sciences*, 106, 5508-5512.
- S. Lundin, K. Catalli, J. Santillán, S.-H. Shim, V.B. Prakapenka, M. Kunz, and Y. Meng (2008). Effect of Fe on the equation of state of mantle silicate perovskite over 1 Mbar, *Physics of the Earth and Planetary Interiors*, 168, 97-102.
- S.-H. Shim, K. Catalli, J. Hustoft, A. Kubo, V.B. Prakapenka, W.A. Caldwell, and M. Kunz (2008). Crystal structure and thermoelastic properties of $(\text{Mg}_{0.91}, \text{Fe}_{0.09})\text{SiO}_3$ postperovskite up to 135 GPa and 2700 K, *Proceedings of the National Academy of Sciences*, 105, 7382-7386.
- J. Hustoft, K. Catalli, S.-H. Shim, A. Kubo, V.B. Prakapenka, and M. Kunz (2008). Equation of state of NaMgF_3 post-perovskite Implication for the seismic velocity changes

-
- at the lowermost mantle, *Geophysical Research Letters*, 35, L10309.
- K. Catalli, S.-H. Shim, and V.B. Prakapenka (2008). A crystalline-to-crystalline phase transition in $\text{Ca}(\text{OH})_2$ at 8 GPa and room temperature, *Geophysical Research Letters*, 35, L05312.
- K. Catalli and Q. Williams (2005). A high pressure phase transition of calcite-III. *American Mineralogist*, 90, 1679-1682.
- Catalli, J. Santillán, and Q. Williams (2005). High-pressure infrared spectroscopic study of PbCO_3 -cerussite: Constraints on the post-aragonite phase. *Physics and Chemistry of Minerals*, 32, 412-417.
- J. Santillán, K. Catalli, and Q. Williams (2005). An infrared study of carbon-oxygen bond distance in magnesite from 0 to 60 GPa. *American Mineralogist*, 90, 1669-1673.

Contents

1	Introduction and motivation	23
1.1	Scientific background	23
1.2	Diamond anvil cell experiments	26
1.2.1	Pressure determination	27
1.2.2	Synchrotron powder X-ray diffraction	29
1.2.3	Synchrotron Mössbauer spectroscopy	31
1.2.4	Synchrotron X-ray emission spectroscopy	32
2	Spin state of ferric iron in perovskite	35
2.1	Introduction	36
2.2	Experimental procedure	38
2.3	Results	42
2.3.1	Effect of ferric iron on the structure of perovskite	42
2.3.2	Synchrotron Mössbauer spectroscopy	44
2.3.3	X-ray emission spectroscopy	49

2.3.4	Equation of state	50
2.4	Implications for the spin state of Fe in perovskite	55
2.5	Implications for the lower mantle	56
2.6	Conclusions	59
3	X-ray diffraction and Mössbauer of ferric post-perovskite	63
3.1	Introduction	64
3.2	Experimental	65
3.3	Results	66
3.4	Discussion and geophysical implications	72
4	Combined effect of ferric iron and aluminum on the properties of perovskite	75
4.1	Introduction	76
4.2	Experimental procedure	78
4.3	Results	85
4.3.1	Effects of ferric iron and aluminum on the structure of perovskite	85
4.3.2	Synchrotron Mössbauer spectroscopy	86
4.3.3	X-ray emission spectroscopy	89
4.3.4	Equation of state	90
4.4	Implications for the crystal chemistry of perovskite	94
4.5	Implications for the lower mantle	96
4.6	Conclusions	102
5	Thickness and Clapeyron slope of the post-perovskite boundary	105
5.1	Introduction	106
5.2	Methods	107
5.3	Results	109
5.3.1	Ferrous post-perovskite	109
5.3.2	Ferric-aluminous post-perovskite	111

5.3.3	Ferric post-perovskite	111
5.4	Discussion	113
5.5	Geophysical implications	116
6	Thickness of the post-perovskite boundary in MORB-type composition	123
6.1	Introduction	124
6.2	Methods	126
6.3	Results	128
6.4	Discussion	132
6.5	Geophysical implications	135
A	A Crystalline-to-Crystalline Phase Transition in Ca(OH)₂	139
A.1	Introduction	140
A.2	Experimental	141
A.3	Results	141
A.4	Discussion	146
	Bibliography	151

Contents

List of Figures

1-1	Schematic of the diamond cell sample chamber	26
1-2	Schematic of the diamond cell setup for X-ray diffraction and in situ laser heating	30
1-3	Schematic of the diamond cell setup for synchrotron Mössbauer spectroscopy	31
1-4	Schematic of the diamond cell setup for X-ray emission spectroscopy . . .	33
2-1	X-ray diffraction patterns of ferric perovskite	40
2-2	Axial ratios of ferric perovskite	45
2-3	Synchrotron Mössbauer spectra of ferric perovskite	46
2-4	Mössbauer parameters of ferric perovskite	47
2-5	X-ray emission spectra of ferric perovskite	49
2-6	Volume of ferric perovskite as a function of pressure.	52
2-7	Density and bulk modulus of perovskites compared with the Preliminary Reference Earth Model	54
3-1	X-ray diffraction patterns of ferric post-perovskite	67

List of Figures

3-2	Volume of ferric post-perovskite as a function of pressure	68
3-3	Synchrotron Mössbauer spectra of ferric perovskite and post-perovskite . . .	70
4-1	Representative X-ray diffraction patterns of ferric-aluminous perovskite . . .	80
4-2	Fitting results of synchrotron Mössbauer spectra of ferric-aluminous perovskite	81
4-3	Synchrotron Mössbauer spectra of ferric-aluminous perovskite	82
4-4	X-ray emission spectra of ferric-aluminous perovskite	83
4-5	Pressure effect on X-ray emission spectra of ferric-aluminous perovskite . . .	84
4-6	Axial ratios of different perovskite compositions with pressure	87
4-7	Pressure–volume relationship for a range of perovskite compositions	92
4-8	Density, bulk modulus, and bulk sound speed in different perovskite compositions	97
4-9	Schematic of a ferric iron rich heterogeneity in the lower mantle	100
5-1	X-ray diffraction patterns of perovskite and post-perovskite at high pressure–temperature	110
5-2	The pressure–temperature conditions for the stability of ferrous and ferric-aluminous perovskite and post-perovskite	112
5-3	The pressure–temperature conditions for the stability of ferric perovskite and post-perovskite	114
5-4	Calculated boundary thickness and phase fractions for post-perovskite	118
6-1	Representative X-ray diffraction patterns of basaltic composition at lower-most mantle conditions	126
6-2	Pressure–temperature phase stability for perovskite and post-perovskite in basalt	129
6-3	Pressure–volume relationship in SiO ₂ in basalt	131

6-4	X-ray diffraction pattern showing unknown line associated with CaCl ₂ - type SiO ₂	131
6-5	Summary of compositional effect on the post-perovskite boundary	133
A-1	XRD patterns of Ca(OH) ₂ at high pressure	142
A-2	Raman spectra of Ca(OH) ₂	144
A-3	Pressure-induced Raman mode shifts for Ca(OH) ₂	145
A-4	The <i>R</i> ₁ line width and the <i>R</i> ₁ and <i>R</i> ₂ separation of ruby fluorescence	148

List of Figures

List of Tables

2.1	Unit-cell volumes and lattice parameters of ferric perovskite up to 106 GPa	60
2.2	Mössbauer parameters for ferric perovskite	61
3.1	Unit-cell volumes and lattice parameters of ferric post-perovskite	74
3.2	Mössbauer parameters for ferric post-perovskite	74
4.1	Unit-cell volumes and lattice parameters of ferric-aluminous perovskite up to 94 GPa	103
4.2	Unit-cell volumes and lattice parameters of aluminous perovskite up to 95 GPa	104
6.1	Composition of synthetic N-MORB-like starting material	137

List of Tables

Introduction and motivation

The special difficulty of the problem of the physics of the earth's interior arises from the extremely restricted range, both of depth and time, for which any direct evidence is available . . . In addition, all observations of earthquakes and all observations of topography and gravity have to be made at the surface or near it. Thus the problem of the physics of earth's interior is to make physical inferences over a range of depth of over 6000 km from data determined only for a range of 2 km at the outside.

–Harold Jeffries, Introduction to *The Earth*, 1924

1.1 Scientific background

The lower mantle has been known as a seismically distinctive layer in the Earth since the late 1930s [Jeffries, 1939; Bullen, 1940], but no change in the crystal structure of the

major mantle phases were known to explain it. Based on analog studies, there were several possible transitions that were proposed to explain the 660 km discontinuity, including $\beta\text{-(Mg,Fe)}_2\text{SiO}_4 \rightarrow$ strontium plumbate type, pyrope-rich garnet \rightarrow ilmenite type, calcium-rich garnet \rightarrow perovskite type, jadeite disproportionation to the calcium ferrite type phase, and $\beta\text{-(Mg,Fe)}_2\text{SiO}_4 \rightarrow (\text{Mg,Fe})\text{SiO}_3$ - ilmenite + ferroperclase [Ringwood, 1970]. When high pressure techniques were finally capable of reliably reaching the pressure–temperature conditions required, Liu [1975] found that $\beta\text{-(Mg,Fe)}_2\text{SiO}_4$ broke down to $(\text{Mg,Fe})\text{SiO}_3$ –perovskite + ferropericalse at pressure–temperature conditions consistent with the discontinuity.

The next major unexplained seismic discontinuity is called the D'' which was first described seismically over 60 years ago [Bullen, 1949] and exists at $\sim 150\text{--}300$ km above the core-mantle boundary [Lay *et al.*, 1998], at pressures in excess of 120 GPa. The D'' layer is especially interesting as it exists at the boundary of the core and the mantle, the greatest change in both density and composition occurring inside the Earth. This region is also expected to mark a considerable thermal boundary layer in the Earth, with a temperature contrast between mantle and core of $\sim 1000 \pm 500$ K [Loper and Lay, 1995].

In 2004, several independent groups simultaneously found a phase transition in MgSiO_3 perovskite, to the post-perovskite phase [Murakami *et al.*, 2004; Oganov and Ono, 2004; Shim *et al.*, 2004]. The new high pressure phase had remained elusive for many years due to the high pressures (~ 120 GPa) and temperatures (~ 2000 K) required to synthesize the phase. Even when reaching these conditions, synthesis of the phase is challenging, dependent on the starting material and frequently requiring long heating durations. However, recent advances in third generation synchrotron facilities allow us to probe changes in the properties of perovskite based on composition, including the effects of spin and valence states of iron in perovskite.

In Chapter 2, I present the results from experiments on the effects of ferric iron substitution into Mg-silicate perovskite. Over the past fifteen years, ferric iron has been recognized as an important component in perovskite [McCammon, 1997; McCammon *et al.*, 1997]. Its presence, up to 60% of total iron, is found even under reducing conditions [Frost *et al.*, 2004]. I measured the equation of state of ferric iron bearing perovskite to 100 GPa, and compared it to a pure MgSiO₃ perovskite that I previously measured under the same sample conditions [Lundin *et al.*, 2008].

In Chapter 3, I present measurements made on the same ferric iron bearing starting material to determine the spin state of iron and the density of post-perovskite.

In Chapter 4, I continue with a systematic approach to understanding trivalent cations in perovskite by measuring the spin state of ferric iron in ferric-aluminous perovskite as well as the equations of state of ferric-aluminous perovskite and aluminous perovskite. Aluminum does seem to have an effect on the spin state behavior of ferric iron in perovskite.

In Chapter 5, I investigate the effects of cation substitution on the depth and thickness of the post-perovskite transition, namely ferrous iron, ferric iron, and ferric iron and aluminum together. These measurements have the advantage over previous studies of all being made in an internally consistent fashion with the same sample setup, pressure standard and laser heating conditions to more easily understand the relative effects of different cations.

After understanding the effects of composition within the Mg-silicate components, in Chapter 6, I extend the work of Chapter 5 to a MORB-like composition to understand the effects of background mineral phases on the post-perovskite transition.

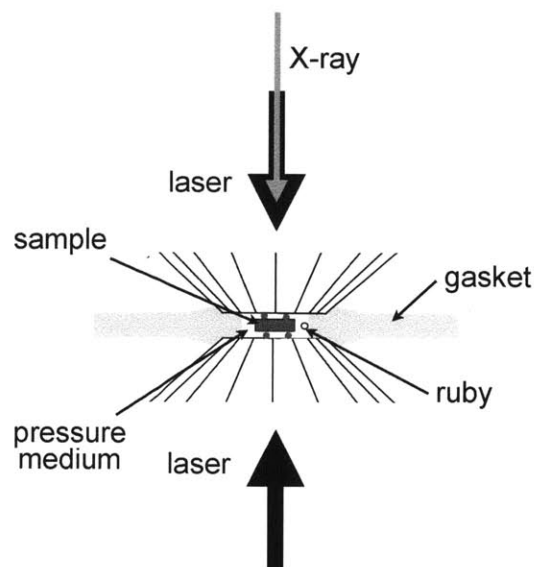


Figure 1-1: Schematic of the standard sample setup within the diamond anvil cell.

1.2 Diamond anvil cell experiments

The diamond anvil cell is a piston-cylinder type apparatus that can generate pressures up to the multi-megabar (300 GPa) range by compressing samples between two opposing gem-quality diamonds. Symmetric-type diamond anvil cells, which have been optimized for double-sided laser heating, are used here. Diamond is not only extremely strong, but it is transparent to a wide range of electromagnetic radiation, including γ -rays, X-rays and visible light.

A typical sample setup is shown in figure (Fig. 1-1). Diamonds with culets of 75–300 μm diameter are typically used for experiments in the 25–150 GPa range, depending on the intended peak pressure of the experiment, and a 100 μm thick rhenium (or beryllium for X-ray emission measurements) foil is pre-indented, using the diamond anvil cell, to a thickness of 20–40 μm for use as a gasket to contain the sample. The foil is then drilled

using an electric discharge machine (EDM) with a hole that is approximately 50% the diameter of the diamond culet (Fig. 1-1).

Sample powders are pressed into a platelet using a diamond cell equipped with 500 μm culet diamond or moissanite anvils. Platelets are 5–15 μm thick and 15–50 μm in diameter, depending on the peak pressure of the sample. After the gasket is seated on the diamond anvil, a platelet is placed in the sample chamber and surrounded by a thermally insulating pressure-transmitting medium. The ideal medium for this is an inert material with low strength to minimize deviatoric stresses at high pressure and prevent heat loss to the highly thermally conductive diamond anvils. (Fig. 1-1).

Three different pressure/insulation media are used in the following chapters: argon, neon, and sodium chloride. Argon is a quasi-hydrostatic inert medium that has the advantage of being easily cryogenically loaded into the diamond cell in the Mineral Physics Lab at MIT. Neon is more hydrostatic, but requires a specialized gas-loading setup. This is available at the GeoSoilEnviroCARS sector of the Advanced Photon Source, where all neon loading was performed. Sodium chloride is a less ideal medium since it is solid, but was necessary for X-ray emission spectroscopy measurements due to the use of highly toxic beryllium gaskets.

1.2.1 Pressure determination

Pressure in the diamond cell is generally measured with an internal standard that has been calibrated with other absolute pressure measurements, such as shock wave [Holmes *et al.*, 1989; Jamieson *et al.*, 1982] or elasticity [Zha *et al.*, 2000] experiments, or robust theoretical predictions [Tsuchiya, 2003]. There are three different pressure standards used here: gold [Tsuchiya, 2003], ruby [Mao *et al.*, 1986], and diamond [Akahama and Kawamura, 2006]. Gold is used in X-ray diffraction experiments, where gold powder (grain size of

$\sim 1\mu\text{m}$) is mixed with the sample powder and the unit-cell volume of gold is measured in the same diffraction pattern as the sample, and used to calculate pressure. For spectroscopy measurements, a small ruby chip or sphere is placed at the edge of the sample chamber (Fig. 1-1), and its fluorescence is used to calculate pressure [Mao *et al.*, 1986]. When the ruby signal is insufficient, the Raman signal from the diamond culet is used to estimate pressure [Akahama and Kawamura, 2006].

Using gold as a pressure standard in X-ray diffraction measurements has the advantage of determining pressure at the same location in the sample chamber as the sample, ensuring the pressure determined is made at the same spot where the sample is probed. Gold has been calibrated against temperature as well as pressure, so the pressure can be determined at high temperature [Jamieson *et al.*, 1982; Heinz *et al.*, 1994; Shim *et al.*, 2002], a valuable feature for the study of Earth materials.

Although measuring the lattice parameter of gold is routine, no consensus exists on the correct equation of state to use to obtain the pressure and other standards such as platinum or magnesium oxide may differ even more [Fei *et al.*, 2004]. This results in different equations of state varying by 10% or more at pressures above 100 GPa. For example, depending on the pressure scale used, the post-perovskite transition in MgSiO_3 has been found to occur anywhere from 102–126 GPa (at 2000 K) with a Clapeyron slope of 4.7–11.2 MPa/K [Ono and Oganov, 2005; Hirose *et al.*, 2006; Shim, 2008]. This is the largest and most obvious uncertainty in phase boundary and equation of state measurements made in the diamond cell. I have taken the approach of making all of my X-ray diffraction measurements internally consistent by using one scale [Tsuchiya, 2003] for all measurements. This gives us the advantage of being able to compare between the different data sets I have collected and assess the effect of composition independent of pressure scale effects. The errors in pressure in X-ray diffraction measurements represent the precision in the volume of gold

measured and do not take into account the uncertainties in the pressure scale itself.

The pressure induced shift of the R1 ruby fluorescence line have been well calibrated against the shock wave measurements on multiple metals [Mao *et al.*, 1986]. When ruby failed to give a reliable pressure reading at very high pressures, due to the weakening of the fluorescence signal [Eggert *et al.*, 1988] or the ruby being crushed, the Raman signal from the diamond anvil was used [Akahama and Kawamura, 2006]. This diamond scale is tied to the platinum scale of Holmes *et al.* [1989].

1.2.2 Synchrotron powder X-ray diffraction

X-ray diffraction measurements in this thesis were made in the angle dispersive setup. The d -spacing is calculated using Bragg's equation:

$$2d\sin\theta = n\lambda \quad (1.1)$$

where d is the interlayer spacing, n is an integer, and λ is the wavelength of the X-ray beam.

All X-ray diffraction measurements were made at the Advanced Photon Source at Argonne National Lab. The monochromatic X-ray beam is focused to a diameter of $\sim 5 \times 5 \mu\text{m}^2$ (13-IDD/16-IDB) or $\sim 10 \times 20 \mu\text{m}^2$ (13-BMD) spot based on the full-width at half maximum, depending on the beamline used. For phase boundary studies, the double-sided laser heating is performed with the laser beam co-aligned with the X-ray beam so that diffraction is measured at the hot spot (Fig. 1-2). A typical heating spot is $\sim 25 \mu\text{m}$ in diameter. The X-ray exposure time for diffraction measurements varied depending on the beamline. At beamline 13-IDD, collection time typically took 10–60 s for mantle silicates at high pressures and temperatures, while collection time was 5–10 min at 13-BMD. At beamline 16-IDB at HPCAT exposure time was 30–60 sec.

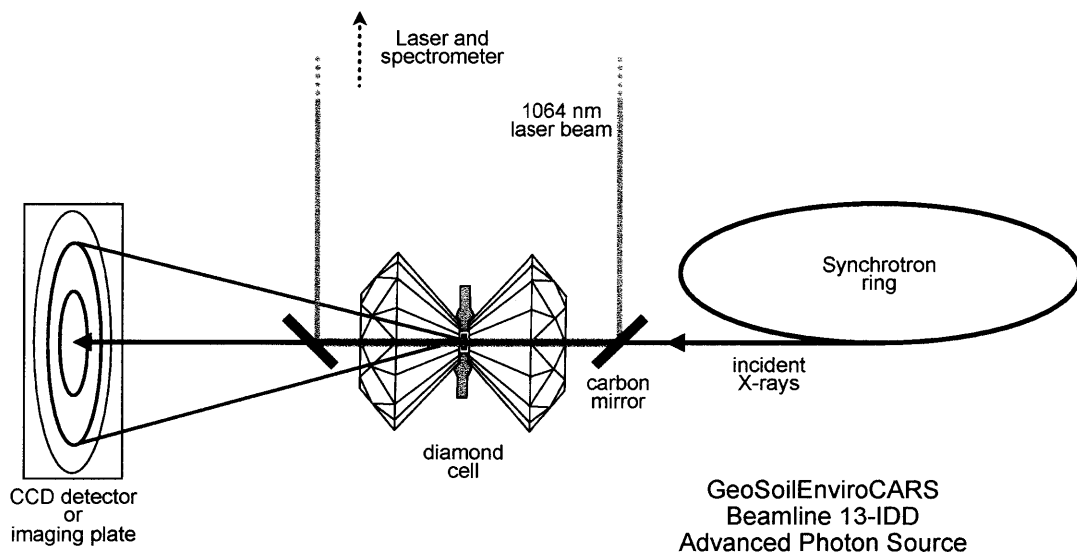


Figure 1-2: Schematic of the diamond cell setup for X-ray diffraction and in situ laser heating at the GeoSoilEnviroCARS sector of the Advanced Photon Source. X-ray semi-transparent carbon mirrors are used to bring the laser beam into the sample. The laser and X-ray beams are co-aligned. X-ray wavelengths in the range of 30–40 keV are typically used.

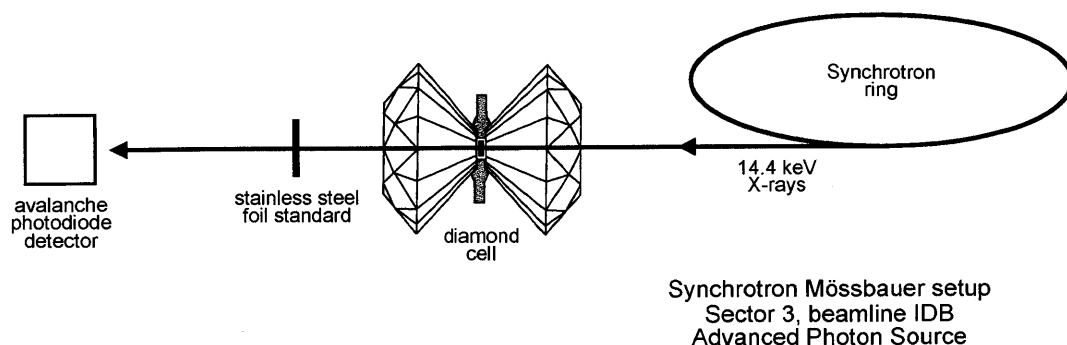


Figure 1-3: Schematic of the diamond cell setup for synchrotron Mössbauer spectroscopy at Sector 3 of the Advanced Photon Source. The wavelength of the incident X-ray was set to 14.4 keV.

1.2.3 Synchrotron Mössbauer spectroscopy

Mössbauer spectroscopy has found widespread use in the fields of chemistry, physics and mineralogy. Mössbauer spectroscopy permits the measurement of the hyperfine interactions in ^{57}Fe . The hyperfine interaction is the splitting of nuclear levels resulting from the interaction of the nucleus with the electronic environment. The nuclear environment depends on multiple factors in the mineral including the valence state of iron and its coordination and site symmetry. In silicate minerals, the parameters of interest include the isomer shift and the quadrupole splitting for iron in the mineral.

The isomer shift results from a Coulombic interaction between the nuclear and electronic charge distributions resulting from the s -electron charge density at the nucleus. Isomer shift can only be measured relative to a standard absorber, such as the iron in stainless steel, or given as a relative value among iron sites within the sample. Quadrupole splitting results from a non-spherical charge distribution around the nucleus, which is caused by the interaction of the nuclear quadrupole moment with a gradient in the electric field due to other charges around the iron nucleus, splitting the nuclear energy levels. Quadrupole

splitting is analogous to the splitting of $3d$ orbitals in transition metals due to crystal field splitting (which leads to the colors in many minerals) [Burns, 1993].

Synchrotron Mössbauer spectroscopy detects the quadrupole splittings and isomer shifts of ^{57}Fe in the sample similar to conventional Mössbauer spectroscopy, with the added benefit of the high brilliance of the synchrotron radiation which dramatically reduces the data acquisition time [Alp *et al.*, 1995]. This makes Mössbauer spectroscopy much more accessible for the high pressure measurement of mantle silicates which have dilute iron contents and very small sample volumes. While X-ray emission spectroscopy (see below) provides only an integrated average spin moment for the sample [Vankó *et al.*, 2006], Mössbauer spectroscopy has the ability to isolate different iron sites in the sample, and provide information on the spin and valence states [Dyar *et al.*, 2006].

At ambient pressures, measurements of quadrupole splitting and isomer shift of iron in a mineral is usually sufficient to identify the valence state and site occupancies of irons, generally done by a basic fingerprinting technique [Bancroft *et al.*, 1967]. This approach does not cleanly translate to the study of minerals at high pressure. Pressure has the effect of changing the electronic distribution around the iron nuclei either simply by densification or by increases in coordination number and changes in spin state changes in spin state. This makes determining the iron valence state and spin state a little more ambiguous, but not impossible. In the last few years, attempts at computing the expected quadrupole splitting and isomer shifts for Fe^{2+} and Fe^{3+} in Mg-silicate perovskite in different crystallographic sites and spin states have found some success [Bengtson *et al.*, 2009; Hsu *et al.*, 2010, 2011].

1.2.4 Synchrotron X-ray emission spectroscopy

Synchrotron based X-ray emission spectroscopy is a relatively newly developed technique that is used for probing the local electronic structure of $3d$ transition metals, which is

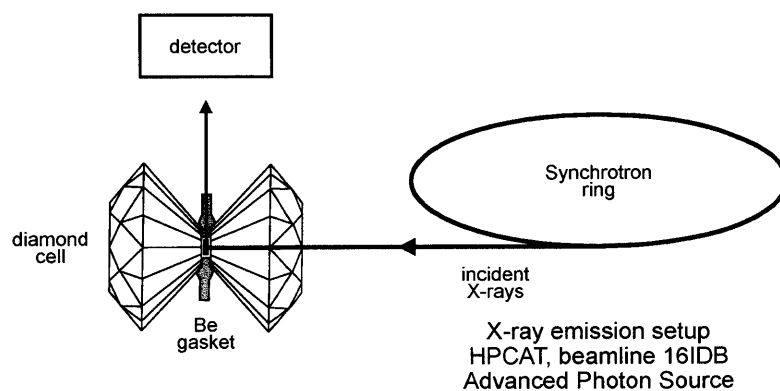


Figure 1-4: Schematic of the diamond cell setup for X-ray emission spectroscopy at the HPCAT sector of the Advanced Photon Source. The wavelength of the incident X-ray was set to 11.35 keV.

useful for the study of iron in mantle silicates [Badro *et al.*, 2004]. Although it is not well-suited for distinguishing between different valence states or crystallographic sites, it can measure the integrated spin state of the sample when suitable high and low spin standards are available, and can measure relative changes in spin state when they are not.

The X-ray emission spectrum is sensitive to the magnetic moment of iron in the sample [Vankó *et al.*, 2006]. The spectrum for iron is characterized by the main $K'_{\beta_{1,3}}$ emission line at 7058 eV, and a satellite (K'_{β}) peak, which exists at slightly lower energy and results from the $3p - 3d$ core-hole exchange interaction in the final state of emission [Vankó *et al.*, 2006]. A transition from the high spin to low spin state is characterized by loss of intensity in the satellite peak.

Because diamond strongly attenuates energy in the 5–10 keV range, beryllium, which has a small scattering cross section, is used to gasket the sample and emitted photons are detected at a 90° angle from the loading axis of the diamond cell, through the beryllium gasket (Fig. 1-4).

Spin state of ferric iron in MgSiO₃ perovskite and its effect on elastic properties

K. Catalli, S.-H. Shim, V.B. Prakapenka, J. Zhao, W. Sturhahn, P. Chow, Y. Xiao, H. Liu, H. Cynn, and W.J. Evans (2010). Earth and Planetary Science Letters, 289, 68-75.

Abstract

Recent studies have indicated that a significant amount of Fe in MgSiO₃ perovskite is Fe³⁺ (Fe³⁺/ΣFe = 10–60%) due to crystal chemistry effects at high pressure and that Fe³⁺ is more likely than Fe²⁺ to undergo a high spin to low spin transition in perovskite. In order to study the spin transition in Fe³⁺ and its effect on the properties of perovskite, we have measured synchrotron Mössbauer spectroscopy (SMS), X-ray emission spectroscopy (XES), and X-ray diffraction (XRD) of perovskite with all Fe in Fe³⁺ in the laser-heated diamond-anvil cell to over 100 GPa. Fe³⁺ increases the anisotropy of the unit cell of perovskite, the opposite effect of Fe²⁺. In perovskite synthesized above 50 GPa, Fe³⁺ enters into both the dodecahedral (A) and octahedral (B) sites approximately equally, suggesting charge coupled substitution. Both SMS and XES indicate that the low spin population in the B site gradually increases with pressure up to 50–60 GPa where all Fe³⁺ in the B site becomes low spin. However, Fe³⁺ in the A site remains high spin to at least 136 GPa. Fe³⁺ makes perovskite more compressible than Mg-endmember below 55 GPa because of the gradual spin transition in the B site together with lattice compression. The completion of the spin transition at 55 GPa results in a 10±4% increase in bulk modulus with no associated change in density. The elasticity change resulting from the completion of the Fe³⁺

spin transition can be a useful seismic probe for investigating compositional heterogeneities associated with Fe³⁺ and Al.

2.1 Introduction

Mg-silicate perovskite is the most abundant silicate mineral in the Earth, with a stability from 660-km depth to several hundred kilometers above the core-mantle boundary [Knittle and Jeanloz, 1987; Shim *et al.*, 2001, 2004]. Perovskite is expected to contain 5–10 mol% of Fe and Al in a pyrolitic mantle composition [Ringwood, 1975; Kesson *et al.*, 1998; Lee *et al.*, 2004].

Based on recent studies of Fe in perovskite, Fe³⁺ is emerging as an increasingly relevant component. Studies using starting materials containing only Fe²⁺ found that perovskite in its stability field has a considerable amount of Fe³⁺, Fe³⁺/ΣFe \simeq 16% [McCammon, 1997], in the absence of Al. If Al is included, Fe³⁺/ΣFe increases further, to 50–75% [McCammon, 1997]. Several studies [Frost *et al.*, 2004; Auzende *et al.*, 2008; Zhang and Oganov, 2006] have shown that Fe²⁺ may disproportionate, creating free Fe metal, enriching perovskite with Fe³⁺. Frost *et al.* [2004] and McCammon [2005] argued that the significant amount of Fe³⁺ in perovskite is not the result of the oxidation state of the lower mantle, which is expected to be reducing, but due to the crystal chemistry of perovskite at high pressure.

Badro *et al.* [2004] reported a high-spin to low-spin transition in Fe in perovskite based on X-ray emission spectroscopy (XES), that occurred as a two step process where approximately half of the Fe became low spin at 70 GPa and the other half at 120 GPa. Li *et al.* [2004], however, found a gradual spin transition to occur both in Al-bearing and Al-free perovskite which was still incomplete at 100 GPa based on XES. Based on a shift in the

volume dependence of the relative isomer shift in synchrotron Mössbauer spectroscopy (SMS), *Jackson et al.* [2005] proposed a spin transition in the Fe^{3+} -like site completing near 70 GPa.

In computational studies, Fe^{3+} was found to be in the low spin state in the B site of perovskite at all pressures relevant to the mantle while Fe^{2+} remains high spin throughout the mantle [*Cohen et al.*, 1997; *Zhang and Oganov*, 2006; *Li et al.*, 2005a; *Stackhouse et al.*, 2007]. A more recent computational study [*Umemoto et al.*, 2008] has shown that the spin transition of Fe^{2+} is possible but limited to specific configurations in perovskite. Therefore, Fe^{3+} may play a more important role in the spin transition in perovskite.

Fe^{3+} may also alter the properties of perovskite. Increased Fe^{3+} in perovskite has been found to significantly enhance the electrical conductivity [*Xu et al.*, 1998]. Also, Fe^{3+} may control the radiative conductivity of perovskite in the lower mantle [*Goncharov et al.*, 2008; *Keppler et al.*, 2008]. Although previous studies have investigated the equation of state of iron-bearing perovskite [*Knittle and Jeanloz*, 1987; *Andrault et al.*, 2001; *Lundin et al.*, 2008], $\text{Fe}^{3+}/\Sigma\text{Fe}$ was not measured in those samples, and Mössbauer studies have shown a wide range of $\text{Fe}^{3+}/\Sigma\text{Fe}$ values even in the absence of Al [*McCammon*, 1997; *Jackson et al.*, 2005].

There is a significant amount of ambiguity in interpreting Mössbauer results for perovskite containing both Fe^{2+} and Fe^{3+} because of overlapping values for the quadrupole splitting (QS) of high spin Fe^{2+} and low spin Fe^{3+} as well as low spin Fe^{2+} and high spin Fe^{3+} [*Li et al.*, 2006]. Furthermore, very high QS values of Fe in perovskite have been reported in recent Mössbauer studies and attributed to an intermediate spin state of Fe^{2+} [*Lin et al.*, 2008; *McCammon et al.*, 2008]. However, computational studies do not support the stability of intermediate spin Fe [*Li et al.*, 2005a; *Tsuchiya et al.*, 2006]. Therefore, in order to understand the spin state of Fe and its effects on the properties of perovskite, it is

important to distinguish between the effects of Fe^{2+} and Fe^{3+} .

Andrault and Bolfan-Casanova [2001] demonstrated that perovskite can be synthesized from $\text{MgSiO}_3 + \text{Fe}_2\text{O}_3$. We found that perovskite with all Fe in Fe^{3+} can be synthesized as confirmed by our Mössbauer spectroscopy, although according to the literature, synthesizing perovskite with all Fe in Fe^{2+} is difficult [*McCammon*, 1997]. We have performed SMS and XES on a sample with $\text{Fe}^{3+}/\Sigma\text{Fe} = 1$ in the laser-heated diamond anvil cell, allowing for a reliable assignment of spin state. In order to study the effect of spin transition on the equation of state of perovskite, we performed XRD on ferric perovskite and compared it to that of Mg-endmember perovskite measured using a common pressure medium (Ar) and pressure standard (Au) [*Lundin et al.*, 2008]. This allows for comparison between the systems that would not otherwise be possible due to varied levels of deviatoric stress and disagreement among common pressure scales at high pressure [*Shim et al.*, 2001; *Fei et al.*, 2004].

2.2 Experimental procedure

A glass starting material was synthesized from a $0.9\text{MgSiO} + 0.1\text{Fe}_2\text{O}_3$ (95% enriched ^{57}Fe) mixture using the containerless laser levitation method in an O_2 atmosphere in order to prevent reduction during melting [*Tangeman et al.*, 2001]. The glass making process yielded several beads of ~ 1 mm in diameter. The composition was examined using electron microprobe on a randomly selected glass bead. Measurements revealed a very homogeneous starting material. However, there was a 5% and 3% loss of Mg and Fe, respectively, during melting due to the volatility of these elements. The amount of oxygen and iron measured using electron microprobe indicates that all Fe exists as Fe^{3+} , which is also consistent with our Mössbauer results.

The beads were broken and ground to a powder and mixed with 10 wt% Au for use as an internal pressure standard [Tsuchiya, 2003] for the XRD study. For SMS, a couple of ruby grains were placed at the edge of the sample for pressure determination [Mao *et al.*, 1986] at 47–63 GPa. Above this pressure the first-order Raman mode of diamond, the anvil material, was used to estimate pressure [Sun *et al.*, 2005]. Pressure in XES was determined by ruby.

Symmetric type diamond anvil cells were used in all experiments. Diamonds with a culet size of 200 μm were used for measurements with a peak pressure less than 75 GPa. Above this pressure diamonds with 100 or 150 μm beveled culets were used. Measurements in each respective data set were taken from multiple sample loadings.

For XRD and SMS, the sample powder was pressed to a foil of ~ 10 μm thickness, and loaded into a preindented Re gasket. Ar was cryogenically loaded into the diamond cell, acting as both an insulating and a pressure medium. A few spacer grains of the starting material were used to keep the sample foil from having direct contact with the diamond anvils, because diamond has a large thermal conductivity. Ar diffraction lines are well resolved to the highest pressures of our study, confirming the presence of a significant amount of medium (Fig. 2-1). Both the hexagonal close-packed (hcp) and face-centered cubic structures of Ar are observed in some of our diffraction patterns. This is likely due to the inclusion of a small amount of nitrogen in our sample loading that leaked in during cryogenic loading of Ar, which stabilizes the hcp phase [Wittlinger *et al.*, 1997; Catalli *et al.*, 2008]. For XES, 3 mm diameter Be gaskets with an initial central thickness of 100 μm were used. A sample platelet was pre-pressed and sandwiched between 5 μm layers of dried NaCl and loaded into the gasket hole.

Angle dispersive XRD was performed at the GSECARS and HPCAT sectors of the Advanced Photon Source. A monochromatic X-ray beam with energy of 30 or 28 keV was

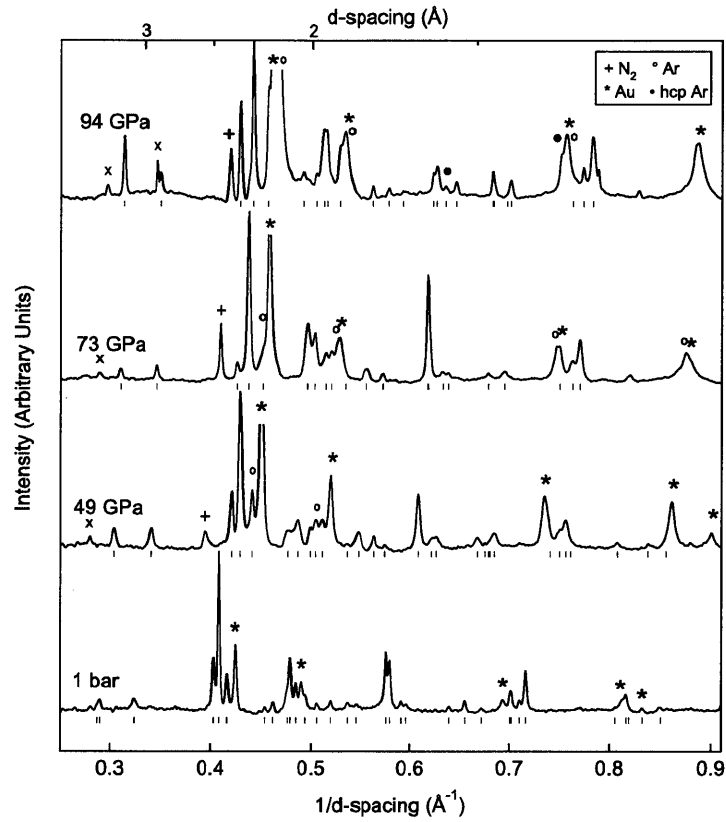


Figure 2-1: High-pressure X-ray diffraction patterns of ferric perovskite synthesized from glass starting material. Tick marks beneath each pattern show the locations of perovskite peaks used in the unit-cell fitting (\times : unknown lines, *: Au pressure standard, +: N₂, o: Ar pressure medium, •: h.c.p. Ar). Backgrounds were subtracted.

focused to a size smaller than $10 \times 20 \mu\text{m}^2$. The diffraction images were collected using either a MarCCD detector or a Mar345 imaging plate. The downstream diamond anvil was mounted on an X-ray semi-transparent cBN backing plate, extending the measurable d -spacing to 1.1 Å. A total of 13–28 diffraction lines were used to constrain the volume of perovskite using the UnitCell program [Holland and Redfern, 1997]. The volume of Au was measured based on 2–5 diffraction lines and pressure was calculated using the scale of Tsuchiya [2003]. The uncertainty in pressure given is the standard deviation in pressure based on the volume of gold calculated from each individual diffraction line. Pressure, volume and axial lengths are presented in Tab. 2.1.

SMS was performed at Sector 3 of the Advanced Photon Source. The X-ray beam was focused to an area of $6 \times 6 \mu\text{m}^2$. The storage ring was operated in top-up mode with 24 bunches separated by 153 ns. Nuclear resonant scattering was measured in a time window of 15–130 ns following excitation. Data collection typically took 2 hours [see Jackson *et al.*, 2005; Sturhahn and Jackson, 2007, for more information]. SMS data were fit using the CONUSS package [Sturhahn, 2000].

XES was performed at the HPCAT sector of the Advanced Photon Source. An 11.35 keV monochromatic X-ray beam was focused down to $30 \times 40 \mu\text{m}^2$ on the sample. Emission was collected through the Be gasket. Collection time was typically 8–16 hours. The spectra have been aligned according to their center of mass relative to a reference spectrum and normalized by total area following the method by Vankó *et al.* [2006]. We used the spectrum of a Fe foil, which has very low satellite peak intensity, for the reference spectrum in the analysis.

The perovskite phase was synthesized by double-sided laser heating at 2000 K for 30 min at 50 GPa using an Nd:YLF laser at APS. In addition, at each pressure above 30 GPa, the sample was scanned with the laser at ~ 1800 K for 15 minutes to synthesize

the stable structure at the new pressure and to anneal deviatoric stress. For SMS above 100 GPa, we did not anneal in order to avoid a phase transition from perovskite to post-perovskite at high temperature [Murakami *et al.*, 2004; Oganov and Ono, 2004; Shim *et al.*, 2004]. Laser annealing was not used on decompression in measurements conducted between 0 and 30 GPa, in order to prevent a phase transition back to a lower-pressure phase.

2.3 Results

2.3.1 Effect of ferric iron on the structure of perovskite

In order to examine the stability of perovskite with $\text{Fe}^{3+}/\Sigma\text{Fe} = 1$, we synthesized perovskite at 45–50 GPa and 2000 K from a crystalline mixture of $0.1\text{Fe}_2\text{O}_3$ hematite + 0.9MgSiO_3 enstatite and $0.9\text{MgSiO}_3 \cdot 0.1\text{Fe}_2\text{O}_3$ glass. After laser heating of the oxide mixture sample, the major diffraction lines are well explained by those of the *Pbnm* perovskite structure, which is consistent with the earlier observation by Andrault and Bolfan-Casanova [2001]. Furthermore, the diffraction patterns of perovskite synthesized from the oxide mixture agree well with those of perovskite synthesized from the glass starting material. These observations suggest the thermodynamic stability of ferric perovskite over a $\text{MgSiO}_3 + \text{Fe}_2\text{O}_3$ mixture. However, we also observed weak diffraction lines from the high-pressure phases of SiO_2 and Fe_2O_3 [Olsen *et al.*, 1991; Kingma *et al.*, 1995; Ono *et al.*, 2004; Shim *et al.*, 2009] in the patterns of perovskite synthesized from the oxide mixture. The existence of these minor lines may be due to inhomogeneity in the laser coupling or inhomogeneity in the sample mixture.

The synthesis of ferric perovskite from glass was performed between 47 and 52 GPa and 2000 K. Pure *Pbnm* perovskite was synthesized without evidence of other minor phases.

Ferric perovskite remains orthorhombic to 106 GPa. In several diffraction patterns there is an unknown line at $\sim 3.4 \text{ \AA}$ that cannot be assigned to perovskite, Au, Ar, Re or any known SiO_2 or Fe_2O_3 phases (Fig. 2-1). It shifts at a much greater rate with pressure than would be expected if it were diffraction from perovskite, which suggests that it is unlikely related to perovskite.

The glass starting material contained a slight excess of Si due to the volatile loss of Mg and Fe^{3+} during the containerless synthesis. Therefore, if the synthesized perovskite has the same cation ratios as the glass starting material, it is possible that the synthesized perovskite has some amount of oxygen vacancies through oxygen vacancy substitution, $\text{Si}_B^{4+} + \frac{1}{2}\text{O}^{2-} = \text{Fe}_B^{3+} + \frac{1}{2}\text{V}_O^0$, where the subscripts denote crystallographic sites and V_O^0 denotes an oxygen vacancy [Navrotsky *et al.*, 2003].

Alternatively, Fe^{3+} can enter perovskite through charge coupled substitution, which will lead to an excess SiO_2 phase coexisting with the perovskite phase for our starting material. Although no SiO_2 phases, stishovite or the CaCl_2 -type, are evident in our diffraction patterns, this does not preclude the existence of an SiO_2 phase as the detection limit is likely $\sim 5\%$. In addition, our SMS and XES suggest approximately equal weighting of Fe^{3+} (see Sections 2.3.2 and 2.3.3) into both the A and B sites of perovskite, which does not support a significant amount of oxygen vacancies. Because computational studies suggested the stabilization of charge coupled substitution over oxygen vacancy substitution for trivalent cations in perovskite at higher pressure [Brodholt, 2000], we synthesized perovskite only above 47 GPa, which would reduce the possibility of oxygen vacancy in ferric perovskite.

We found that Fe^{3+} expands the volume of perovskite relative to Mg-endmember more than Fe^{2+} between 0 and 106 GPa: 17 mol% Fe^{3+} expands the volume at 1 bar (V_0) by 2.1% whereas 15 mol% Fe^{2+} expands it by only 0.6% [Lundin *et al.*, 2008]. At 1 bar, high spin Fe^{3+} is 45% larger than Si^{4+} whereas it is 11% smaller than Mg^{2+} [Shannon, 1976].

Yet, high spin Fe^{2+} is only 3% larger than Mg^{2+} . Therefore, our observation indicates that the expansion of the octahedra has a greater effect on the volume of perovskite than the contraction of the dodecahedra.

Fe^{3+} also increases the axial ratios (c/a and b/a) relative to Mg-endmember perovskite, whereas Fe^{2+} decreases them [Lundin *et al.*, 2008] (Fig. 2-2). This suggests that Fe^{3+} increases the anisotropy of the unit cell of perovskite whereas Fe^{2+} decreases it. Fe^{3+} enters into both the A and B sites, according to our SMS, whereas Fe^{2+} enters only the A site. Therefore, Fe^{3+} will expand the volume of the octahedra, but it is smaller than Mg in the A site, and thus will induce more octahedral tilting, resulting in higher anisotropy of perovskite.

2.3.2 Synchrotron Mössbauer spectroscopy

SMS was performed at a series of pressures between 47 and 136 GPa (Fig. 2-3). The spectra at 47 and 53 GPa consist of only two quantum bits while the spectra at 63 GPa and above consist of four quantum bits with a more regular spacing between 20 and 130 ns, indicating a change in the electronic configuration of Fe^{3+} between 53 and 63 GPa.

In order to extract Mössbauer parameters, the spectra were fit with a two Fe site model. Attempts were made for one and three site models, but the spectra require more than one site and three site models did not improve the fitting. The obtained Mössbauer parameters include the relative site weighting, quadrupole splitting (QS), the full-width at half maximum (FWHM) of the QS , and the relative isomer shift (ΔIS) between the two Fe sites.

The two Fe sites in ferric perovskite show very different QS values, but with a small ΔIS (Fig. 2-4). The QS value can be affected by oxidation state, spin state (high spin and low spin), and coordination state (A and B sites). In this study, all the Fe in perovskite is Fe^{3+} , making QS dependent mainly on spin state and coordination state. In general, low

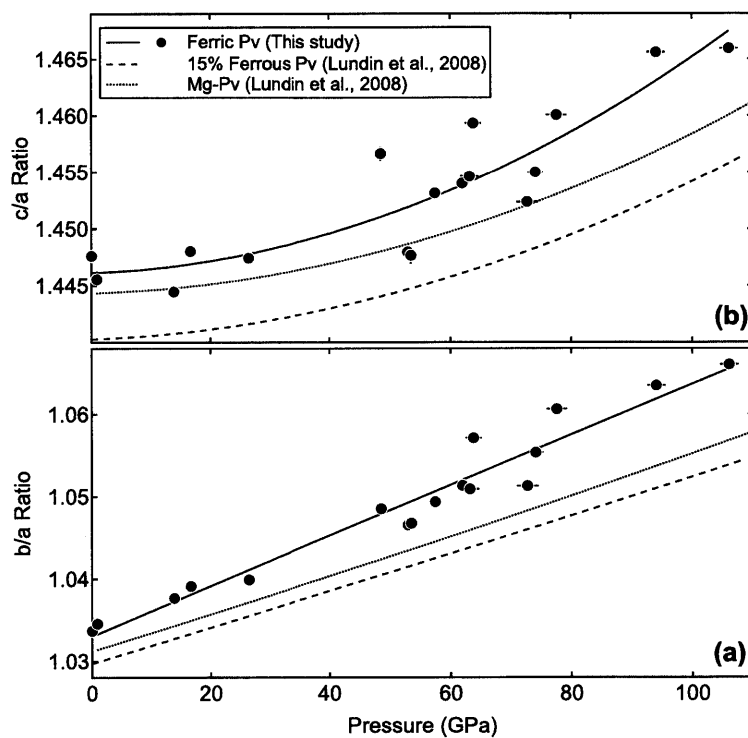


Figure 2-2: Axial ratios, (a) b/a and (b) c/a , of perovskite with different compositions. Ferric perovskite is shown in solid circles, with the solid curves providing a guide for the eye. Ferrous perovskite is shown by the dashed curves, and Mg-endmember perovskite by the dotted curves [Lundin *et al.*, 2008].

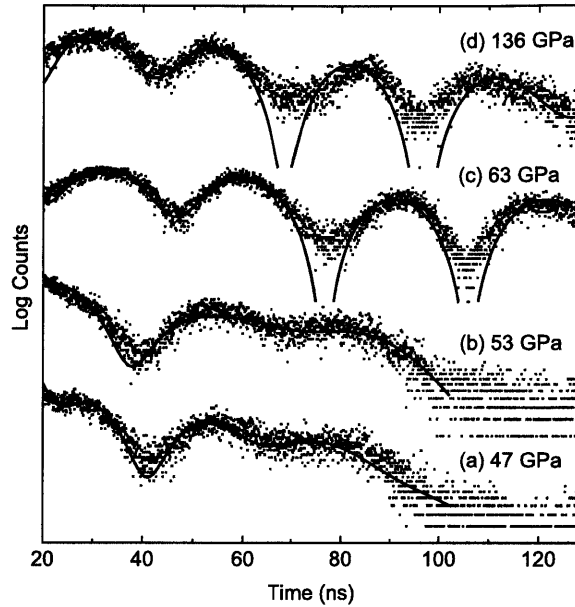


Figure 2-3: Synchrotron Mössbauer spectra of ferric perovskite at high pressure. The data points are shown as dots while the curves are the best fits using CONUSS.

spin Fe^{3+} has a larger QS ($\sim 2.0\text{--}3.5$ mm/s) than high spin Fe^{3+} ($\sim 0.0\text{--}1.5$ mm/s), and increased coordination number also increases QS but to a lesser degree (~ 0.5 mm/s) [Dyar *et al.*, 2006]. Therefore, the two Fe^{3+} sites we identify are distinguished more by their spin state rather than their coordination state and the low and high QS sites are assigned to high spin and low spin Fe^{3+} , respectively.

The visible change in the spectra between 53 and 63 GPa is related to an increase in the weighting of low spin Fe^{3+} relative to high spin, a slight drop in the QS of each site, a drastic reduction in the width of the QS of the high spin site as well as a slight reduction in that of the low spin site, and an increase in ΔIS (Fig. 2-4). No further changes occur in the SMS above 63 GPa up to 136 GPa (Figs. 2-3 and 2-4).

We interpret these observations as following. Below 50 GPa, high spin Fe^{3+} exists in both the A and B sites and low spin Fe^{3+} only exists in the B site. Because coordination

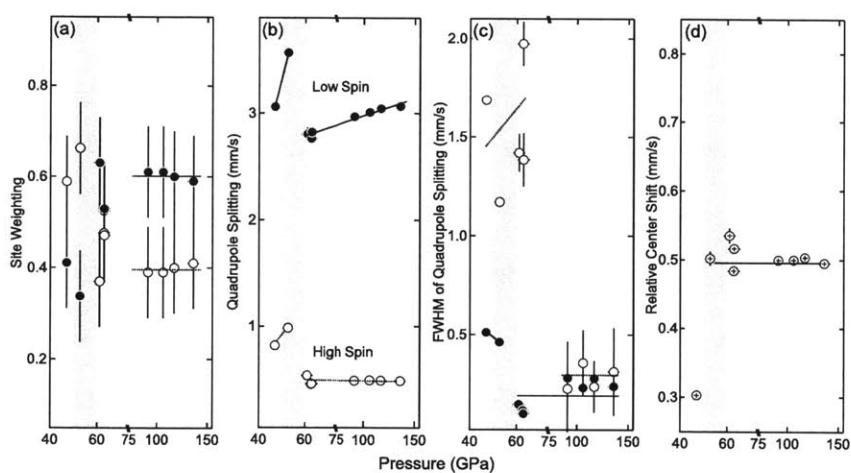


Figure 2-4: Mössbauer parameters from fitting of data with CONUSS: (a) relative site weighting, (b) quadrupole splitting (QS), (c) full width at half maximum or distribution of QS values, and (d) relative isomer shift (ΔIS). Lines are guides for the eye. All parameters for the low spin site are given as solid circles while parameters for the high spin site are given as open circles. Note that the x -axis is split at 75 GPa and scaled differently above and below that pressure. The gray area is the pressure range where we found the completion of the Fe^{3+} spin transition in the B site.

also changes QS but to a lesser degree, the existence of high spin Fe^{3+} in both sites results in the large QS distribution for the high spin Fe^{3+} site. However, because low spin Fe^{3+} exists only in the B site, it has a much smaller QS distribution.

At the transition pressure (P_{tr}), all Fe^{3+} in the B site becomes low spin and the A site is left with only high spin Fe^{3+} (therefore, mixed spin), which makes the distributions of both sites small and similar to each other. This also explains an increase in the relative population of the low spin Fe^{3+} site. The assignment of low spin Fe^{3+} to the B site is also supported by computational predictions [Li *et al.*, 2005a; Stackhouse *et al.*, 2007].

The relative population above 60 GPa remains nearly constant at 60:40, whereas 50:50 is expected if all high spin are in the A site and all low spin are in the B site. The relative population is obtained by assuming the same Mössbauer responses, such as recoil-free fractions, from each site, because no information exists. However, the two sites unlikely have the same Mössbauer responses [Hawthorne, 1988]. A similar degree of offset in the site population was also found in the post-perovskite phase of Fe_2O_3 [Shim *et al.*, 2009] where Fe must exist in two different sites with equal weighting as required by the crystal structure. This example demonstrates that a reasonable uncertainty for this parameter is $\pm 10\%$. The fact that the QS distribution for the low spin and high spin sites becomes essentially the same above the transition suggests that they are in separate crystallographic sites, i.e., the A and B sites of perovskite. In addition, as shown in Section 2.3.3, our XES indicates that the ratio between high spin and low spin Fe^{3+} above 50 GPa is 1:1 within experimental uncertainties. From these results, we conclude that Fe^{3+} substitutes into perovskite through charge coupled substitution ($\text{Mg}_A^{2+} + \text{Si}_B^{4+} \rightarrow \text{Fe}_A^{3+} + \text{Fe}_B^{3+}$) rather than oxygen vacancy substitution.

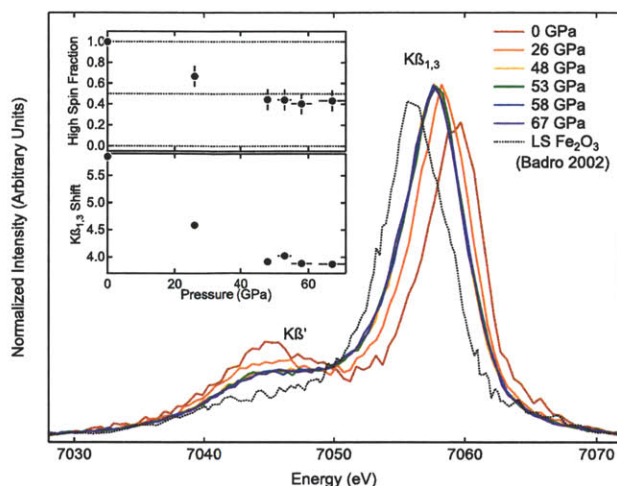


Figure 2-5: X-ray emission spectra of ferric perovskite at high pressure. The dotted curve is the spectrum of low spin Fe_2O_3 at 46 GPa by *Badro et al.* [2002]. The inset shows the high spin fraction obtained from the $\text{K}\beta'$ intensity difference (see the text for method).

2.3.3 X-ray emission spectroscopy

X-ray emission spectra of high spin Fe are characterized by the main $\text{K}\beta_{1,3}$ peak at 7058 eV and the $\text{K}\beta'$ satellite at lower energy which results from the $3p$ core-hole $3d$ exchange interaction during emission (Fig. 2-5). The intensity of the satellite peak is proportional to the spin number of Fe in the sample, with a greater intensity equivalent to a higher spin sample [*Badro et al.*, 1999].

We synthesized perovskite at 50 GPa for XES. Between 48 and 67 GPa, no change in the intensity of $\text{K}\beta'$ was found (Fig. 2-5). Upon decompression there is an increase in the $\text{K}\beta'$ intensity. These observations indicate that the high spin to low spin transition is a progressive transition with pressure up to 48 GPa, above which there is no change in spin. Above 48 GPa, the satellite peak intensity still remains higher than that in Fe_2O_3 with low spin Fe^{3+} at 46 GPa [*Badro et al.*, 2002], suggesting that some Fe^{3+} remains in high spin in this pressure range.

Assuming that the spectrum measured at 0 GPa represents complete high spin Fe^{3+} , we obtained the fraction of high spin Fe^{3+} at high pressure (the inset in Fig. 2-5) using the difference in the satellite peak intensity from that of the low spin Fe_2O_3 spectrum at 46 GPa by *Badro et al.* [2002]. This reveals that the high spin fraction decreases with pressure up to 48 GPa and then remains constant at approximately 50% within experimental uncertainties above the pressure. This is in agreement with our SMS interpretation.

Whereas SMS suggests that the spin transition in the B site completes between 53 and 63 GPa, XES indicates 48 GPa. Considering experimental uncertainties, including different pressure media and different stress conditions along the radial (XES) and axial (SMS) directions of the diamond cell, we believe that the transition pressure likely exists between 48 and 63 GPa. We tentatively assign the transition pressure to 55 GPa.

2.3.4 Equation of state

In order to constrain the equation of state (EOS), we measured the volume of ferric perovskite synthesized from the glass starting material up to 106 GPa (Fig. 2-1). The post-perovskite phase transition has been reported to occur at 100–120 GPa [*Murakami et al.*, 2004; *Mao et al.*, 2004; *Shieh et al.*, 2006; *Shim et al.*, 2008]. As such, our data collected after heating above 106 GPa appears to be within the perovskite + post-perovskite mixed phase region during laser heating. Therefore, we restrict our data presented to those inside the perovskite stability field. Note that all the data points used for EOS fits are obtained after laser annealing to 2000 K except for the data points below 25 GPa. In order to prevent synthesis of a low-pressure phase, we did not laser anneal the samples below 25 GPa.

Fitting all of the P - V data between 0 and 106 GPa to the third-order Birch-Murnaghan (BM) equation gives a bulk modulus of $K_0 = 228 \pm 5$ GPa at 1 bar, with a pressure derivative of $K'_0 = 4.5 \pm 0.3$ for V_0 fixed to $165.78 \pm 0.03 \text{ \AA}^3$, which was measured in this study. The

K_0 and K'_0 of ferric perovskite are significantly lower and higher, respectively, than those of Mg-endmember and ferrous perovskite measured by *Lundin et al.* [2008] using the same Au scale. This comparison indicates that Fe^{3+} makes perovskite more compressible at lower pressure but less compressible at higher pressure.

In order to explore where the compressibility of ferric perovskite changes with respect to ferrous perovskite, we calculated the differences between the measured volume of ferric (17 mol%) perovskite and the EOS of ferrous (15 mol%) perovskite [*Lundin et al.*, 2008], $V(\text{ferric Pv}) - V(\text{ferrous Pv})$ (open squares in Fig. 2-6b). The volume difference decreases with pressure below 55 GPa, suggesting that the compressibility of ferric perovskite is higher than ferrous perovskite. Above 55 GPa, the volume difference increases with pressure, indicating that ferric perovskite becomes less compressible. In other words, the compressibility changes near the pressure range where our SMS and XES results indicate the completion of the high-spin \rightarrow low spin transition in the B site. However, some systematic trends still remain in the fit residual (open circles in Fig. 2-6b).

In order to examine the statistical significance of the systematic trend observed in $V(\text{ferric Pv}) - V(\text{ferrous Pv})$ and the fit residual, we consider all the possible uncertainty sources. The largest source is from the uncertainty in the absolute pressure scale, which should be $\sim 5\%$. However, by using the same pressure scale and comparing only the relative offset, we can avoid the problem of uncertainty in the absolute scale. However, the pressure error bars estimated from the standard deviation of pressures from different diffraction lines are still significantly larger than the volume uncertainties estimated from unit-cell fitting. Therefore, we propagated the uncertainty in pressure using $\sigma(\Delta V)^2 = \sigma(V)^2 + \sigma(P)^2(V/K)^2$ and presented them in Fig. 2-6b. Even after considering this uncertainty, the trend in $V(\text{ferric Pv}) - V(\text{ferrous Pv})$ and the residual after fitting the entire dataset with one BM equation remain significant (the open squares and circles, respectively,

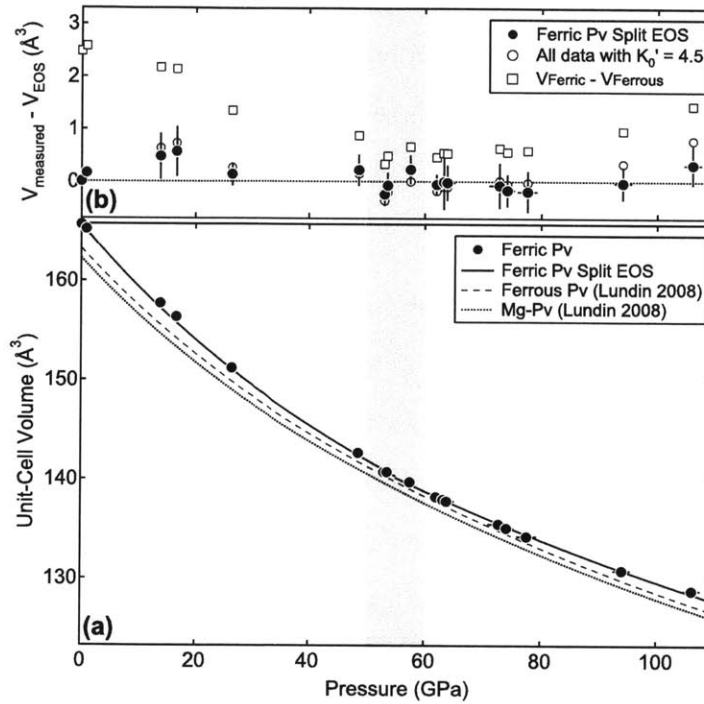


Figure 2-6: (a) Measured volume of ferric perovskite (black circles). The solid curve shows the EOS fit split at 55 GPa. Error bars are given as 1σ . Also shown for comparison are the EOSs of MgSiO_3 perovskite (dotted curve) and $(\text{Mg}_{0.85}, \text{Fe}_{0.15})\text{SiO}_3$ (dashed curve) [Lundin *et al.*, 2008]. (b) Difference between the measured data and EOS fits. The solid and open circles are the residuals for the split EOS fit and the whole fit, respectively. The open squares are the volume difference between ferric and ferrous perovskite. The error bar for ΔV estimated from both pressure and volume are shown for our best fit only. However, the same error bar can be applied also for the other fit residuals. The gray area is the pressure range where we found the completion of the Fe^{3+} spin transition.

in Fig. 2-6b).

Because the spin transition is completed and the trend in $V(\text{ferric Pv}) - V(\text{ferrous Pv})$ changes near 55 GPa, we fit our P - V data with two different pressure ranges, above and below 55 GPa. Because of the strong correlation between K_0 and K'_0 [Bell *et al.*, 1987], the second-order BM equation is used for both pressure ranges. The method described in Sata *et al.* [2002] and Shim *et al.* [2008] was used by setting the reference state at 55 GPa instead of 1 bar, because V_0 for the trend above 55 GPa is unknown. This attempt further improves the fitting over using the entire pressure range in one EOS, even though K'_0 is fixed to 4. We obtained $K_{55 \text{ GPa}} = 439 \pm 2 \text{ GPa}$ for the lower-pressure data and $K_{55 \text{ GPa}} = 501 \pm 17 \text{ GPa}$ for the higher-pressure data, which is a $14 \pm 4\%$ increase in bulk modulus at the spin transition. However, density does not change at 55 GPa (Fig. 2-7a,b). The fit residual of this scheme is significantly less systematic and close to 0 considering the uncertainty, suggesting that this scheme is statistically superior to the former.

When the latter fitting results are projected to 1 bar, we obtained $K_0 = 237 \pm 3 \text{ GPa}$ for the lower-pressure data and $K_0 = 304 \pm 20 \text{ GPa}$ for the higher-pressure data. Compared with the bulk moduli of 15 mol% ferrous and Mg-endmember perovskite, 259–261 GPa [Lundin *et al.*, 2008], which used the same pressure scale and the same pressure medium, this fitting result suggests that Fe^{3+} makes perovskite more compressible during the spin transition, but less compressible after the completion of the spin transition. Below 55 GPa, compression in ferric perovskite is accommodated by both lattice compression and the gradual spin collapse of Fe^{3+} in the B site. For comparison, across the spin transition in ferroperriclite, the size of Fe^{2+} appears to decrease by 10% [Fei *et al.*, 2007]. Therefore, these compressional mechanisms at low pressure would result in a greater compressibility of the structure during the gradual spin transition. After the completion of the gradual Fe^{3+} spin transition in the B site, volume reduction is only achieved by lattice compression,

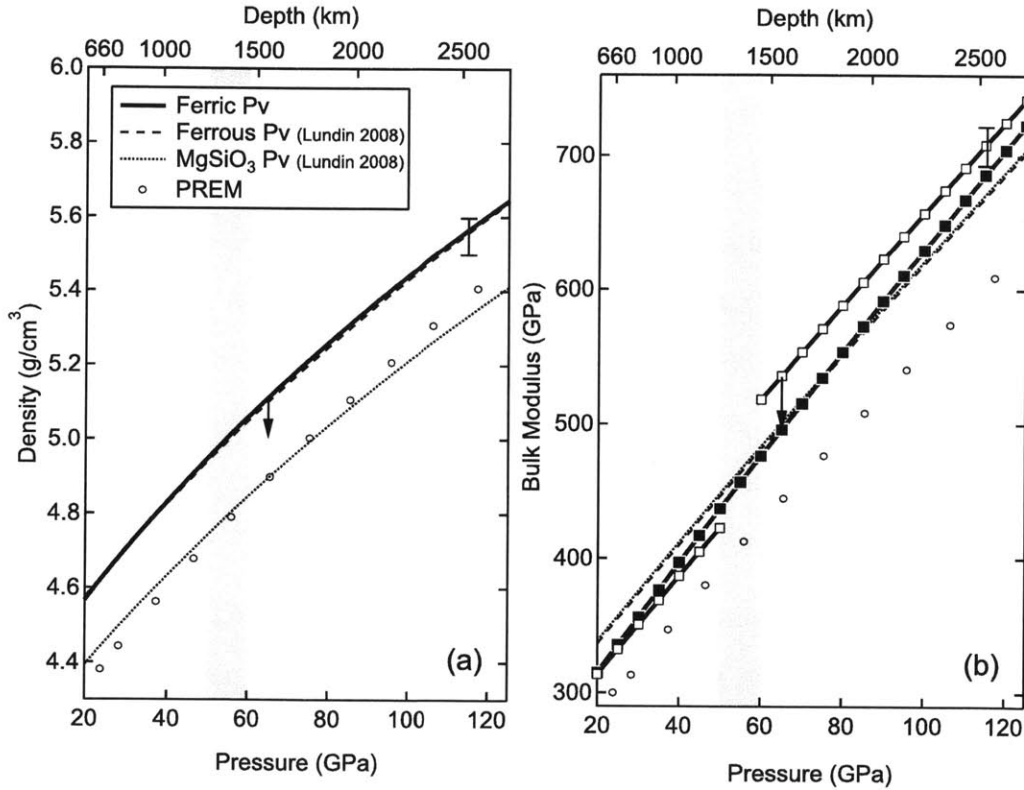


Figure 2-7: Profiles of (a) density and (b) bulk modulus for ferric perovskite data (solid curves), ferrous perovskite (dashed curves), and Mg-endmember perovskite (dotted curves) [Lundin *et al.*, 2008], and PREM [Dziewonski and Anderson, 1981] (open circles). Note that the profiles for perovskite are calculated at 300 K. The arrows shown represent the expected thermal effect at 2000 K on these parameters for Mg-endmember perovskite [Fiquet *et al.*, 2000]. The gray area is the pressure range where we found the completion of the Fe³⁺ spin transition.

which is reflected by the increase in bulk modulus after the spin transition.

2.4 Implications for the spin state of Fe in perovskite

Our results provide useful information for the spin state of Fe in perovskite, which has recently been a subject of much debate [Badro *et al.*, 2004; Li *et al.*, 2004; Jackson *et al.*, 2005; Lin *et al.*, 2008; McCammon *et al.*, 2008]. Badro *et al.* [2004] proposed a two step decrease in the satellite peak intensity in the XES of Al-free perovskite. Interpretation of the two step process was difficult because of the coexistence of Fe²⁺ and Fe³⁺. Interestingly, the pressure range where the first drop was observed (40–60 GPa) coincides with the pressure range where we observed a gradual spin transition of Fe³⁺ in the B site. Therefore, the drop in the high spin population at lower pressure observed by Badro *et al.* [2004] may be related to the spin transition of Fe³⁺.

In contrast, Li *et al.* [2004] reported a gradual loss of spin in Al-bearing perovskite in their XES measurements. As discuss in Section 2.5, site mixing between Fe³⁺ and Al could leave the Fe³⁺ spin transition unfinished in the mantle pressure range and therefore result in a continuous decrease in the high spin population. Li *et al.* [2004] also proposed a gradual loss for Al-free perovskite which is in disagreement with the results of Badro *et al.* [2004]. However, the smaller pressure range and fewer data points for Al-free perovskite in Li *et al.* [2004] make comparison difficult. Also, Badro *et al.* [2004] annealed perovskite, whereas Li *et al.* [2004] did not, which could result in the difference.

Jackson *et al.* [2005] reported a gradual decrease in relative *IS* below 70 GPa where *IS* becomes insensitive to pressure in their SMS of perovskite. They interpreted that the change might be related to a spin transition in Fe³⁺. In fact, our results confirm this interpretation. We note that our measurements make unambiguous interpretation possible as

perovskite contains only Fe^{3+} in our study.

2.5 Implications for the lower mantle

Some recent studies have suggested that mantle perovskite may contain a significant amount of Fe^{3+} due to crystal chemistry effects at high pressure [McCammon, 1997; Frost *et al.*, 2004], which may have important implications for core formation, the scale of mantle mixing, and the oxidation state of the mantle [McCammon, 2005; Wood *et al.*, 2006].

In Fig. 2-7, we compare the density and bulk modulus of ferric perovskite with those of ferrous perovskite and the Earth's lower mantle, taken from the Preliminary Reference Earth Model (PREM) [Dziewonski and Anderson, 1981]. Because our measurements are conducted at 300 K, we present profiles at 300 K. For better comparison with PREM, the black arrow in each figure shows the approximate thermal effect (2000 K) (Fig. 2-7) which was calculated based on the thermal parameters for Mg-endmember perovskite [Fiquet *et al.*, 2000; Shim and Duffy, 2000]. As found in our study, the completion of the Fe^{3+} spin transition at 55 GPa does not result in a noticeable effect on density, but does cause a discontinuous increase in bulk modulus.

Because the spin transition of Fe^{3+} occurs only in the B site, it is important to know whether mantle silicate perovskite contains Fe^{3+} in the B site. A single crystal study at 1 bar suggested that Fe^{3+} may exist only in the A site whereas Al preferentially enters the B site through charge coupled substitution [Vanpeteghem *et al.*, 2006b]. This is perhaps due to the much larger size of high spin Fe^{3+} relative to Al, which is 15–20% according to Shannon [1976]. However, after the spin transition at high pressure, low spin Fe^{3+} is essentially the same size as Al, only about 2% larger [Shannon, 1976]. Therefore, they are likely to compete for the B site at high pressure. Our preliminary SMS results for

perovskite with equal amounts of Fe^{3+} and Al show that $20 \pm 10\%$ of Fe^{3+} exists in the B site at 50–70 GPa, supporting this argument (Catalli et al., 2010, in preparation).

However, the addition of Al into perovskite, as expected for the Earth, would make the effect of the spin transition less pronounced. Mantle perovskite likely has about 10 mol% Fe, with 60% of that as Fe^{3+} [McCammon, 1997], which leaves 6% Fe^{3+} in perovskite. From our SMS on Fe^{3+} ,Al-bearing perovskite, 20% of this should exist in the B site, and thus become low spin. Therefore, the elasticity change due to the completion of Fe^{3+} spin transition would result in a $0.5 \pm 0.2\%$ increase in bulk sound speed in a mantle relevant composition.

The pressure where the spin transition of Fe^{3+} is completed would certainly change with composition and temperature. Since temperature results in expansion of the unit cell, and because the spin transition is volume driven, temperature may suppress the transition to deeper in the mantle [Sturhahn et al., 2005; Hofmeister, 2006].

A recent computational study predicted that the spin transition pressure decreases with an increase in Fe^{2+} in perovskite [Bengtson et al., 2008]. Yet, it is unclear how the change in the concentration of Fe^{3+} would change the transition pressure. Furthermore, as Al would be coupled with Fe^{3+} , its effect may play a significant role in the transition pressure.

An important question for geophysical application is whether the bulk modulus increase, or bulk sound speed increase, would remain sharp at lower-mantle temperature. In ferropericlase (Fp), high temperature spreads out the spin transition of Fe^{2+} over a wider pressure range due to the entropy effect [Sturhahn et al., 2005; Lin et al., 2007]. In perovskite, some studies have suggested that the presence of diverse Fe environments in perovskite would make the transition broad. Computational studies showed the existence of different short range Fe ordering with similar energies and therefore the transition in Fe in perovskite may be broad [Li et al., 2005a; Stackhouse et al., 2007]. We have shown that the

Fe^{3+} spin transition is gradual, taking place between 0 and 55 GPa. However, unlike Fp [Fei *et al.*, 2007], the compressibility of perovskite changes at the completion of the spin transition of Fe^{3+} . Therefore, it is likely that the change in compressibility will remain sharp, even at high temperature.

The presence of Al, though, could make the transition gradual. Because low spin Fe^{3+} becomes similar in size to Al, they are likely to compete for the B site at high pressure, as supported by our preliminary SMS results. As a result, the population of Fe^{3+} in the B site could continuously increase with pressure as the spin transition proceeds. If so, the population of low spin Fe^{3+} in the B site would increase with pressure and it is possible that the spin transition may never complete at mantle pressures. If so, no sharp transition would occur in the mantle, but this would result in perovskite with Fe^{3+} and Al having a lower bulk modulus than Mg-endmember or ferrous perovskite throughout the lower mantle due to the gradual volume decrease in Fe^{3+} through the spin transition. A study on perovskite with both Fe^{3+} and Al [Nishio-Hamane *et al.*, 2008] suggested only a slight decrease in bulk modulus, but it is important to heat perovskite to sufficiently high temperature for longer duration in order to reach equilibrium for the site mixing between Fe^{3+} and Al.

If the transition is sharp in the mantle, it would result in a velocity discontinuity (but without a density change) in the mid lower mantle, providing a useful probe for the existence of Fe^{3+} in the lower mantle. The transition might be more intense where the concentration of Fe^{3+} is enhanced in perovskite. As the amount of Fe^{3+} may be increased with Al [McCammon, 1997], the most likely place for a sharp transition would be the regions with enhanced amounts of basaltic materials, suggesting that our findings can be useful for understanding mantle heterogeneities. As yet unexplained discontinuities do exist in the mid lower mantle [Kawakatsu and Niu, 1994; Stunff *et al.*, 1995; Shen *et al.*, 2003; Courtier and Revenaugh, 2008].

If the transition is gradual in the Earth's mantle, it will effect the velocity profile at the mid to lowermost mantle. The composition of the lower mantle can be constrained by comparing laboratory measured density/velocity profiles to seismic profiles [Stixrude *et al.*, 1992]. Therefore, a change in the velocity profile by the spin transition of Fe^{3+} in perovskite would affect the estimation.

2.6 Conclusions

X-ray emission spectroscopy on Fe^{3+} -bearing MgSiO_3 perovskite reveals a spin transition from high-spin to mixed spin completing near 55 GPa. Synchrotron Mössbauer spectroscopy results demonstrate that Fe^{3+} in the B site of perovskite undergoes a gradual spin transition to 55 GPa where all Fe^{3+} in the B site becomes low-spin. However, Fe^{3+} in the A site remains high-spin throughout lower-mantle pressures. Our volume measurements at high pressure indicate that there is no discontinuous change in the density of ferric perovskite associated with the completion of the spin transition. However, our equation of state fitting indicates that the bulk modulus increases at the completion of the spin transition. In addition, we found that the charge coupled substitution of $\text{Fe}^{3+} - \text{Fe}^{3+}$ for Mg–Si increases the orthorhombic distortion of the perovskite structure, in contrast to substituting predominantly Fe^{2+} for the A site which reduces the distortion. The elasticity change found at the completion of the Fe^{3+} spin transition can be a useful probe for seismic investigations of the oxidation state of Fe and compositional heterogeneities in the lower mantle.

Table 2.1: Unit-cell volumes and lattice parameters of Fe³⁺-Pv at high pressure. Pressure was determined using the equation of state of gold [Tsuchiya, 2003].

P (GPa)	a (Å)	b (Å)	c (Å)	V (Å ³)
0.0 (2)	4.8028 (9)	4.9646 (6)	6.953 (1)	165.78 (3)
0.9 (3)	4.7992 (11)	4.9651 (8)	6.938 (2)	165.31 (5)
13.8 (16)	4.7213 (11)	4.8992 (11)	6.820 (2)	157.74 (5)
16.6 (18)	4.7014 (10)	4.8852 (10)	6.808 (1)	156.36 (4)
26.4 (10)	4.6489 (9)	4.8344 (8)	6.729 (1)	151.23 (3)
48.5 (17)	4.5373 (11)	4.7574 (9)	6.609 (2)	142.67 (4)
53.0 (13)	4.5286 (10)	4.7393 (9)	6.557 (2)	140.73 (4)
53.5 (15)	4.5286 (18)	4.7403 (10)	6.556 (2)	140.73 (5)
57.5 (20)	4.5082 (10)	4.7307 (9)	6.551 (2)	139.72 (4)
62.0 (14)	4.4884 (7)	4.7187 (9)	6.526 (1)	138.22 (3)
63.2 (30)	4.4854 (14)	4.7137 (11)	6.525 (2)	137.95 (4)
63.8 (26)	4.4699 (9)	4.7251 (11)	6.523 (1)	137.78 (3)
72.7 (36)	4.4604 (11)	4.6892 (11)	6.478 (1)	135.49 (4)
74.1 (25)	4.4474 (11)	4.6935 (12)	6.471 (1)	135.07 (4)
77.6 (34)	4.4256 (10)	4.6939 (10)	6.462 (1)	134.24 (3)
94.0 (30)	4.3781 (11)	4.6561 (14)	6.417 (2)	130.80 (4)
106.1 (30)	4.3516 (9)	4.6390 (11)	6.379 (1)	128.78 (3)

Table 2.2: Fitting results for the Mössbauer spectrum of Fe^{3+} -Pv. QS : quadrupole splitting in mm/s, FWHM: distribution of QS in mm/s, IS : isomer shift relative to iron and ΔIS : isomer shift difference between sites 1 and 2 in mm/s. Parameters with error values were varied. The uncertainties are given in parentheses at the 90% confidence level for the last reported significant digit(s). The weights are normalized, and therefore one of the weights is given without errors.

P (GPa)	Site 1				Site 2				ΔIS
	Weight	QS	FWHM	IS	Weight	QS	FWHM	IS	
47 (1)	0.411 (4)	3.06 0.01	0.511 (7)		0.589	0.820 (5)	1.69 (2)		0.303 (6)
53 (2)	0.338 (8)	3.57 0.02	0.462 (10)		0.662	0.985 (5)	1.17 (1)		0.502 (10)
61 (2)	0.630 (14)	2.81 0.06	0.148 (18)		0.370	0.540 (1)	1.42 (9)		0.535 (11)
63 (2)	0.524 (7)	2.76 0.05	0.118 (7)		0.476	0.458 (1)	1.97 (11)		0.484 (4)
63 (2)	0.529 (7)	2.82 0.04	0.101 (11)		0.471	0.463 (1)	1.38 (13)		0.516 (5)
91 (3)	0.610 (8)	2.97 0.02	0.281 (185)		0.390	0.490 (1)	0.23 (23)		0.499 (4)
106 (3)	0.610 (10)	3.01 0.00	0.232 (5)	1.56	0.390	0.493 (4)	0.36 (17)	1.28	0.499 (5)
117 (4)	0.600 (7)	3.05 0.00	0.279 (4)	1.63	0.400	0.490 (3)	0.24 (13)	1.38	0.503 (4)
136 (4)	0.590 (8)	3.07 0.01	0.239 (6)	1.62	0.410	0.489 (4)	0.31 (22)	1.36	0.495 (5)

X-ray diffraction and Mössbauer spectroscopy of ferric iron-bearing post-perovskite

K. Catalli, S.-H. Shim, V.B. Prakapenka, J. Zhao, and W. Sturhahn (2010). X-ray diffraction and Mössbauer spectroscopy of Fe³⁺-bearing Mg-silicate post-perovskite at 128-138 GPa. American Mineralogist, 95, 418-421.

Abstract

The effect of ferric iron on the properties of Mg-silicate post-perovskite were studied up to 138 GPa using synchrotron X-ray diffraction and Mössbauer spectroscopy. Our diffraction measurements revealed that the incorporation of Fe³⁺ has virtually no effect on the volume of post-perovskite, in contrast to Fe²⁺ which increases the volume. Therefore, incorporation of Fe³⁺ increases the density of post-perovskite much more effectively than Fe²⁺. Mössbauer spectroscopy suggests that Fe³⁺ enters post-perovskite through charge-coupled substitution, and is high spin in the bipolar prismatic site and low spin in the octahedral site (i.e., mixed spin state). Our results may have important implications for the gravitational stability of lower-mantle heterogeneities.

3.1 Introduction

The D'' region is a seismically distinct layer at the lower 200–400 km of the mantle that has been known for decades [Lay *et al.*, 1998]. Only in recent years was Mg-silicate perovskite, the dominant phase of the lower mantle, found to undergo a phase transformation to the so-called post-perovskite phase at pressures related to the D'' discontinuity [Murakami *et al.*, 2004; Oganov and Ono, 2004; Shim *et al.*, 2004]. Since then, many studies have attempted to reconcile the seismic features at the lowermost mantle with the properties of the post-perovskite phase.

For example, the anticorrelation between shear (V_S) and bulk sound velocity (V_Φ) anomalies has been related to the physical properties of the post-perovskite phase [Oganov and Ono, 2004; Wookey *et al.*, 2005]. However, some seismic studies have indicated that the anticorrelation can be observed from a much shallower depth than the post-perovskite transition, suggesting that compositional variation at the lowermost mantle may still play an important part [Hernlund and Houser, 2008]. Furthermore, the observation of the large low shear velocity provinces, which extend to well above the expected depth for the post-perovskite transition, with sharp lateral boundaries [Ni *et al.*, 2002], appears to be more consistent with compositional changes. Therefore, it is important to understand compositional effects on the properties of post-perovskite.

Iron is an important cation in mantle silicates and oxides. Recent studies [McCammon, 1997; Sinmyo *et al.*, 2006] have suggested that a significant amount of Fe in lower mantle silicates can be Fe³⁺ due to crystal chemistry effects at high pressure. In addition, Fe³⁺ concentration appears to increase with the presence of Al to $\text{Fe}^{3+}/\Sigma\text{Fe} \simeq 0.6$ [McCammon, 1997]. Al is particularly enriched in basaltic materials in the lower mantle. Therefore, it is important to understand the effects of valence state changes in Fe on the physical properties

of the lower mantle silicates.

Here we report the volume of Fe³⁺-bearing post-perovskite (hereafter Fe³⁺-PPv) measured within its stability field using synchrotron X-ray diffraction (XRD). Our synchrotron Mössbauer spectroscopy (SMS) reveals the spin state of Fe³⁺ in post-perovskite, which is important for understanding the physical property changes due to the valence state change in Fe.

3.2 Experimental

The starting material was a glass synthesized using the containerless laser levitation method [Tangeman *et al.*, 2001] in an O₂ atmosphere. This material is also used for studying the effects of Fe³⁺ on perovskite [Catalli *et al.*, 2010b]. Electron microprobe measurements show that the starting material is MgSiO₃ with 17 mol% of Fe₂O₃ (95% enriched in ⁵⁷Fe). The amount of oxygen and iron measured using electron microprobe indicates that all Fe is Fe³⁺.

The glass was ground to a powder and mixed with 10 wt% Au for use as an internal pressure standard [Tsuchiya, 2003] for the XRD study. For SMS, the sample was not mixed with Au, but instead pressure was measured using the first-order Raman mode of diamond, the anvil material [Akahama and Kawamura, 2006]. Symmetric type diamond-anvil cells (DAC) were used with diamonds with 150 μm beveled culets. The sample powder was pressed to a foil of ~10 μm thickness, and loaded into a preindented Re gasket. Ar was cryogenically loaded into the DAC, acting as both an insulating and a pressure medium. A few spacer grains of the starting material were used to keep the sample foil from having direct contact with the diamond anvils.

The advanced flat-top, double-sided laser heating system at the GSECARS sector of the

Advanced Photon Source (APS) was used to heat the sample to temperatures up to 3000 K [Prakapenka *et al.*, 2008]. The two diode-pumped fiber lasers were focused on both sides of the sample in the DAC. The size of the flat-top heating spot was about 20–30 μm , comparable to the sample size.

Angle-dispersive XRD was performed at the GSECARS sector using a monochromatic X-ray beam with energy of 40 keV, focused to a size of $5 \times 5 \mu\text{m}^2$. Diffraction images were collected using a MarCCD detector. A total of 12–23 diffraction lines were used to constrain the volume of post-perovskite using the UnitCell program [Holland and Redfern, 1997]. The volume of Au, constrained by 2–3 diffraction lines, was used for calculating pressure using the scale of Tsuchiya [2003]. Pressure uncertainty is given as the 1σ standard deviation among the pressures obtained from individual diffraction lines.

SMS was performed at Sector 3 of APS. The X-ray beam was focused to an area of $6 \times 6 \mu\text{m}^2$. The storage ring was operated in top-up mode with 23 bunches separated by 153 ns. Nuclear resonant scattering was measured in a time window of 15–130 ns following excitation. Data collection took 2 hours [see Catalli *et al.*, 2010b; Shim *et al.*, 2009, for more information]. The spectra was fit using the CONUSS package [Sturhahn, 2000].

3.3 Results

To synthesize post-perovskite, pressure was first increased to 139 GPa. The sample was then heated at 2400–3000 K for 30 minutes. After thermal quenching pressure had dropped to 125 GPa and the sample consisted of a mixture of perovskite and post-perovskite. Pressure was increased again to 145 GPa and the sample was then heated at 2200–3000 K for another 30 minutes, during which the sample was converted to pure post-perovskite (Fig. 3-1). Pressure dropped to 138 GPa after heating. No other phases, including SiO_2 , Fe_2O_3 ,

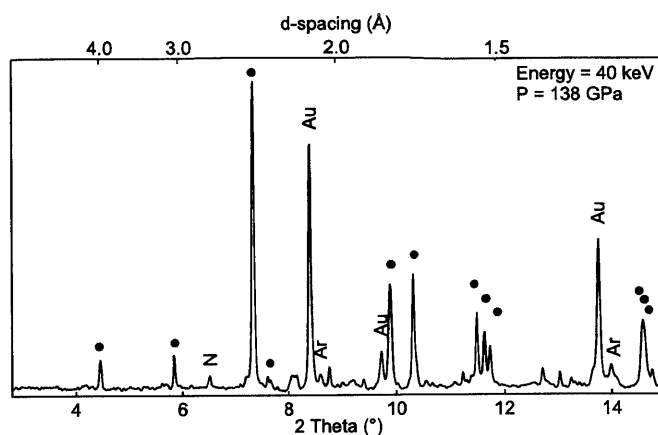


Figure 3-1: Representative XRD pattern of post-perovskite at high pressure. Triangles show key diffraction lines of post-perovskite (Ar, argon pressure medium; Au, gold pressure standard; N, nitrogen). The background is subtracted.

and MgO, were identified.

The volume of post-perovskite was measured during decompression between 138 and 42 GPa (Fig. 3-2 and Tab. 3.1). The sample was not annealed during decompression in order to prevent back transformation to the perovskite phase. Measurements made below 130 GPa are characterized by significant line broadening and volumes deviating from the higher-pressure trend. Similar trends were also found in Fe^{2+} -PPv [Shim *et al.*, 2008] and were attributed to the combined effects of deviatoric stresses and being out of the post-perovskite stability field. In this study, only data collected above 130 GPa was used.

The most notable difference between Fe^{3+} -PPv and Fe^{2+} -PPv is that Fe^{3+} has very little effect on the volume of post-perovskite: the volume of Fe^{3+} -PPv is very similar to the volume of Mg end member post-perovskite [Guignot *et al.*, 2007] whereas 9 mol% Fe^{2+} expands the volume by 0.7% [Shim *et al.*, 2008] (Fig. 3-2). Guignot *et al.* [2007] used a different pressure scale, which may introduce some uncertainty in comparing with Mg end member post-perovskite. However, the comparison between Fe^{3+} -PPv and Fe^{2+} -

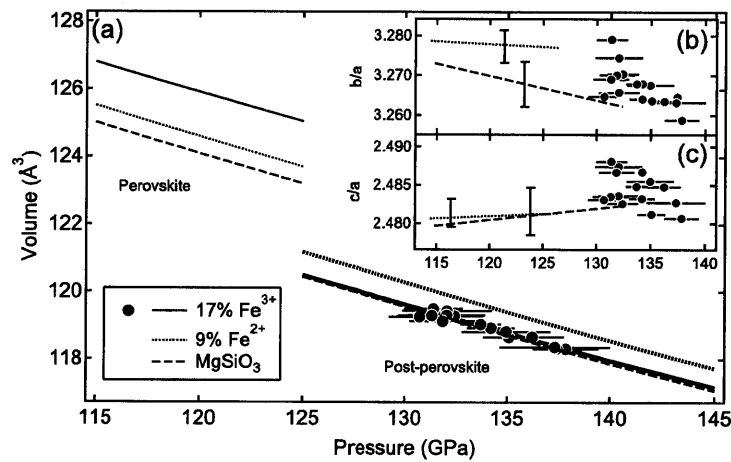


Figure 3-2: (a) Pressure–volume data for Fe^{3+} -PPv (solid circles) and its EOS (bold solid line). We also show the EOS for Fe^{3+} -Pv of the same composition [light, solid line, *Catalli et al.*, 2010b], 9% Fe^{2+} -Pv [light, dotted line, *Lundin et al.*, 2008], 9% Fe^{2+} -PPv [bold, dotted line, *Shim et al.*, 2008], MgSiO_3 -Pv [light, dashed line, *Lundin et al.*, 2008], and MgSiO_3 -PPv [bold, dashed line, *Guignot et al.*, 2007]. Note that all data sets were measured in an Ar medium, using the Au scale of *Tsuchiya* [2003] except for the MgSiO_3 -PPv data [*Guignot et al.*, 2007] which was measured in NaCl medium with the MgO pressure scale [*Speziale et al.*, 2001]. The inset shows the (b) b/a and (c) c/a ratios of post-perovskite. The vertical bars in the insets show the data scatter.

PPv is robust because these two datasets are based on the same pressure scale and pressure medium. The volume of Fe³⁺-PPv is smaller than 9 mol% Fe²⁺-PPv even though it has a larger Fe content (17 mol%), supporting that Fe³⁺ may have a very small effect on the volume of post-perovskite and therefore very large effects on the density.

Catalli et al. [2010b] found that Fe³⁺ in the octahedral site of perovskite undergoes a gradual high-spin → low-spin transition up to 55 GPa. They also found that the completion of the spin transition makes the perovskite phase less compressible. This stiffening of Fe³⁺-Pv results in a larger volume than Fe²⁺-Pv at the lowermost mantle. Combined with the small effect of Fe³⁺ on the post-perovskite volume, this results in an increased magnitude of the volume decrease at the post-perovskite transition: only $\Delta V/V = 1.7\%$ in the Fe²⁺ bearing system, whereas $\Delta V/V = 3.6\%$ in the Fe³⁺ bearing system at 125 GPa.

Because of the narrow pressure range where the volume measurements were made in addition to V_0 being unknown, it is difficult to constrain the compressibility of Fe³⁺-PPv. In order to reduce the uncertainty, by taking 137.9 GPa as the reference pressure, where an actual data point exists, we conducted equation of state (EOS) fitting to the second order Birch-Murhanhan equation (the fitting scheme is reported in *Sata et al.* [2002] and *Shim et al.* [2008]). This yields $K_{138 \text{ GPa}} = 724 \pm 30 \text{ GPa}$ for $V_{138 \text{ GPa}} = 118.30 \pm 0.01 \text{ \AA}^3$ (at 125 GPa, $K = 682 \text{ GPa}$, $V = 120.5 \text{ \AA}^3$), which are similar to those reported on Fe²⁺-bearing post-perovskite [*Shim et al.*, 2008], suggesting the compressibility of post-perovskite may not be affected significantly by a change in the valence state of Fe.

It has been shown that the high-spin → low-spin transition in Fe³⁺ [*Catalli et al.*, 2010b] and the substitution mechanism of trivalent cations [*Brodholt*, 2000] can affect the density of mantle silicates at high pressure. Therefore, we conducted SMS measurements at 128 GPa on a Fe³⁺-PPv sample to understand Fe³⁺ site occupancy and spin state (Fig. 3-3). Our XRD pattern of the sample shows that the sample is mostly post-perovskite with a

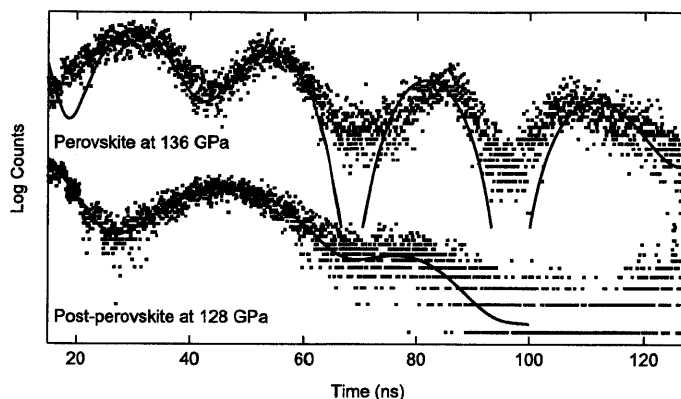


Figure 3-3: Synchrotron Mössbauer spectra of Fe^{3+} perovskite + post-perovskite mixture at 128 GPa (bottom) and Fe^{3+} -Pv at 136 GPa (top). Black lines show the fits from CONUSS.

small amount of perovskite, found to be about 17% from our SMS spectral fit, due to incomplete transformation. Because the Mössbauer spectrum of pure Fe^{3+} -Pv was measured and fitted at a similar pressure (136 GPa) [Catalli *et al.*, 2010b] (Fig. 3-3), we fixed the Mössbauer parameters of Fe^{3+} -Pv in the spectral fitting, while allowing the post-perovskite parameters and the relative proportion of post-perovskite to perovskite to vary (Tab. 3.2). We attempted a single-site model for post-perovskite but it did not explain the observed spectral features. Introducing more than 2 sites may not be statistically reasonable for the given resolution of the data.

Our SMS suggests that Fe^{3+} enters into two different sites in post-perovskite with a 6:4 ratio (Tab. 3.2). This is in reasonable agreement with expected equal partitioning of Fe^{3+} into the bipolar prismatic (Mg) and octahedral (Si) sites in post-perovskite, as supported by computational results which suggested the stability of charge-coupled substitution of trivalent cations over oxygen vacancy substitution at the lowermost mantle [Zhang and Oganov, 2006]. A 6:4 site weighting ratio was also found in a SMS study on the post-perovskite phase of Fe_2O_3 [Shim *et al.*, 2009] which should have a 1:1 ratio, required by stoichiometry. A similar trend was also found in Fe^{3+} -Pv [Catalli *et al.*, 2010b] (Tab. 3.2), where X-ray

emission spectroscopy supported a 1:1 ratio between Fe^{3+} in the two sites. Therefore, our post-perovskite results can be regarded as in good agreement with the charge-coupled substitution of Fe^{3+} in post-perovskite.

Fe^{3+} -PPv has one high quadrupole splitting (QS) site and one low QS site, similar to Fe^{3+} -Pv [Catalli *et al.*, 2010b] (Tab. 3.2). The low QS value is consistent with that of high-spin Fe^{3+} [Dyar *et al.*, 2006]. Low-spin Fe^{3+} is expected to have higher QS value [Hawthorne, 1988]. Low-spin Fe^{3+} found in the rare earth orthoferrite perovskites has $QS = 2.4$ mm/s [Xu *et al.*, 2001], which is similar to the value for the high QS site. Therefore, the high and low QS sites can be attributed to low-spin and high-spin Fe^{3+} , respectively.

Because the size of low-spin Fe^{3+} is smaller than high-spin Fe^{3+} , low-spin Fe^{3+} would exist in the smaller octahedral site in post-perovskite, which is consistent with computational results [Li *et al.*, 2005a; Zhang and Oganov, 2006] and experimental results on Fe_2O_3 -PPv [Shim *et al.*, 2009]. Catalli *et al.* [2010b] found that Fe^{3+} in the bipolar prismatic site remains high-spin and Fe^{3+} in the octahedral site remains low-spin between 55 and 136 GPa. From the site weighting and the QS , our results on post-perovskite suggest that the spin state of Fe^{3+} (mixed spin) does not change across the post-perovskite transition.

Although Fe^{2+} exists only in the bipolar-prismatic site, Fe^{3+} exists in both the bipolar prismatic and octahedral sites. In addition, the spin state of Fe^{3+} (mixed spin) is likely different from that of Fe^{2+} in post-perovskite [Lin *et al.*, 2008; McCammon *et al.*, 2008]. These differences between Fe^{2+} -PPv and Fe^{3+} -PPv might be responsible for the contrast in the effects of Fe^{2+} and Fe^{3+} on the density of post-perovskite.

The notable difference between the Mössbauer parameters of the perovskite and post-perovskite phases is that the QS of the low-spin site is much smaller in post-perovskite

(Tab. 3.2). The smaller QS of the low-spin site in post-perovskite can be explained by a less distorted octahedral site, since distortion from a cubic environment around the Fe nucleus results in an increased QS value [Hawthorne, 1988]. The axial ratios (Figs 3-2b,c) of Fe^{3+} -PPv remain essentially the same as those of Fe^{2+} -PPv and Mg-endmember-PPv [Shim *et al.*, 2008; Guignot *et al.*, 2007]. These indicate that Fe^{3+} may decrease (or at least not change) the structural distortion, particularly related to the octahedra. This is in sharp contrast with the case of Fe^{3+} -Pv [Catalli *et al.*, 2010b] where Fe^{3+} significantly increases the distortion of the perovskite unit cell relative to both Fe^{2+} -Pv and pure Mg end member perovskite.

3.4 Discussion and geophysical implications

Our X-ray diffraction and synchrotron Mössbauer spectroscopy study shows that incorporation of Fe^{3+} does not change the volume of the post-perovskite phase, whereas Fe^{2+} increases the volume by 0.7%, suggesting that the valence state change in Fe may have significant effects on the density of mantle silicates at the lowermost mantle. Our SMS measurements indicate that Fe^{3+} enters post-perovskite through charge-coupled substitution and is in a mixed spin state, which is in contrast with the case of Fe^{2+} , where Fe^{2+} has been reported to be intermediate spin [McCammon *et al.*, 2008; Lin *et al.*, 2008] in the Mg site. Therefore, a change in the valence state of Fe would have notable effects on the physical properties of post-perovskite.

The greater density increase at the post-perovskite transition found in the Fe^{3+} -bearing system may have some implications for the stability of the chemical heterogeneities at the lowermost mantle. McCammon [1997] suggested that Fe^{3+} content may be enhanced by the presence of Al. Because the ionic sizes of Al and low-spin Fe^{3+} are essentially

3.4. Discussion and geophysical implications

the same [Shannon, 1976] and both can enter the octahedral site of Mg-silicates at the lowermost mantle [Li *et al.*, 2005a], Al would likely have a similar effect on volume as low-spin Fe³⁺. Basaltic material contains larger amounts of Fe and Al and therefore the density after the post-perovskite transition would be higher than the bulk lower mantle at the D'' layer. Therefore, basaltic material would be gravitationally stable at the D'' layer.

Table 3.1: Unit-cell volumes and lattice parameters of Fe³⁺-PPv at high pressure. Pressure was determined using the equation of state of gold [Tsuchiya, 2003].

P (GPa)	a (Å)	b (Å)	c (Å)	V (Å ³)
137.9 (16)	2.4460 (9)	7.971 (2)	6.068 (1)	118.30 (4)
137.4 (1)	2.4440 (6)	7.979 (2)	6.068 (2)	118.32 (4)
137.3 (27)	2.4446 (9)	7.977 (2)	6.069 (2)	118.36 (4)
136.2 (15)	2.4459 (9)	7.982 (2)	6.078 (1)	118.66 (4)
135.1 (13)	2.4470 (10)	7.986 (2)	6.071 (2)	118.64 (5)
135.0 (22)	2.4458 (6)	7.992 (1)	6.079 (1)	118.81 (3)
134.2 (3)	2.4463 (6)	7.994 (1)	6.083 (2)	118.96 (4)
134.2 (12)	2.4481 (9)	7.991 (2)	6.079 (2)	118.92 (4)
133.7 (10)	2.4474 (9)	7.998 (2)	6.081 (2)	119.03 (4)
132.4 (14)	2.4492 (6)	8.010 (2)	6.080 (1)	119.28 (4)
132.1 (22)	2.4476 (6)	8.014 (2)	6.088 (2)	119.43 (4)
132.1 (19)	2.4502 (6)	8.002 (2)	6.085 (1)	119.30 (4)
131.9 (16)	2.4468 (6)	8.001 (2)	6.084 (2)	119.12 (4)
131.4 (14)	2.4467 (7)	8.023 (2)	6.088 (1)	119.49 (4)
131.3 (17)	2.4493 (7)	8.007 (2)	6.083 (1)	119.29 (4)
130.7 (15)	2.4503 (9)	7.999 (2)	6.084 (2)	119.25 (4)

Table 3.2: Fitting results for the Mössbauer spectrum of Fe³⁺-PPv measured at 128 GPa. We obtained $\chi^2 = 1.3$ for the spectral fitting (QS : quadrupole splitting in mm/s, FWHM: distribution of QS in mm/s, and ΔIS : isomer shift difference between sites 1 and 2 in mm/s). For comparison, we also present the Mössbauer parameters of Fe³⁺-Pv [Catalli *et al.*, 2010b].

Phase	P (GPa)	Site 1			Site 2			ΔIS
		Weight	QS	FWHM	Weight	QS	FWHM	
PPv	127(7)	0.61(1)	1.99(1)	0.43(2)	0.39	0.318(9)	0.45(2)	0.40(1)
Pv	136(4)	0.59(1)	3.07(3)	0.24(1)	0.41	0.49(1)	0.313(4)	0.49(1)

Combined effect of ferric iron and aluminum on the properties of perovskite

This chapter is being prepared for publication as:

K. Catalli, S.-H. Shim, V.B. Prakapenka, J. Zhao, W. Sturhahn, P. Chow, Y. Xiao, H. Liu, H. Cynn, and W.J. Evans. Effects of the Fe^{3+} spin transition on the properties of aluminous perovskite and new insights for lower-mantle seismic heterogeneities.

Abstract

We have measured the effects of the coupled substitution of Fe^{3+} and Al on the density and compressibility of mantle silicate perovskite up to 95 GPa. X-ray emission spectroscopy and synchrotron Mössbauer spectroscopy reveal a rapid increase in the population of low-spin Fe^{3+} in Fe^{3+} ,Al-bearing perovskite over a narrow pressure range near 70 GPa, which is in sharp contrast with Al-free Fe^{3+} -Pv, where Fe^{3+} undergoes a gradual spin transition, and with Al-free Fe^{2+} -Pv, where Fe^{2+} does not become low spin. At low pressure, Fe^{3+} and Al expand the perovskite lattice. However, near the pressure range of the abrupt increase in the low-spin population, the unit-cell volume of Fe^{3+} ,Al-bearing perovskite becomes similar to that of Mg-endmember perovskite, while those of Al-free Fe^{3+} -bearing perovskite and Al-free Fe^{2+} -bearing perovskite remain larger throughout the lower mantle. Consequently, perovskite in Al-rich systems, should have lower density in the shallow lower mantle but similar or greater density than perovskite in pyrolite in the deep lower mantle, affecting the buoyancy and mechanical stability of heterogeneities. Although the Fe^{3+} spin transition in perovskite is unlikely to cause a seismic discontinuity at mantle

temperatures, it may result in a large change in bulk sound speed at 1200–1800 km depth, such that a vertically extending structure with an elevated amount of Fe^{3+} would generate slower and faster anomalies above and below the depth of the spin transition, respectively, relative to the surrounding mantle. This may have important implications for bulk sound speed anomalies observed at similar depths in seismic tomography studies.

4.1 Introduction

Spin transitions in iron have been reported in the major lower-mantle minerals, magnesium silicate perovskite and ferroperricline, at mantle pressures [Badro *et al.*, 2003, 2004; Li *et al.*, 2004; Lin *et al.*, 2005; Speziale *et al.*, 2005; Tsuchiya *et al.*, 2006; Fei *et al.*, 2007; McCammon *et al.*, 2008; Lin *et al.*, 2008; Umemoto *et al.*, 2008; Grocholski *et al.*, 2009]. The spin transition in ferroperricline, $(\text{Mg,Fe})\text{O}$, has been found to induce a volume collapse to that of the magnesium endmember (i.e., MgO), resulting in a density increase at lower-mantle pressures [Lin *et al.*, 2005; Speziale *et al.*, 2005; Fei *et al.*, 2007]. However, ferroperricline is expected to be a relatively minor component in the lower mantle while perovskite makes up approximately 80%; thus the properties of perovskite should significantly influence the bulk lower mantle.

Badro *et al.* [2004] reported a decrease in spin moment of iron in perovskite at high pressure. Recent studies proposed a high spin to intermediate spin transition in Fe^{2+} at high pressure [Lin *et al.*, 2008; McCammon *et al.*, 2008], while other experimental [Grocholski *et al.*, 2009] and computational [Zhang and Oganov, 2006; Stackhouse *et al.*, 2007; Bengtson *et al.*, 2008] studies have proposed that Fe^{2+} in perovskite remains high spin throughout most of the lower mantle. Regardless, Lundin *et al.* [2008] showed that Fe^{2+} does not affect the pressure–volume relationship in perovskite.

Mantle silicate perovskite is expected to contain 5–10% each of Fe and Al in the lower mantle [Kesson *et al.*, 1998]. Its crystal chemistry is complicated by the presence of two dif-

ferent crystallographic sites (dodecahedral, hereafter A, and octahedral, hereafter B, sites) available for cation substitution [Horiuchi *et al.*, 1987]. Iron may exist as both Fe^{2+} and Fe^{3+} with some studies finding up to 60% of iron to be Fe^{3+} in the presence of Al, even under reducing conditions [McCammon, 1997; Frost *et al.*, 2004]. Both theoretical [Stackhouse *et al.*, 2007; Hsu *et al.*, 2011] and experimental [Xu *et al.*, 2001; Catalli *et al.*, 2010b] studies demonstrated that Fe^{3+} in the B site of Al-free perovskite undergoes a high spin to low spin transition at much lower pressure than Fe^{2+} . The Mössbauer parameters and the spin transition of Fe^{3+} reported by Catalli *et al.* [2010b] have been reproduced and confirmed by a recent first-principles study [Hsu *et al.*, 2011].

The complex crystal chemistry of perovskite diversifies the environments for iron and complicates the interpretation of high pressure spectroscopy results, which have been inconsistent with one another [Badro *et al.*, 2004; Li *et al.*, 2004; Lin *et al.*, 2008; McCammon *et al.*, 2008; Grocholski *et al.*, 2009]. X-ray emission spectroscopy (XES) provides a measure of integrated spin population but does not distinguish iron in different valence states. Mössbauer spectroscopy is sensitive to both the valence and spin states of iron, but the interpretation of multiple iron sites in various states is difficult. The above issues can, therefore, be best resolved by measuring the effects of individual cations (Fe^{2+} , Fe^{3+} , and Al) on the properties of perovskite with a combination of different spectroscopic techniques.

We have systematically studied the effects of different cations on the pressure–volume relationship of perovskite, including pure magnesium endmember (Mg-Pv) [Lundin *et al.*, 2008], with 9 and 15 mol% FeSiO_3 (Fe^{2+} -Pv) [Lundin *et al.*, 2008], with 9 mol% Fe_2O_3 (Fe^{3+} -Pv) [Catalli *et al.*, 2010b], with 10 mol% Al_2O_3 (Al-Pv), and with 10 mol% FeAlO_3 (Fe^{3+} Al-Pv) (the latter two are reported here). All systems have been studied using the same pressure scale (gold) and pressure medium (argon) to allow for direct comparison between the different compositions. Therefore, these data sets provide important informa-

tion on the effects of compositional variation on the density ($d \ln \rho / dX$) and bulk sound speed ($d \ln V_{\phi} / dX$) of perovskite. Here we report synchrotron Mössbauer spectroscopy (SMS), XES, and X-ray diffraction (XRD) on Fe^{3+} -Al-Pv in the laser-heated diamond cell to 95 GPa to measure the spin state of Fe^{3+} and its effect on the pressure–volume relationship in aluminous perovskite. We discuss the effects of the Fe^{3+} spin transition in perovskite on lower mantle structure and dynamics.

4.2 Experimental procedure

Glass starting materials ($0.90\text{MgSiO}_3 \cdot 0.05\text{Al}_2\text{O}_3 \cdot 0.05\text{Fe}_2\text{O}_3$ and $0.90\text{MgSiO}_3 \cdot 0.10\text{Al}_2\text{O}_3$, numbers are in mol fraction) were synthesized by the containerless laser levitation method [Tangeman *et al.*, 2001]. For the Fe^{3+} -Al-Pv glass, synthesis was conducted under an O_2 atmosphere in order to prevent reduction during melting. By only allowing one valence state of iron (Fe^{3+}), the interpretation of SMS and XES data can be considerably simplified. Electron microprobe measurements revealed that the starting material is homogeneous and has a composition of $(\text{Mg}_{0.88}\text{Fe}_{0.13}\text{Al}_{0.11}\text{Si}_{0.88})\text{O}_3$ (± 0.01). The iron-bearing starting material is enriched with 95% ^{57}Fe for SMS.

The glass starting materials were ground to a powder and mixed with 10 wt% gold for use as an internal pressure standard [Tsuchiya, 2003] for the XRD studies. For SMS and XES, ruby grains were placed at the edge of the sample chamber for pressure determination [Mao *et al.*, 1986] instead of mixing with gold. For XRD and SMS, the sample powder was pressed to a foil and loaded into a preindented Re gasket. Argon was cryogenically loaded into the diamond cell, acting as both an insulating and a pressure medium, with a few spacer grains of sample material separating the sample foil from the diamond. For XES, 3 mm diameter Be gaskets with an initial central thickness of 100 μm were used. A sample

platelet was pre-pressed and sandwiched between 5 μm layers of dried NaCl and loaded into the gasket hole.

Symmetric-type diamond anvil cells equipped with 200 or 300 μm culet diamonds were used for measurements with a peak pressure of less than 75 GPa, while 100 or 150 μm beveled culets were used above this pressure. Measurements on $\text{Fe}^{3+}\text{Al-Pv}$ were taken from multiple sample loadings.

The perovskite phase was synthesized by double-sided laser heating at 2000 K for 30 min above 45 GPa using an Nd:YLF laser (Fig. A-1) [Prakapenka *et al.*, 2008]. In addition, at each pressure the sample was scanned with the laser at 1800–2100 K for 7–15 minutes to synthesize the stable structure at the new pressure and to anneal deviatoric stress.

Angle-dispersive XRD was performed at the GSECARS sector of the Advanced Photon Source (APS) (Fig. A-1). A monochromatic X-ray beam was focused to $5 \times 5 \mu\text{m}^2$ with energy of 40 keV for measurements on $\text{Fe}^{3+}\text{Al-Pv}$ and $10 \times 20 \mu\text{m}^2$ at 30 keV for Al-Pv. Diffraction was collected using a MarCCD detector for $\text{Fe}^{3+}\text{Al-Pv}$ and a Mar345 imaging plate for Al-Pv. Diffraction lines of argon in all diffraction patterns confirm the presence of the pressure/insulation medium. Both the hexagonal close-packed (hcp) and face-centered cubic structures are observed in some diffraction patterns (Fig. A-1), likely due to the inclusion of a small amount of nitrogen during cryogenic loading of Ar, which stabilizes the hcp phase [Wittlinger *et al.*, 1997; Catalli *et al.*, 2008].

SMS was performed at the HPCAT and XOR-3 sectors of the APS (Fig. 4-3). At XOR-3, the 14.4 keV beam was focused to an area of $6 \times 6 \mu\text{m}^2$. The storage ring was operated in top-up mode with 24 bunches separated by 153 ns. Nuclear resonant scattering was measured in a time window of 15–130 ns following excitation. Data collection typically took 2–4 hours [see Jackson *et al.*, 2005; Sturhahn and Jackson, 2007; Catalli *et al.*, 2010b,

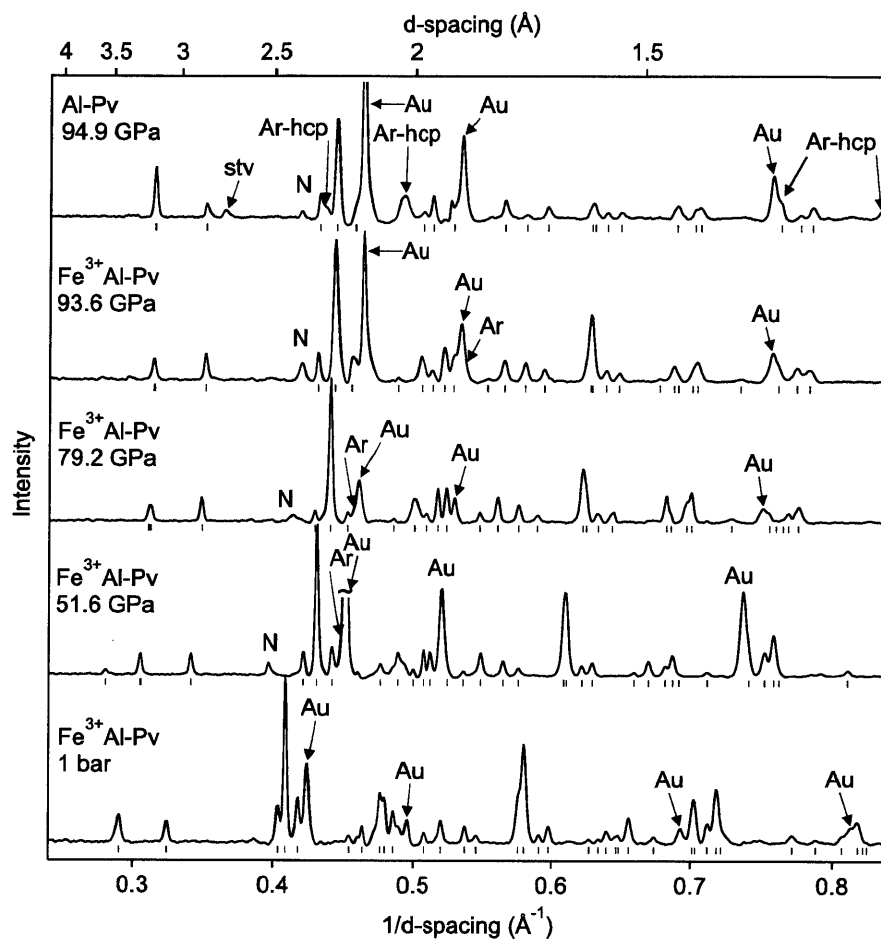


Figure 4-1: Representative X-ray diffraction patterns of Fe^{3+} Al-Pv (bottom four patterns) and Al-Pv (topmost pattern). The ticks below each diffraction pattern show the locations of perovskite lines used for the calculation of volume and lattice parameters. Au: gold; Ar: argon; Ar-hcp: hcp structured argon; stv: stishovite; N: nitrogen. Backgrounds have been subtracted.

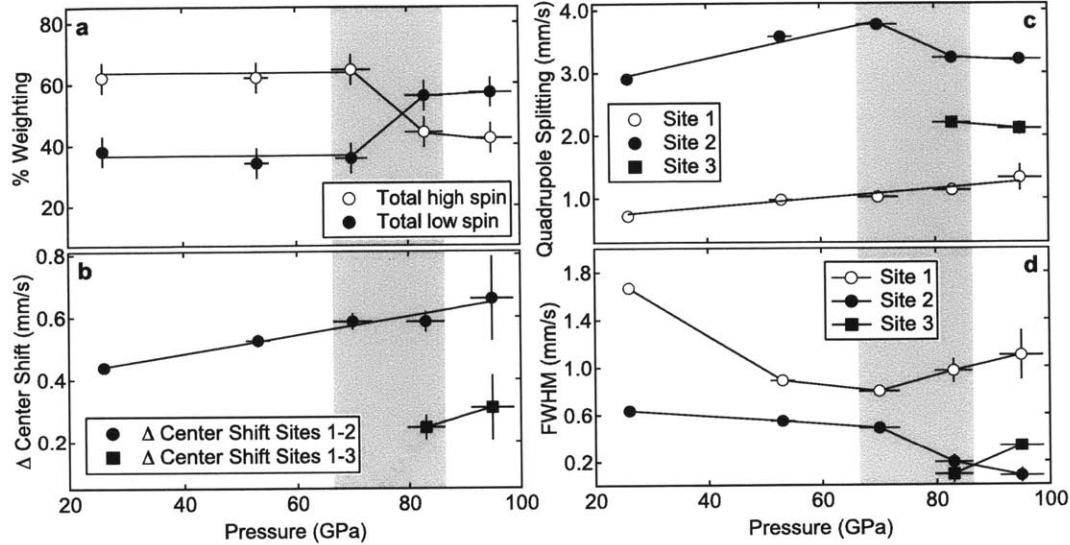


Figure 4-2: Mössbauer parameters of $\text{Fe}^{3+}\text{Al-Pv}$. Site 1: high-spin Fe^{3+} , site 2: low-spin Fe^{3+} , site 3: low-spin Fe^{3+} site that appears above 70 GPa. (a) Percent weightings of high (open circles) and low (closed circles) spin sites (site 2 + site 3), (b) relative center shift between sites 1 and 2 (circles) and between sites 1 and 3 (squares), (c) quadrupole splittings of high spin (open circles), low spin (closed circles), and new low spin (closed squares) sites, and (d) full widths at half maxima of quadrupole splittings (same symbols as (c)). The gray area is the pressure range where we found spectral changes in Fig. 4-3. Errors in parameters are outputs from CONUSS.

for details]. At beamline 16-IDD of HPCAT, the beam size was $30 \times 40 \mu\text{m}^2$ and data collection time was 8–10 hours. SMS data were fit using the CONUSS package [Sturhahn, 2000] (Fig. 4-2).

XES was performed at the HPCAT sector of APS (Fig. 4-4). An 11.35 keV X-ray beam was focused down to $30 \times 40 \mu\text{m}^2$ on the sample. Emission was collected through the Be gasket. Collection time was typically 8–16 hours. The spectra have been aligned relative to a reference spectrum (iron foil) according to their centers of mass and normalized by total area following the method of Vankó *et al.* [2006] (Figs 4-4 and 4-5). The method is discussed further in Catalli *et al.* [2010b].

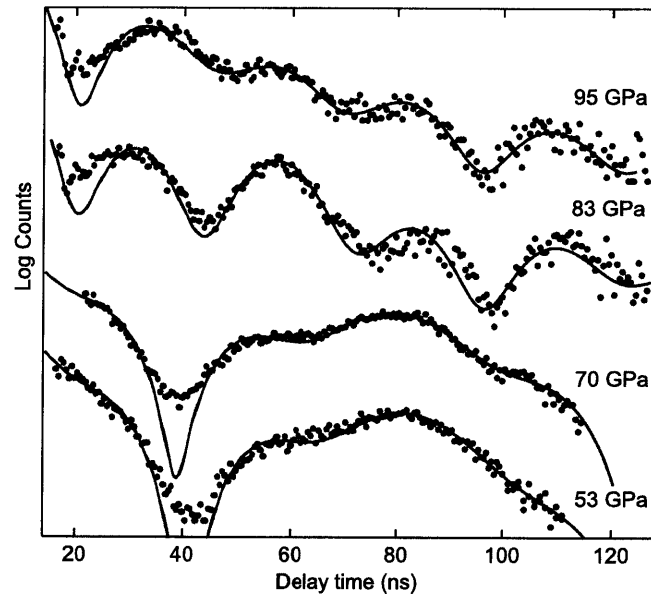


Figure 4-3: Synchrotron Mössbauer spectra of Fe^{3+} Al-Pv at high pressure. Data points are shown as dots, while the lines are the spectral fitting results. The Mössbauer parameters obtained from the fitting are shown in Fig. 4-2. Large gaps between the curve and the low-count data points at ~ 40 ns in low-pressure spectra are due to the logarithmic scale for the vertical axis. The misfit does not exceed 7% of the maximum counts, which is comparable for the magnitude of misfits in other spectral areas.

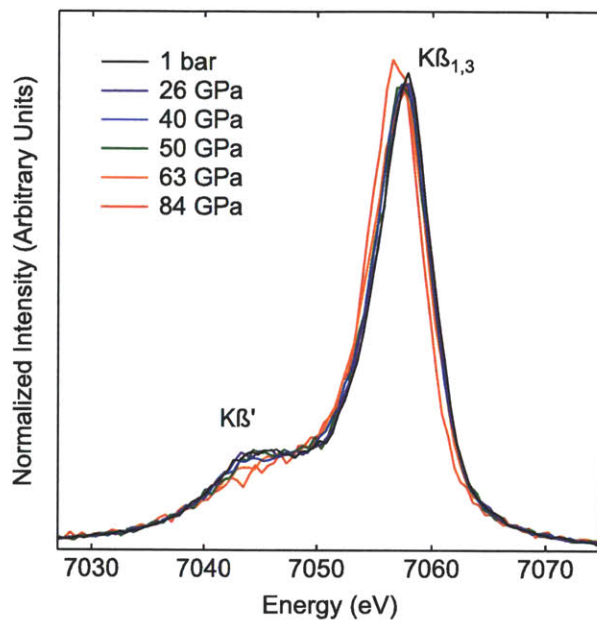


Figure 4-4: X-ray emission spectra of Fe^{3+} Al-Pv measured at high pressure. Spectra have been aligned according to their center of mass.

Diffraction patterns of Fe^{3+} Al-Pv were measured between 0 and 95 GPa (Fig. A-1, Table 4.1) and at 0–95 GPa on Al-Pv (Table 4.2). The patterns measured below 45 GPa were collected on decompression and not annealed in order to prevent back transformation to low pressure phases. Mössbauer spectra of Fe^{3+} Al-Pv were measured between 26 and 95 GPa (Fig. 4-3). The spectrum measured at 26 GPa was taken on decompression, and last laser-heated at 52 GPa. XES was measured between 0 and 84 GPa (Fig. 4-4). The emission spectra taken at 40 and 26 GPa and ambient pressure were made on decompression and last laser-heated at 50 GPa.

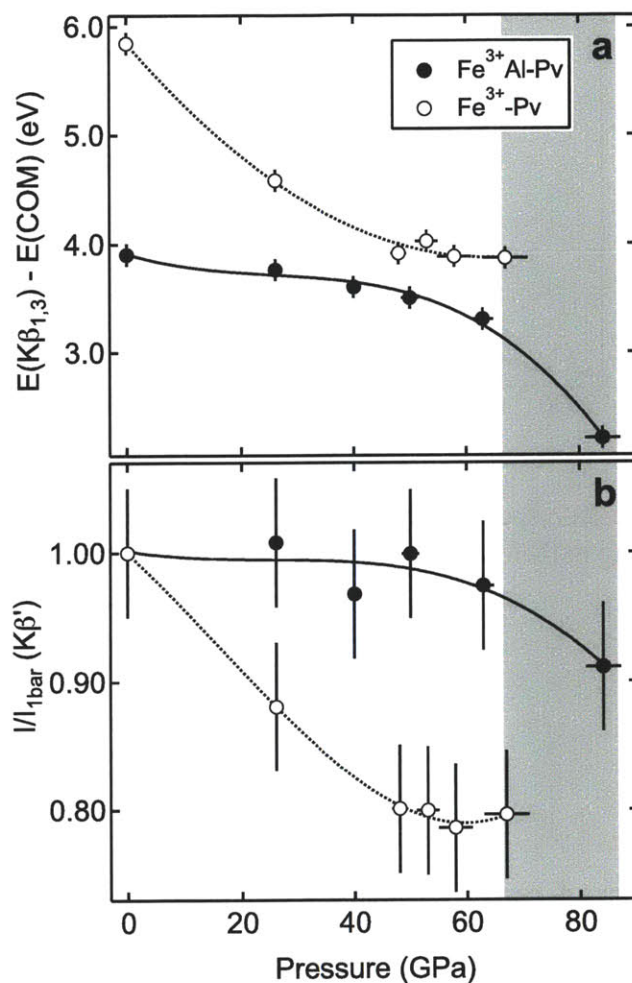


Figure 4-5: Parameters obtained from X-ray emission spectroscopy of $\text{Fe}^{3+}\text{Al-Pv}$. (a) Energy differences between the main peak position ($K\beta_{1,3}$) and the centers of mass. (b) The integrated intensity of the satellite peak ($K\beta'$) relative to the spectrum measured at 1 bar for the quenched sample. The gray area is the pressure range where we observed changes in SMS and XES.

4.3 Results

4.3.1 Effects of ferric iron and aluminum on the structure of perovskite

All observed diffraction lines can be explained by orthorhombic *Pbnm* perovskite (both Fe³⁺Al-Pv and Al-Pv) with gold (pressure scale), argon (pressure medium), and nitrogen (captured during cryogenic loading) (Fig. A-1). No diffraction lines from other phases, including SiO₂, Fe₂O₃, or Al₂O₃, are present in the patterns, suggesting that Fe³⁺ at least predominantly remains in the perovskite structure [see *Catalli et al.*, 2010b, for more detail]. The most intense line from silica (either in stishovite or the CaCl₂-type) was observed in some diffraction patterns of Al-Pv. Stishovite and CaCl₂-type silica can contain up to 5 wt% Al₂O₃ [*Hirose et al.*, 2005]. However, according to our diffraction patterns, the amount of stishovite should not exceed 5%. Therefore, the dominant amount of Al should exist in the Al-Pv phase.

Trivalent cations, such as Fe³⁺ and Al, enter into the perovskite structure through either oxygen vacancy substitution or charge coupled substitution [*Navrotsky*, 1999; *Brodholt*, 2000]. Charge coupled substitution becomes energetically more favorable at pressures related to the lower mantle [*Brodholt*, 2000]. We note perovskite was synthesized at pressures greater than 45 GPa in this study. In the case of Al-free Fe³⁺-Pv, *Catalli et al.* [2010b] showed that Mössbauer spectra measured at high pressure were consistent with charge coupled substitution of Fe³⁺ at pressures related to the lower mantle. Therefore, it is likely that Fe³⁺ and Al also enter the perovskite structure through charge coupled substitution under these conditions.

An ideal undistorted perovskite structure has cubic symmetry, while Mg-silicate perovskite crystallizes in the distorted orthorhombic *Pbnm* structure, with unit cell axial ratios of $a : b : c \simeq 1 : 1 : \sqrt{2}$. Therefore, the axial ratios, b/c (= 1 in a pseudo-cubic perovskite)

and c/a ($= \sqrt{2}$ in a pseudo-cubic perovskite), are a measure of the degree of distortion in the unit cell (Fig. 4-6). With pressure, all perovskites presented in Fig. 4-6 show increasing axial ratios, suggesting increasing distortion with pressure. Fe^{2+} reduces and Fe^{3+} alone increases the distortion of the perovskite unit cell relative to Mg-Pv throughout the lower mantle [Lundin *et al.*, 2008; Catalli *et al.*, 2010b]. The distortion in the unit cell of Al-Pv is greater than Mg-Pv at lower pressures but approaches that of Mg-Pv at high pressure.

Fe^{3+} Al-Pv is more distorted than Mg-Pv at lower pressures. However, the gap between Mg-Pv and Fe^{3+} Al-Pv decreases with pressure. Because the magnitude and high-pressure behavior of the axial ratios of Fe^{3+} Al-Pv are much more similar to Al-Pv than Fe^{3+} -Pv, Al is likely the more important contributor to the distortion of mantle perovskite than Fe^{3+} in this composition. These suggest that the degree of structural distortion in perovskite is sensitive to composition (Fig. 4-6).

4.3.2 Synchrotron Mössbauer spectroscopy

The synchrotron Mössbauer spectra of Fe^{3+} Al-Pv below 70 GPa consist of one broad feature with three overlapping beats (Fig. 4-3). Between 70 and 83 GPa, the spectra show drastic changes to four clearly separated beats. Similar spectral changes were also observed in Al-free Fe^{3+} -Pv but at a much lower pressure, 55 GPa [Catalli *et al.*, 2010b]. Qualitatively, it is clear from the spectra (Fig. 4-3) that there is a change in the iron environments occurring between 70 and 83 GPa. The spectra taken between 26 and 70 GPa were fit using a two iron site model, while the spectra at 83 and 95 GPa require three sites for a satisfactory fit to the data (Fig. 4-2).

Quadrupole splitting (QS) is a measure of the splitting of the excited nuclear state caused by an electric field gradient. The QS of iron in silicates and oxides is sensitive to both the valence and spin states of iron [Hawthorne, 1988]. To a lesser degree, it is

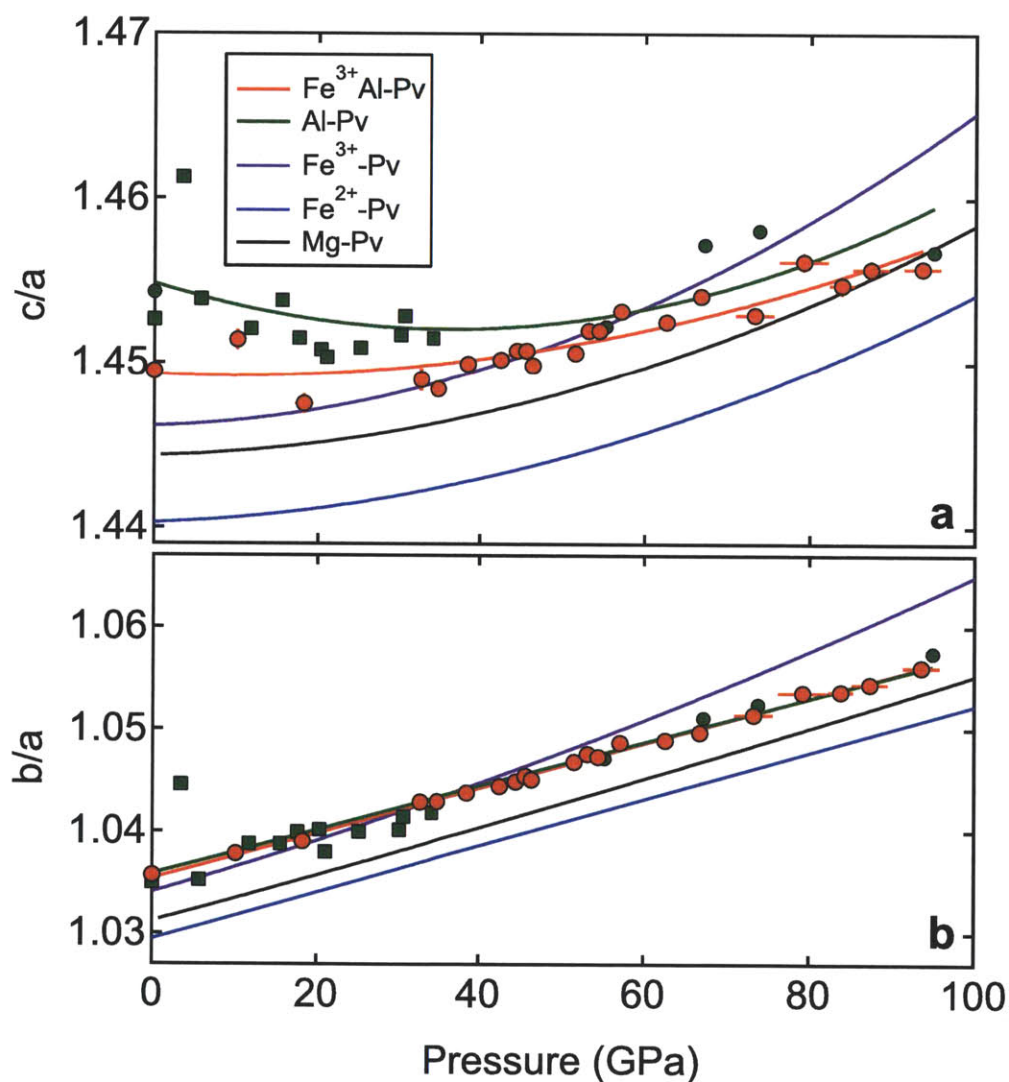


Figure 4-6: Axial ratios of perovskite, (a) b/a and (b) c/a , with different compositions. Red circles and lines: Fe^{3+} Al-Pv (this work), green: Al-Pv (green circles from this study and squares from *Yagi et al.* [2004]), purple: Fe^{3+} -Pv [*Catalli et al.*, 2010b], blue: Fe^{2+} -Pv [*Lundin et al.*, 2008], black: Mg-Pv [*Lundin et al.*, 2008]. Errors in axial ratios are based on the errors on individual axial parameters output from the UnitCell Program [*Holland and Redfern*, 1997] and in most cases are smaller than the marker size.

also sensitive to the coordination state of iron. In this study, we used starting materials containing all iron in Fe^{3+} and the dominant valence state of iron remains 3+ after laser heating (see below for details and also related discussions in *Catalli et al.* [2010b]). This allows us to attribute the changes in QS to the spin state of Fe^{3+} .

The number of regular quantum beats in a spectrum increases with the magnitude of the dominant QS component. Therefore, the drastic change in raw spectra seen above 70 GPa (Fig. 4-3) indicates an increase in the QS of the dominant Fe^{3+} site. Because the QS of Fe^{3+} increases at a high spin to low spin transition [*Li et al.*, 2006; *Bengtson et al.*, 2009; *Hsu et al.*, 2011], the changes observed in the raw spectra suggest an increase in the amount of low spin Fe^{3+} in perovskite.

At 70 GPa and below, the fitting identifies one iron site with $QS = 2.9 \sim 3.8$ mm/s and the other with $QS = 0.7 \sim 1.3$ mm/s (Fig. 4-2c). The lower QS value is consistent with high spin Fe^{3+} [*Xu et al.*, 2001; *Dyar et al.*, 2006], which we assign to the A site. A high QS value (~ 3.0 mm/s) was found experimentally for low spin Fe^{3+} in Al-free, Fe^{3+} -Pv [*Catalli et al.*, 2010b] in the B site, the interpretation of which was confirmed by computations [*Hsu et al.*, 2011]. Therefore, we assign the high QS site to low spin Fe^{3+} in the B site. The site weightings reveal that $\sim 35\%$ of the Fe^{3+} is low spin between 26 and 70 GPa in Fe^{3+} -Al-Pv (Fig. 4-2a).

The high QS value of low spin Fe^{3+} is similar to that of high spin Fe^{2+} [*Hsu et al.*, 2011]. However, the starting materials contain all iron in Fe^{3+} . Our XRD patterns show that the starting material transforms completely to perovskite without evidence for SiO_2 or MgO (Fig. A-1), ruling out the possibility of reduction of Fe^{3+} to Fe^{2+} during laser heating (see *Catalli et al.* [2010b]). Previous studies showed that Al can stabilize Fe^{3+} over Fe^{2+} in perovskite [*McCammon*, 1997; *Frost et al.*, 2004]. Furthermore, our SMS interpretation of low spin Fe^{3+} is consistent with our XES observation (see below).

The third site required for fitting the spectra at 83 and 95 GPa has a QS near 2.2 mm/s (Fig. 4-2c). For the rare-earth orthoferrite perovskites (LaFeO_3 and PrFeO_3), which have the same $Pbnm$ perovskite structure as well as Fe^{3+} in the octahedral site, $QS \simeq 2.4$ mm/s was observed for low spin Fe^{3+} in the B site [Xu *et al.*, 2001]. Therefore, the third iron site is also most likely low spin Fe^{3+} in the B site. Combining the two low spin sites gives a total low spin fraction of $56 \pm 5\%$ at 83–95 GPa, an increase from 35% at pressures below 70 GPa (Fig. 4-2a).

4.3.3 X-ray emission spectroscopy

The X-ray emission spectra of high spin iron are characterized by the main $K\beta_{1,3}$ peak at 7058 eV and the $K\beta'$ satellite peak at lower energy which results from the $3p$ core-hole $3d$ exchange interaction during emission (Fig. 4-4). The intensity of the satellite peak ($K\beta'$) has been found to be proportional to the spin number of iron in the sample [Badro *et al.*, 1999; Vankó *et al.*, 2006]. However, this requires an accurate standard for low spin Fe^{3+} . An orthorhombic phase of Fe_2O_3 measured at 46 GPa appears to have all iron in the low spin state [Badro *et al.*, 2002; Shim *et al.*, 2009]. However, the structure of this phase is more likely the Rh_2O_3 -II type [Shim and Duffy, 2002; Shim *et al.*, 2009] and therefore this phase may not be a good low spin standard for Fe^{3+} -Al-Pv. We are aware of no other phases that would make good low spin Fe^{3+} (or low spin Fe^{2+}) standards for perovskite and, therefore, believe it is much more appropriate to present relative changes in the integrated intensity of the satellite peak with respect to that of Fe^{3+} -Al-Pv quenched to ambient pressure. The relative changes in the average spin measured by XES can then be compared with the SMS results.

The position of the main peak ($K\beta_{1,3}$) has also been used to detect spin transitions [Vankó *et al.*, 2006; Li *et al.*, 2004]. Determination of the peak position involves much less

uncertainty and therefore provides a more robust measure of the spin transition. Following the method presented in *Vankó et al.* [2006], the position of $K\beta_{1,3}$ was obtained relative to the center of mass of the spectra (Fig. 4-5a, see *Catalli et al.* [2010b] for method). These allow for robust interpretations by focusing only on first-order features in the raw X-ray emission spectra, which are not sensitive to a specific standard or fitting methods.

For Fe^{3+} -Al-Pv, the relative position of $K\beta_{1,3}$ with respect to the center of mass of the spectrum is essentially unchanged up to 63 GPa (Fig. 4-4). Between 63 and 84 GPa, however, there is a large shift in the $K\beta_{1,3}$ peak (Fig. 4-5a). In addition, the integrated intensity of the satellite peak ($K\beta'$) decreases at the same pressure range (Fig. 4-5b). Decreases in these quantities are related to a decrease in average spin number [*Badro et al.*, 2003, 2004; *Li et al.*, 2004]. Therefore, our XES observations suggest an increase in the population of low spin Fe^{3+} between 63 and 84 GPa. As shown in Fig. 4-5, this behavior is in contrast with Al-free Fe^{3+} -Pv where a gradual decrease in spin moment was found at pressures between 0 and 55 GPa [*Catalli et al.*, 2010b].

As mentioned earlier, XES is much more sensitive to the spin state than the valence state [*Vankó et al.*, 2006]. For example, because the $K\beta_{1,3}$ peak position is essentially insensitive to the valence state within ± 0.3 eV [*Gamblin and Urch*, 2001] while it is much more sensitive to the spin state. Our XES measurements clearly indicate an increase in low spin Fe^{3+} at ~ 70 GPa and therefore we can rule out the interpretation of the new high QS site observed in SMS as being due to the creation of high spin Fe^{2+} .

4.3.4 Equation of state

A total of 20–32 diffraction lines were used to constrain the volume of Fe^{3+} -Al-Pv and 15–22 lines for Al-Pv using the UnitCell program [*Holland and Redfern*, 1997] (Fig. 4-7a). The volume of gold was measured based on 2–3 diffraction lines and used to calculate

pressure [Tsuchiya, 2003]. The uncertainty given is the standard deviation in pressure based on the volume of gold calculated from each individual diffraction line. In order to assess the effect of composition on the unit-cell volume of perovskite, we present the volume of each composition relative to Mg-Pv (Fig. 4-7b).

While a dense data distribution was achieved for Fe³⁺Al-Pv, because of the lack of low pressure data on Al-Pv, except for at 1 bar, we have included the results from a previous study by Yagi *et al.* [2004] on the same composition at 0–34 GPa, which is in good agreement with our results. Al expands the volume of perovskite at low pressures (Fig. 4-7). However, due to the higher compressibility of Al-Pv, its volume becomes essentially identical to Mg-Pv by ~50 GPa (Fig. 4-7). Fitting the combined Al-Pv dataset to the Birch-Murnaghan equation of state (EOS), we find that the incorporation of 10 mol% Al₂O₃ results in a ~7% decrease in bulk modulus relative to Mg-Pv [Lundin *et al.*, 2008], yielding $K_0 = 244 \pm 3$ GPa when K'_0 is fixed to 4 (where K_0 is the bulk modulus at 1 bar and K'_0 is its pressure derivative).

Fe³⁺Al-Pv has a larger volume than Mg-Pv, Al-Pv, and Fe²⁺-Pv but smaller volume than Fe³⁺-Pv at pressures lower than 55 GPa (Fig. 4-7b). This is consistent with the Al-Pv and Fe³⁺-Pv data, where Al and Fe³⁺ individually increase the unit cell volume of perovskite. Fe³⁺ and Al together (Fe³⁺Al-Pv) increase the compressibility of perovskite below 70 GPa (K_0 of 262 ± 8 GPa with $K'_0 = 3.0 \pm 0.3$ for fixed $V_0 = 164.807 \text{ \AA}^3$, where V_0 is volume at 1 bar), consistent with cases where either Al or Fe³⁺ alone exist in perovskite (Al-Pv and Fe³⁺-Pv).

Above 70 GPa, the unit cell volume of Fe³⁺Al-Pv becomes essentially the same as that of Mg-Pv, necessitating a change in compressibility (Fig. 4-7). We consider the region above 70 GPa to be a different regime, and fit it with a separate EOS. Because V_0 is unknown for this pressure range, it was allowed to vary in the EOS fitting. This yielded

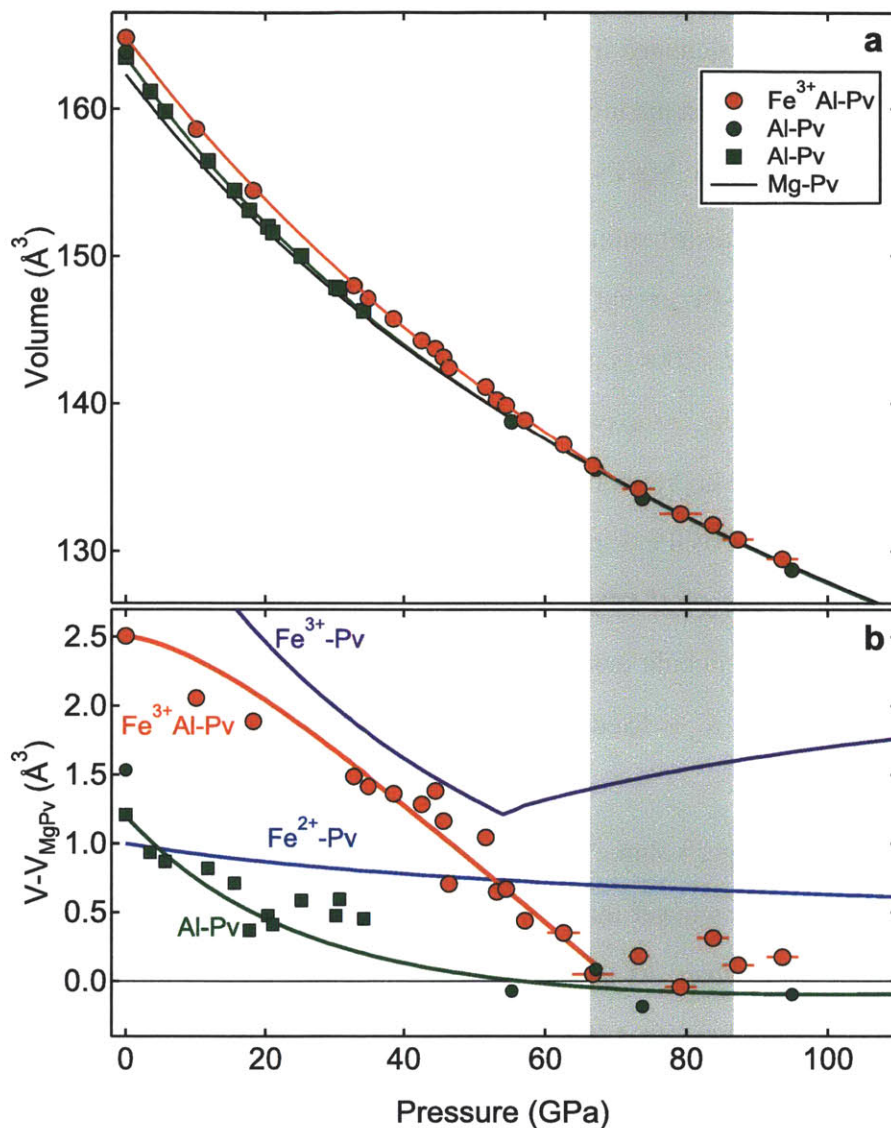


Figure 4-7: (a) Unit-cell volumes of Fe^{3+} Al-Pv (red circles) and Al-Pv (green circles from this study and squares from *Yagi et al.* [2004]). The red line is the fit to the third order Birch-Murnaghan equation for Fe^{3+} Al-Pv for data below 70 GPa and the green line is the EOS fit for Al-Pv. The equation of state of Mg-Pv [*Lundin et al.*, 2008] (black line) is shown for comparison. (b) Volume difference from Mg-endmember perovskite (red: Fe^{3+} Al-Pv, green: Al-Pv, blue: Fe^{2+} -Pv [*Lundin et al.*, 2008], purple: Fe^{3+} -Pv [*Catalli et al.*, 2010b]). The horizontal line represents the volume of Mg-Pv [*Lundin et al.*, 2008]. The gray areas show the pressure range where changes in the SMS and XES spectral features were detected.

$K_0 = 269 \pm 13$ GPa with $V_0 = 162 \pm 1 \text{ \AA}^3$ for a fixed K'_0 of 4. The EOS of the higher pressure range was constrained by only 6 data points over a pressure range of 28 GPa without constraint from a known V_0 and is, thus, less reliable. However, K_0 and V_0 match well with Mg-Pv [Lundin *et al.*, 2008] within the uncertainty. It is notable that the pressure where the volume of Fe^{3+} -Al-Pv merges into that of Mg-Pv coincides with the pressure range where changes in SMS and XES were detected.

A recent study on perovskite with 15 mol% $\text{Fe}^{3+}\text{AlO}_3$ [Nishio-Hamane *et al.*, 2008] did not find the volume collapse and change in compressibility as found here, although the study agrees with ours in that the combined substitution of Fe^{3+} and Al results in an increased compressibility. The difference in the results can be attributed to the greater data scatter and the lack of coverage in pressure below 40 GPa and between 70 and 90 GPa in Nishio-Hamane *et al.* [2008].

Unlike ferropericlase where a sharp decrease in volume over a narrow pressure range was observed at the spin transition [Fei *et al.*, 2007], we found no evidence of a sharp volume change in Fe^{3+} -Al-Pv at the spin transition in Fe^{3+} , within our experimental resolution. This difference is likely due to the much smaller amount of iron undergoing the spin transition (20%) in Fe^{3+} -Al-Pv than ferropericlase (100%). It is also notable that stress in perovskite is accommodated by both tilting of the octahedra and decreasing bond distances, while in ferropericlase it is mostly through decreasing bond distances. A negligible effect of the Fe^{3+} spin transition on volume was also found in a first-principles study on perovskite in a similar composition [Li *et al.*, 2005b].

Some computational studies have proposed a smaller change in the compressibility of perovskite by the spin transition of Fe^{3+} [Li *et al.*, 2005a; Caracas, 2010]. However, Li *et al.* [2005a] only considered the spin transition of Fe^{3+} in the A site. Caracas [2010] reported the elasticity of FeAlO_3 and AlFeO_3 where strong iron-iron interactions and mag-

netic ordering might influence the compressibility, while these are unlikely factors for our diluted system.

4.4 Implications for the crystal chemistry of perovskite

Computational studies have predicted that Fe^{3+} in the B site of perovskite would be low spin at high pressure [Li *et al.*, 2005a; Stackhouse *et al.*, 2007; Hsu *et al.*, 2011], and experimental studies showed that Fe^{3+} undergoes a high spin to low spin change in the B site of the *Pbnm* perovskite phases of LaFeO_3 and PrFeO_3 at 30–50 GPa [Xu *et al.*, 2001] and MgSiO_3 perovskite at 0–55 GPa [Catalli *et al.*, 2010b]. Therefore, it is reasonable to assign low spin Fe^{3+} to the B site.

For perovskite synthesized at 25 GPa and then quenched to 1 bar for XRD measurements, Vanpeteghem *et al.* [2006a] reported that all iron (including Fe^{3+}) remains in the A site while all Al exists in the B site. If we assume that Fe^{3+} and Al enter perovskite through charge coupled substitution, our data indicate that low spin Fe^{3+} can enter the B site and move an equal amount of Al into the A site at high pressure. The assumption of charge coupled substitution for our samples is reasonable because a first-principles study found that charge coupled substitution is energetically more favorable at high pressure [Brodholt, 2000] and our samples were synthesized at sufficiently high pressures, above 45 GPa.

Our data indicates that the population of low spin Fe^{3+} abruptly increases in Fe^{3+} -Al-Pv at 70 GPa. If all low spin Fe^{3+} , including the new iron site, enters the B site, the abrupt increase in low spin Fe^{3+} above 70 GPa would result in an abrupt increase in the amount of Al in the A site, i.e., site mixing of Fe and Al between the A and B sites in perovskite:



4.4. Implications for the crystal chemistry of perovskite

where superscripts “A” and “B” represent the A and B sites of perovskite, respectively, and superscripts “HS” and “LS” indicate high spin and low spin, respectively.

A computational study has shown that the energy difference between configurations with “Fe³⁺ in the A site + Al in the B site” and “Al in the A site + Fe³⁺ in the B site” in perovskite becomes negligibly small at 92 GPa [Li *et al.*, 2005a], supporting our interpretation of site mixing. In this case, the two different *QS* values for low spin Fe³⁺ in the B site may result from the coexistence of different local clusterings in perovskite, which may be energetically similar with each other [Stackhouse *et al.*, 2007; Bengtson *et al.*, 2009]. Alternatively, the new site could be assigned to low spin Fe³⁺ in the A site, while the B site remains predominantly occupied by Al. However, this would require a mixture of high spin and low spin Fe³⁺ in the A site, stable with no further increase in low spin component over a span of at least 15 GPa.

The former hypothesis may also provide some explanations why the spin transition is gradual in Al-free Fe³⁺-Pv and sharp in Fe³⁺ Al-Pv. While no inter-site diffusion is necessary for the Fe³⁺ spin transition in Al-free Fe³⁺-Pv, because Fe³⁺ exists in the B site from low pressures, inter-site diffusion would be critical for the Fe³⁺ spin transition in Al-bearing perovskite because Al would be dominant in the B site at low pressure and the B site is more favorable for the spin transition of Fe³⁺ [Hsu *et al.*, 2011]. This might also explain why the Fe³⁺ spin transition does not reach 100% in Fe³⁺ Al-Pv; it would require diffusion of all Al from the B to the A site, which would be energetically costly for the system.

In Al-free Fe³⁺-Pv, Catalli *et al.* [2010b] found a gradual high spin to low spin transition in Fe³⁺ in the B site (Fig. 4-5) that increases the compressibility of perovskite at low pressure. However, in this study, we found that the population of low spin Fe³⁺ does not change up to 70 GPa when Al is present in the system and, therefore, the higher com-

compressibility of Fe³⁺Al-Pv at 0–70 GPa (Fig. 4-7) should be the result of some other factor. Because Al increases the compressibility of perovskite as shown in Al-Pv (Fig. 4-7), Al is the more likely source of the higher compressibility of Fe³⁺Al-Pv at low pressure.

At ambient pressure, high spin Fe³⁺ is approximately 21% larger than Al, whereas low spin Fe³⁺ is comparable in size to Al [Shannon, 1976]. Therefore, in the highly compressed lattice of Al-bearing perovskite near 70 GPa (Fig. 4-7), where the unit cell volume of perovskite approaches to that of Mg endmember, the smaller-sized low spin Fe³⁺ would be energetically more favorable than high spin Fe³⁺. This means that Al plays an important role in the spin behavior of Fe³⁺ in mantle silicate perovskite.

4.5 Implications for the lower mantle

We have built a large dataset for understanding the effects of different cations on the compressional behavior of mantle silicate perovskite [Lundin *et al.*, 2008; Catalli *et al.*, 2010b] by using a consistent experimental setup, including pressure scale, pressure medium, and stress annealing. This allows for direct comparison among the different compositions without contamination from the use of different pressure scales or samples under different stress conditions, and therefore allows us to reliably extract compositional effects on density, bulk modulus, and bulk sound speed (Fig. 4-8).

The density of Fe³⁺Al-Pv was calculated using the unit cell volume data measured from XRD and the composition measured by electron microprobe of the starting material. For a more reasonable comparison, the iron content of each of the other compositions (Fe³⁺-Pv and Fe²⁺-Pv) was scaled to be equal to that of Fe³⁺Al-Pv (Fig. 4-8a,b). For Fe²⁺-Pv, we performed a linear interpolation of volume at ambient pressure based on iron content between 15 mol% Fe²⁺-Pv and pure Mg-Pv [Lundin *et al.*, 2008]. The compressibility of

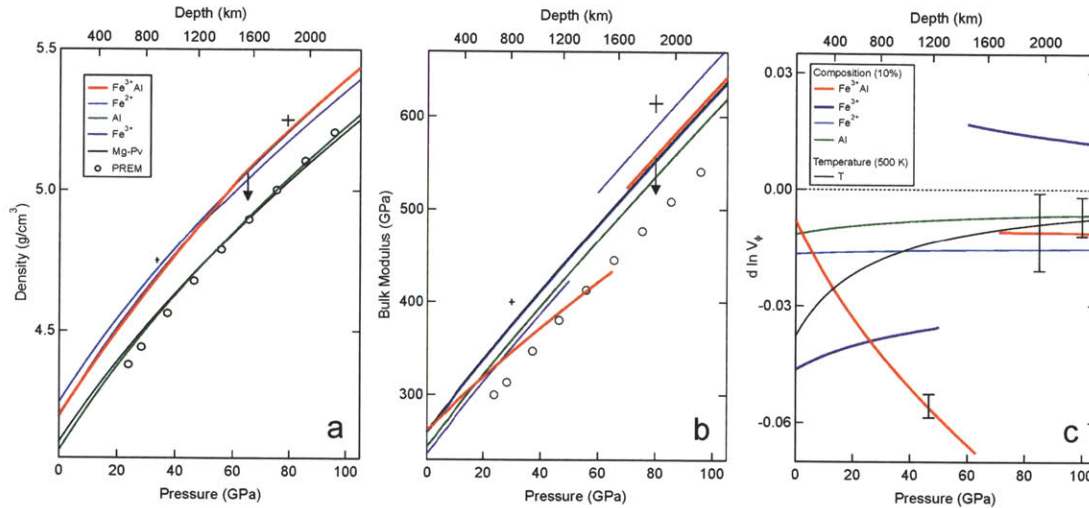


Figure 4-8: Profiles of (a) density, (b) bulk modulus, and (c) the effects of perovskite composition on bulk sound speed ($d \ln V_\phi / dX$) relative to Mg-Pv. For comparison, density and bulk modulus of the Preliminary Reference Earth Model (PREM) [Dziewonski and Anderson, 1981] are shown in (a) and (b) (black circles). In (a) and (b), the values for Fe²⁺-Pv [Lundin *et al.*, 2008] (blue lines) and Fe³⁺-Pv [Catalli *et al.*, 2010b] (purple lines) were scaled to 13% iron for comparison with Fe³⁺-Al-Pv (red lines) (see discussion for scaling details). Mg-Pv [Lundin *et al.*, 2008] (black lines) and Al-Pv (green lines) have not been scaled. The arrows show the expected effect of temperature on the density and bulk modulus of perovskite. In (c), the effect of increasing temperature by 500 K was calculated using the parameters in Fiquet *et al.* [2000] (black lines). The compositional effects were calculated for 10% changes in the content of different cations. Two sets of representative error bars, one for low pressure and one for high pressure, are shown as crosses above the density and bulk modulus lines in (a) and (b), respectively. In (c), errors are shown for Al-Pv and for the high and low pressure segments of Fe³⁺-Al-Pv.

perovskite was found to be essentially insensitive to Fe^{2+} content, so K_0 was set to 259 GPa for $K'_0 = 4$ [Lundin *et al.*, 2008]. Because Fe^{3+} -Pv has a more complicated pressure–volume behavior, volume was scaled to 6.5 mol% Fe_2O_3 by a linear interpolation between 9 mol% Fe_2O_3 -bearing perovskite [Catalli *et al.*, 2010b] and Mg-Pv [Lundin *et al.*, 2008] at each individual pressure. All of the perovskite data presented were measured at 300 K. The expected effect of temperature on the density measured in MgSiO_3 [Fiquet *et al.*, 2000] is shown by an arrow in Fig. 4-8a,b, and assumes that cation substitution up to 13% does not change the thermal properties of perovskite.

At pressures lower than 55 GPa, Fe^{2+} -Pv is the most dense composition, while Fe^{3+} -Pv and Fe^{3+} Al-Pv are less dense (1% at 1 bar) (Fig. 4-8a). The larger unit cell volumes of Fe^{3+} -Pv and Fe^{3+} Al-Pv are perhaps due to lattice expansion by Fe^{3+} and Al in the B site, because of their larger ionic sizes relative to Si. Near 60 GPa, Fe^{3+} Al-Pv becomes roughly the same density as Fe^{2+} -Pv (Fig. 4-8a). This is due to the fact that while Fe^{2+} -Pv has essentially the same bulk modulus as Mg-Pv, Fe^{3+} Al-Pv is more compressible, resulting in a much faster increase in density with pressure than either Fe^{2+} -Pv or Mg-Pv. Fe^{3+} Al-Pv and Fe^{3+} -Pv have similar densities up to ~ 55 GPa. At 55 GPa, the completion of the spin transition in Fe^{3+} -Pv results in the stiffening of the structure, which translates to a lower rate of increase in the density of the composition. However, the volume collapse in Fe^{3+} Al-Pv allows the density of this composition to rapidly increase with pressure.

We calculated the bulk moduli of perovskites with different compositions using the EOS fitting results (Fig. 4-8b). The bulk modulus of Fe^{2+} -Pv remains essentially the same as that of Mg-Pv [Lundin *et al.*, 2008], while Al decreases the bulk modulus by 3–4% throughout the lower mantle. In Fe^{3+} -Pv and Fe^{3+} Al-Pv, we found changes in bulk modulus at 55 and 70 GPa, respectively. Because we rely on the first-derivative of the EOS for the calculation of bulk modulus, our data are not of sufficiently high-resolution to distinguish between a

continuous or discontinuous increase in the bulk modulus [Catalli *et al.*, 2010b].

The rate of increase in bulk modulus is distinct in Fe³⁺Al-Pv compared with all other compositions. This is because we fit all of the other compositions using the second-order Birch-Murnaghan (B-M) equation ($K'_0 = 4$ fixed), while the EOS fit for Fe³⁺Al-Pv is made with the third-order B-M equation. When the third-order equation was used we did not find significant changes in K'_0 from 4 for all the compositions except for Fe³⁺Al-Pv. Statistically, the fitting quality for Fe³⁺Al-Pv data improves significantly from the second-order to third-order B-M equation, while it is not the case for the Fe³⁺-free compositions. This indicates that the lower rate of increase in bulk modulus in Fe³⁺Al-Pv is at least qualitatively robust. Due to the large uncertainty in the EOS fitting for high pressure segments of Fe³⁺-Pv ($P \geq 55$ GPa) and Fe³⁺Al-Pv ($P \geq 70$ GPa), the difference in the bulk modulus between Fe³⁺-Pv and Fe³⁺Al-Pv may be statistically less significant at these pressure ranges. Yet, it is qualitatively clear from the slope change in Fig. 4-7 that an increase in bulk modulus is required to explain our data.

Using the density and bulk modulus, we calculated the effect of composition on the bulk sound speed of perovskite ($d \ln V_\phi$) (Fig. 4-8c), which is important in the interpretation of seismic tomography of the lower mantle [e.g., Trampert *et al.*, 2004]. As shown in Fig. 4-8c, for Fe²⁺ and Al, $d \ln V_\phi$ remains nearly constant throughout the lower mantle. However, $d \ln V_\phi$ is much more negative for Fe³⁺-bearing systems at shallow lower mantle pressures. However, after the spin transition of Fe³⁺, $d \ln V_\phi$ becomes either indistinguishable from that of Fe²⁺ if Al exists in the system (Fe³⁺Al-Pv) or even positive if Al is absent (Fe³⁺-Pv). The uncertainty in $d \ln V_\phi$ is larger for Fe³⁺ after its spin transition than those for other compositions and those for Fe³⁺ before the spin transition, mainly due to the unknown V_0 for the high-pressure segments of the P - V datasets of Fe³⁺-Pv and Fe³⁺Al-Pv. However, it is clear from Fig. 4-7 that the Fe³⁺ and Fe³⁺+Al cases require large increases in bulk

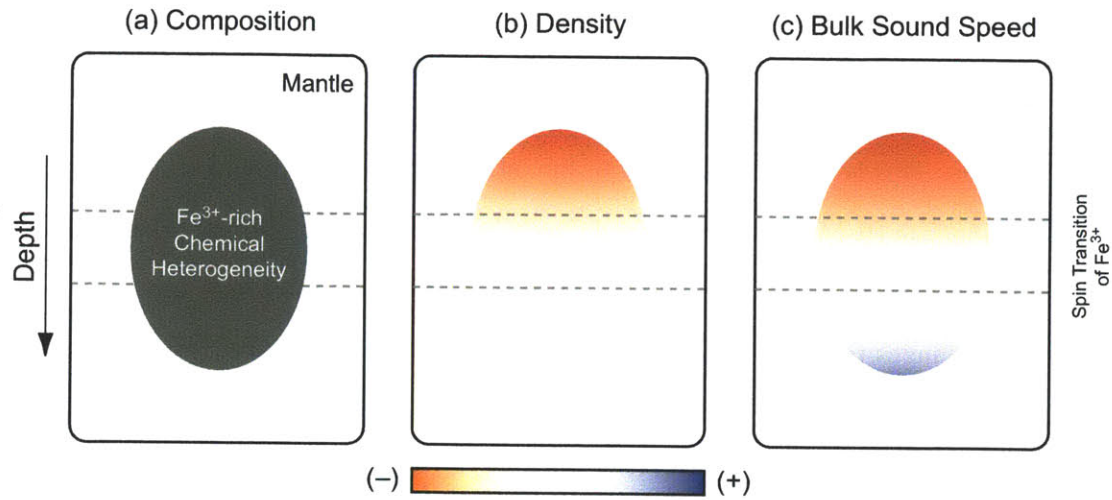


Figure 4-9: (a) A vertically extending mantle structure with an elevated amount of Fe^{3+} . In (b) and (c), we show the expected anomalies in density and bulk sound speed, respectively, with respect to normal mantle as a function of depth. Based on our results, an Fe^{3+} -rich structure would show a negative anomaly above the transition depth and either no anomaly or a slightly positive one below the depth of the Fe^{3+} spin transition.

modulus (and therefore $d \ln V_\phi$) across the spin transition.

The property changes associated with the Fe^{3+} spin transition may have important implications for the stability of chemical heterogeneities and the interpretation of seismic tomography of the lower mantle. For demonstration, in Fig. 4-9 we assumed a structure in the lower mantle with an elevated $\text{Fe}^{3+}/\Sigma\text{Fe}$ while the total iron content remains constant. We assume a structure extending across the depth of the Fe^{3+} spin transition with no temperature difference between the surrounding mantle and the structure.

Sturhahn et al. [2005] proposed that high temperature in the mantle would broaden the pressure interval over which spin transitions occur in the mantle. Therefore, in the lower mantle, the spin transition in Fe^{3+} is unlikely to result in a seismic velocity discontinuity. Instead, it would be a broad boundary as indicated by the two dashed lines in Fig. 4-9.

As shown in Fig. 4-8a, due to lattice expansion by the incorporation of Fe^{3+} , the Fe^{3+} -

rich structure in Fig. 4-9 would have a lower density than the surrounding mantle before the spin transition. However, due to the high compressibility, particularly for Fe^{3+} -Al-Pv, the density of an Fe^{3+} -rich vertical structure with a sufficient amount of Al may become comparable or even slightly greater than that of the surrounding mantle (Fig. 4-9). Therefore, an Fe^{3+} -rich structure may be positively and negatively buoyant before and after the spin transition, respectively, which would decrease the mechanical integrity of the structure in the mid-mantle.

As demonstrated in Fig. 4-9c, based on our results, Fe^{3+} -rich structures would have distinctively low bulk sound speeds in the shallow lower mantle before the spin transition of Fe^{3+} . However, the Fe^{3+} spin transition would make the bulk sound speed of the structure similar to (Fe^{3+} -Al-Pv) or slightly higher (Fe^{3+} -Pv) than that of the surrounding mantle. The change in $d \ln V_\phi$ by the spin transition may have important implications for the interpretation of bulk sound speed tomography of the lower mantle. For example, an Fe^{3+} -rich structure would be imaged as a negative anomaly at shallower depths, while it would be imaged as a positive anomaly at deeper depths (Fig. 4-9c).

Trampert et al. [2004] showed that the distribution of bulk sound speed anomalies in the lower mantle changes between 1200 and 2000 km depth. This depth range is similar to the depth expected for the spin transition of Fe^{3+} in perovskite. If indeed the spin transition contributes to the seismic change, chemical layering in the middle to lowermost regions of the lower mantle may not be required to explain the seismic changes and the spin transition might be an interesting candidate for the origin of the seismic observation. It is notable that perovskite in basalt (15 mol% Al_2O_3 and likely 10 mol% Fe_2O_3) contains more Al and therefore likely more Fe^{3+} than perovskite in pyrolite (5 mol% Al_2O_3 and likely 3 mol% Fe_2O_3) [*Hirose et al.*, 2005], considering the observation that Al elevates the concentration of Fe^{3+} in perovskite to $\text{Fe}^{3+}/\Sigma \text{Fe} = 0.6$ [*McCammon*, 1997]. Therefore, our calculation

(6.5 mol% Fe₂O₃) would be more applicable for basaltic systems.

For further implications for the lower mantle, it is important to investigate the thermal effects. In ferropericlase, it has been found that the high spin to low spin transition occurs over a much wider pressure range at high temperature [Sturhahn *et al.*, 2005; Lin *et al.*, 2007; Fei *et al.*, 2007]. Because Al-Fe³⁺ mixing between two different sites is likely involved in the high spin to low spin transition in perovskite, the mixing entropy can influence the broadness of the spin transition together with temperature. Also, temperature may increase the depth at which the high spin to low spin transition occurs [Sturhahn *et al.*, 2005]. It is also important to understand the effects of the Fe³⁺ spin transition on shear-wave speed in perovskite.

4.6 Conclusions

Our synchrotron X-ray spectroscopy measurements reveal that the presence of aluminum increases the pressure of the high spin to low spin transition in ferric iron and decreases the pressure interval over which the transition occurs. Furthermore, the unit cell volume of ferric aluminous perovskite merges to that of magnesium endmember perovskite at 70 GPa, while the unit cell volume of aluminum-free ferric perovskite remains greater than that of magnesium endmember throughout the lower mantle, resulting in distinct density profiles for mantle silicate perovskites depending on aluminum content. Our study reveals that the spin transition in ferric iron is strongly influenced by aluminum and increases the bulk modulus of perovskite. The bulk sound speed calculated from our measured density and bulk modulus shows that the spin transition in ferric iron would generate different seismic velocity anomalies in Fe³⁺-rich structures extending across the spin transition depth.

Table 4.1: Unit-cell volumes and lattice parameters of Fe³⁺Al-Pv at high pressure. Pressure was determined using the equation of state of gold [Tsuchiya, 2003].

P (GPa)	V (Å ³)	a (Å)	b (Å)	c (Å)
1 bar	164.81(4)	4.788(1)	4.959(1)	6.940(2)
10.1(8)	158.63(5)	4.722(1)	4.901(1)	6.854(2)
18.3(11)	154.46(6)	4.683(1)	4.866(1)	6.779(2)
32.7(8)	148.02(4)	4.610(1)	4.807(1)	6.680(1)
34.9(4)	147.14(4)	4.601(1)	4.798(1)	6.664(1)
38.6(5)	145.76(4)	4.584(1)	4.784(1)	6.646(1)
42.5(9)	144.30(4)	4.567(1)	4.770(1)	6.623(2)
44.5(6)	143.74(4)	4.560(1)	4.765(1)	6.616(1)
45.6(7)	143.16(4)	4.553(1)	4.760(1)	6.606(1)
46.4(9)	142.44(4)	4.547(1)	4.752(1)	6.592(2)
51.6(1)	141.13(4)	4.530(1)	4.742(1)	6.571(2)
53.2(8)	140.25(4)	4.518(1)	4.733(1)	6.560(2)
54.5(4)	139.88(4)	4.514(1)	4.728(1)	6.554(2)
57.1(7)	138.86(4)	4.500(1)	4.719(1)	6.539(1)
62.6(6)	137.22(4)	4.482(1)	4.702(1)	6.511(2)
66.8(6)	135.78(4)	4.464(1)	4.686(1)	6.491(2)
73.3(23)	134.22(4)	4.446(1)	4.674(1)	6.459(2)
79.2(29)	132.53(4)	4.421(1)	4.657(1)	6.437(2)
83.8(15)	131.80(4)	4.414(1)	4.651(1)	6.421(1)
87.3(22)	130.80(4)	4.400(1)	4.640(1)	6.406(1)
93.6(22)	129.47(4)	4.383(1)	4.629(1)	6.381(1)

Table 4.2: Unit-cell volumes and lattice parameters of Al-Pv at high pressure. Pressure was determined using the equation of state of gold [Tsuchiya, 2003].

P (GPa)	V (\AA^3)	a (\AA)	b (\AA)	c (\AA)
1 bar	163.83(5)	4.7740(12)	4.943(1)	6.943(2)
55.3(6)	138.78(4)	4.5022(9)	4.714(1)	6.538(1)
67.2(3)	135.56(3)	4.4565(9)	4.684(1)	6.494(1)
73.8(8)	133.58(4)	4.4319(10)	4.664(2)	6.462(2)
94.9(7)	128.75(4)	4.3722(10)	4.623(1)	6.370(1)

Thickness and Clapeyron slope of the post-perovskite boundary

K. Catalli, S.-H. Shim, and V.B. Prakapenka (2009). Thickness and Clapeyron slope of the post-perovskite boundary. Nature, 462, 782-785.

Abstract

The thicknesses and Clapeyron slopes of mantle phase boundaries strongly influence the seismic detectability of the boundaries and convection in the mantle. An unusually large positive slope found for the perovskite to post-perovskite boundary [Oganov and Ono, 2004; Tsuchiya *et al.*, 2004; Tateno *et al.*, 2009] would destabilize high-temperature anomalies at the lowermost mantle [Nakagawa and Tackley, 2004], which is incompatible with seismic observations [Garnero *et al.*, 2007]. Here we report the thickness and Clapeyron slope of the post-perovskite boundary in three compositions determined in the laser-heated diamond-anvil cell at in situ high pressure–temperature conditions up to 3000 K and 145 GPa. The measured Clapeyron slope ($+6.7 \pm 0.5$ MPa/K) is consistent with the D'' discontinuity [Sidorin *et al.*, 1999]. However, in both systems the boundary thickness in Fe²⁺ or Al bearing systems increases to $400 \sim 600 \pm 100$ km, which is substantially larger than the thickness of the D'' discontinuity (<30 km) [Lay, 2008]. Although the Fe²⁺ buffering effect of ferropericlasite may decrease the post-perovskite boundary thickness in an Al-free system, the post-perovskite boundary would remain thick in a pyrolitic composition because of the effects of Al and the rapid temperature increase in the D'' layer. The post-perovskite

boundary will be particularly thick in regions with elevated Al content and/or low Mg/Si ratio (such as basaltic materials), reducing the effects of the large positive Clapeyron slope of the post-perovskite boundary on the buoyancy of thermal anomalies and stabilizing the compositional heterogeneities at the lowermost mantle. If the post-perovskite transition is the source of the D'' discontinuity, regions with sharp discontinuities require distinct compositions, such as a higher Mg/Si ratio or low Al content.

5.1 Introduction

The bottom 200–400 km of the mantle, the D'' layer, has been known to have seismic properties distinct from the overlying mantle, including large-scale lateral variations in velocities and a laterally varying discontinuity at the top of the layer (i.e., D'' discontinuity) [Lay *et al.*, 1998; Garnero, 2000]. The discovery of a phase transition in the dominant mantle silicate (i.e., post-perovskite transition) [Murakami *et al.*, 2004; Oganov and Ono, 2004; Shim *et al.*, 2004] has provided new opportunities to better understand seismologic observations [Tsuchiya *et al.*, 2004; Wookey *et al.*, 2005] and to constrain important geophysical parameters [Lay *et al.*, 2006; van der Hilst *et al.*, 2007] in the D'' layer.

Any transition in phases with variable compositions should have a finite depth interval where both low- and high-pressure phases exist (hereafter boundary thickness). For seismic detection, the boundary thickness should be sufficiently small. A thickness less than 30 km was estimated for the D'' discontinuity [Lay, 2008]. In addition, together with its Clapeyron slope (dP/dT), the thickness of the post-perovskite (PPv) boundary is critical for understanding mantle convection in the D'' region [Nakagawa and Tackley, 2004].

The thickness of the post-perovskite boundary has not been well determined [Mao *et al.*, 2004; Hirose *et al.*, 2006; Tateno *et al.*, 2005; Nishio-Hamane *et al.*, 2007] due to experimental difficulties. Here we report determination of the thickness and Clapeyron slope of the post-perovskite boundary in $(\text{Mg}_{0.91}\text{Fe}_{0.09}^{2+})\text{SiO}_3$, $(\text{Mg}_{0.91}\text{Fe}_{0.09}^{3+})(\text{Fe}_{0.09}^{3+}\text{Si}_{0.91})\text{O}_3$ and

$(\text{Mg}_{0.9}\text{Fe}_{0.1}^{3+})(\text{Al}_{0.1}\text{Si}_{0.9})\text{O}_3$ at in situ high pressure–temperature in the double-sided laser-heated diamond anvil cell combined with synchrotron X-ray diffraction under improved experimental conditions.

5.2 Methods

The starting materials were a natural pyroxene with a composition of $(\text{Mg}_{0.91}\text{Fe}_{0.09}^{2+})\text{SiO}_3$ and synthetic glasses with compositions of $(\text{Mg}_{0.91}\text{Fe}_{0.09}^{3+})(\text{Fe}_{0.09}^{3+}\text{Si}_{0.91})\text{O}_3$ and $(\text{Mg}_{0.9}\text{Fe}_{0.1}^{3+})(\text{Al}_{0.1}\text{Si}_{0.9})\text{O}_3$. The pyroxene sample was also used in our recent X-ray diffraction study of the equation of state and crystal structure of post-perovskite [Shim *et al.*, 2008] and the Fe^{3+} – Fe^{3+} sample was used for the study of the equations of state of Fe^{3+} perovskite and Fe^{3+} post-perovvskite and the spin state of Fe^{3+} in perovskite and post-perovskite [Catalli *et al.*, 2010b, a]. The glass starting materials were synthesized from $\text{MgSiO}_3 + \text{Fe}_2\text{O}_3 \pm \text{Al}_2\text{O}_3$ oxide mixtures by the containerless method under an O_2 atmosphere in order to ensure that all Fe remained Fe^{3+} [Tangeman *et al.*, 2001]. The purity of the glass starting materials were examined by synchrotron X-ray diffraction and Raman spectroscopy. The valence state of Fe in perovskites (Pv) synthesized from the glasses was confirmed to be 3+ by synchrotron Mössbauer spectroscopy.

The starting material was powdered and mixed with 8–10 wt% gold for use as an internal pressure scale. A thin platelet of the sample + gold mixture (thickness less than 5 μm) was loaded in either a 35 or 50 μm hole of a pre-indented Re gasket. Ar was cryogenically loaded for pressure medium and insulation. The platelet is supported by grains with the same composition as the starting material, in order to prevent the platelet from being in direct contact with the thermally conductive diamond anvils. Diamond anvils with either a 75 or 100- μm diameter culet were mounted in symmetric-type diamond-anvil cells to

compress the samples to high pressure.

In situ high pressure–temperature measurements were conducted in the laser-heated diamond-anvil cell at the GSECARS sector of the Advanced Photon Source (APS) using a double-sided laser heating and angle dispersive diffraction setup. A monochromatic X-ray beam (energy of either 37 or 40 keV) was focused to $5 \times 5 \mu\text{m}^2$ on the sample and co-axially aligned with two Nd:YLF laser beams focused on both sides of the sample in the diamond-anvil cell. The size of the laser beam focus ($20 \mu\text{m}$) was comparable to the size of the sample ($20\text{--}30 \mu\text{m}$). Diffraction images were measured using the MarCCD detector. The tilt of the CCD detector and the sample-to-detector distance were calibrated by measuring the diffraction images of CeO_2 . The 2D diffraction images were integrated into diffraction patterns using the Fit2D software [Hammersley, 1997]. The unit-cell volume of gold, constrained by 2–5 diffraction lines, was used for calculating pressure combined with its equation of state [Tsuchiya, 2003]. The temperature of the sample was estimated by fitting the thermal radiation from the sample to Planck’s equation [Jeanloz and Heinz, 1984]. The measured diffraction patterns of perovskite and post-perovskite agree well with those calculated from the crystal structure models of these phases. In particular, the Rietveld refinements of the post-perovskite diffraction patterns [Shim *et al.*, 2008] yielded structural parameters which are in excellent agreement with computational predictions [Oganov and Ono, 2004; Tsuchiya *et al.*, 2004].

Controlling the thickness of the insulation layers is challenging in cryogenic Ar loading. Some samples show much broader diffraction lines even at high temperature, suggesting thin or no insulation layers. These data were not included in our boundary determination. Some of the previous boundary studies did not use an insulating medium.

We note that all three data sets, $(\text{Mg}_{0.91}\text{Fe}_{0.09})\text{SiO}_3$, $(\text{Mg}_{0.9}\text{Fe}_{0.1}^{3+})(\text{Al}_{0.1}\text{Si}_{0.9})\text{O}_3$, and $(\text{Mg}_{0.91}\text{Fe}_{0.09}^{3+})(\text{Fe}_{0.09}^{3+}\text{Si}_{0.91})\text{O}_3$, were measured using the same experimental methods, in-

cluding the pressure scale and pressure transmitting medium. This enables us to measure the thickness and transition pressure in a manner that is internally consistent among the different compositions.

5.3 Results

5.3.1 Ferrous post-perovskite

After being compressed directly to 120 GPa without heating, an amorphized $(\text{Mg}_{0.91}\text{Fe}_{0.09}^{2+})\text{SiO}_3$ pyroxene sample was heated for a total of 1.5 hrs at 1500–2700 K. Due to the thermal effect, pressure increased to greater than 130 GPa. At these conditions, the synthesis of a perovskite + post-perovskite (Pv+PPv) mixture was observed and the phase assemblage remained stable throughout the heating (Fig. 5-1a). In the next heating run at slightly higher pressure, the sample transformed completely to pure post-perovskite (Fig. 5-1b). A separate sample was heated to 2000–3000 K at 137 GPa where we observed synthesis of pure post-perovskite within 10 min. These observations indicate that the pressure–temperature conditions of the former sample are very close to the Pv+PPv→PPv boundary and those of the latter sample are within the stability field of pure post-perovskite.

When the pure post-perovskite sample was decompressed by 5 GPa and heated, perovskite diffraction lines appeared in 1 hr (Fig. 5-1c), indicating a PPv→Pv+PPv transition. We further decompressed this sample and heating it to 2800 K at 119 GPa revealed strong growth of perovskite diffraction lines. In the other samples compressed to 110–120 GPa, stability of the Pv+PPv mixture was observed over 1.5 hrs of heating. When the Pv+PPv mixture was decompressed and heated to 2000 K at 107 GPa, sudden broadening of the post-perovskite lines was observed within 10 min, indicating the instability of

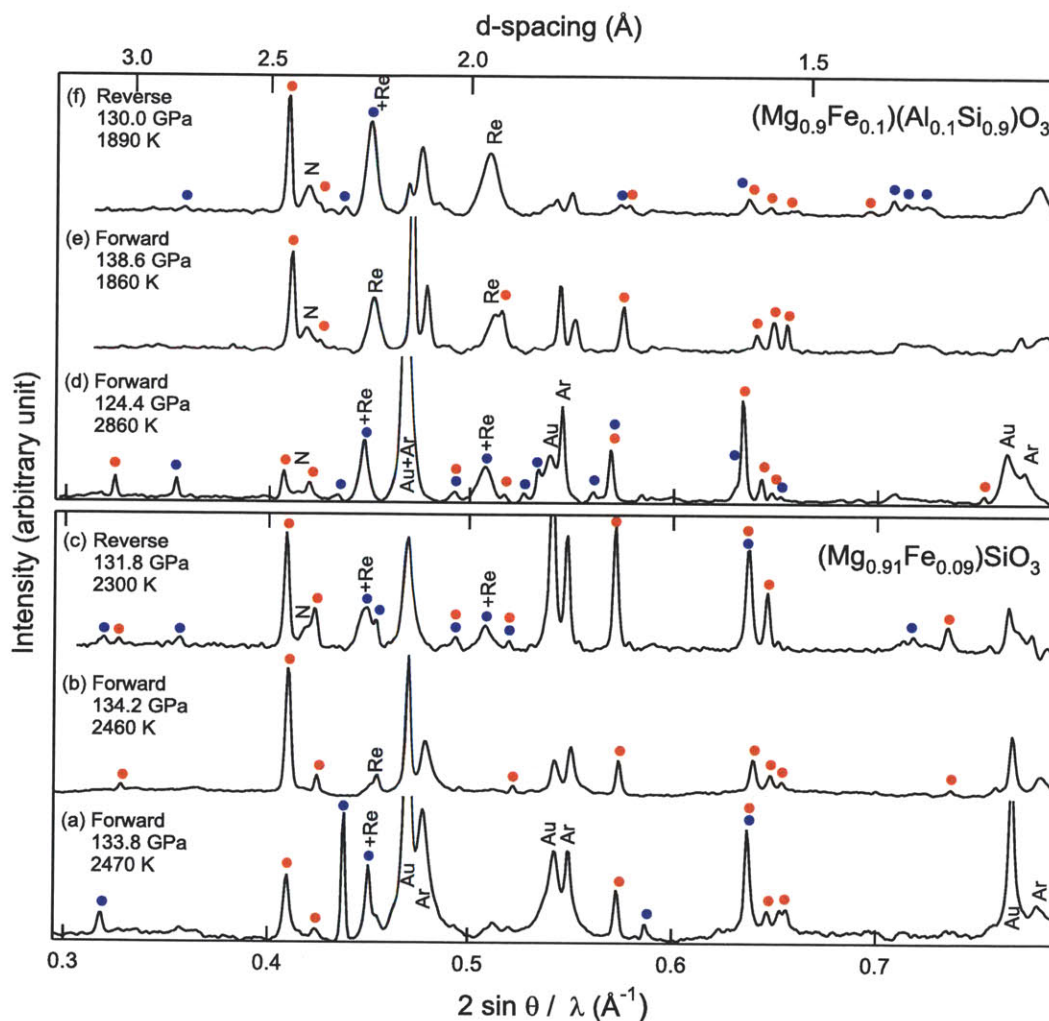


Figure 5-1: X-ray diffraction patterns of (a) Pv+PPv, (b) pure post-perovskite, and (c) PPv+Pv in $(\text{Mg}_{0.91}\text{Fe}_{0.09})\text{SiO}_3$, and (d) Pv+PPv, (e) pure post-perovskite, and (f) PPv+Pv in $(\text{Mg}_{0.9}\text{Fe}_{0.1}^{3+})(\text{Al}_{0.1}\text{Si}_{0.9})\text{O}_3$ measured at high pressure–temperature. Identifications for the major diffraction lines are shown (blue circles: perovskite, red circles: post-perovskite, Ar: pressure medium, Au: pressure standard, Re: gasket, N: nitrogen). Backgrounds were subtracted.

post-perovskite. This condition coincides with the Pv→PPv boundary reported previously [Hirose *et al.*, 2006] using the same pressure scale (Fig. 5-2a).

5.3.2 Ferric-aluminous post-perovskite

An amorphous $(\text{Mg}_{0.9}\text{Fe}_{0.1}^{3+})(\text{Al}_{0.1}\text{Si}_{0.9})\text{O}_3$ sample was compressed to 132 GPa where we observed synthesis of a Pv+PPv mixture during heating. After a total of 55 min of heating above 139 GPa, we observed a transition from a Pv+PPv mixture to pure post-perovskite (Fig. 5-1e), which indicates the stability of the post-perovskite phase. The pure post-perovskite sample was decompressed and heated to 1800–2100 K at 130 GPa. After a 13 min heating a few diagnostic diffraction lines of the perovskite phase appeared, indicating a PPv→Pv+PPv transition (Fig. 5-1f). For separate samples, the stability of a Pv+PPv mixture was observed up to 137 GPa at high temperature during compression. Therefore, the Pv+PPv→PPv boundary should exist between 130 and 140 GPa at 2000 K.

In other samples compressed to lower pressures, we observed the stability of a Pv+PPv mixture along both the forward and reverse directions between 113 and 137 GPa at 2000–3000 K (Fig. 5-1d). In a sample compressed to lower pressure, synthesis of pure perovskite was observed up to 109 GPa at 2000 K. These observations indicate that the boundary thickness is larger in $(\text{Mg}_{0.9}\text{Fe}_{0.1}^{3+})(\text{Al}_{0.1}\text{Si}_{0.9})\text{O}_3$ (Fig. 5-2b).

5.3.3 Ferric post-perovskite

The $(\text{Mg},\text{Fe}^{3+})(\text{Fe}^{3+},\text{Si})\text{O}_3$ glass sample was compressed to ~ 104 GPa and then laser-heated for 30 minutes. At 1500–2800 K and pressures of 112–115 GPa, ferric iron bearing orthorhombic perovskite was synthesized. There was no evidence for post-perovskite in the diffraction patterns, or any breakdown products of perovskite such as SiO_2 or Fe_2O_3 .

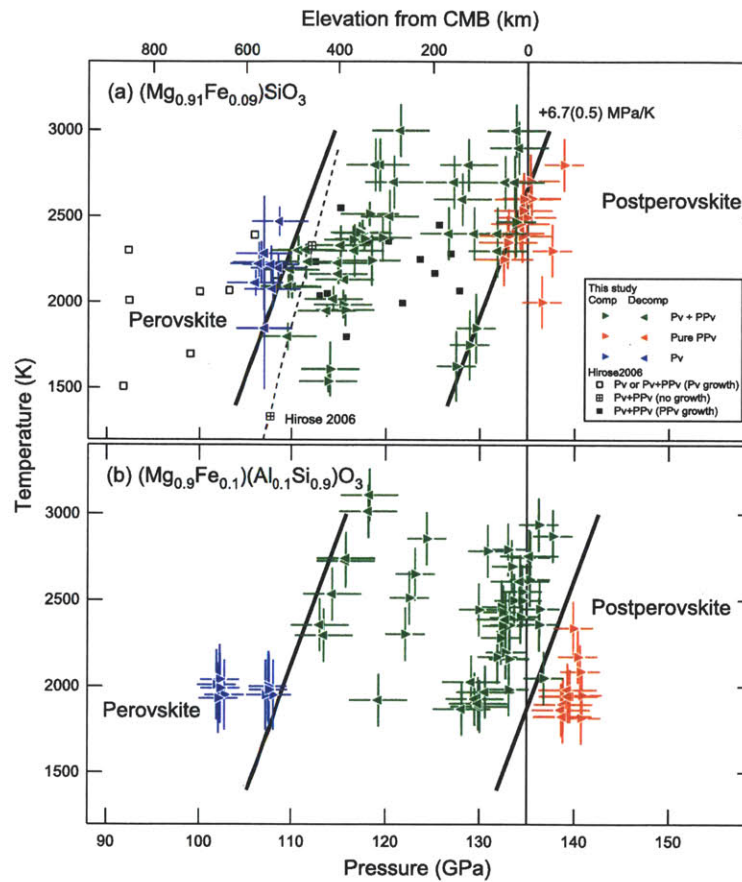


Figure 5-2: The pressure–temperature conditions for the stability of perovskite (blue triangles), Pv+PPv mixture (green triangles), and post-perovskite (red triangles) in (a) $(\text{Mg}_{0.91}\text{Fe}_{0.09})\text{SiO}_3$ and (b) $(\text{Mg}_{0.9}\text{Fe}_{0.1})(\text{Al}_{0.1}\text{Si}_{0.9})\text{O}_3$. The right and left triangles represent data points measured along the forward and reverse paths, respectively. The solid black lines are the phase boundaries determined from our data. The dashed line and squares in (a) are from a previous study [Hirose et al., 2006]. The error bars represent 1σ uncertainties. The elevations from the core-mantle boundary (CMB) is shown at the top.

Pressure was then increased to 118 GPa and further heated at 1500-2900 K, 122-128 GPa at high temperature. Within the first 10 minutes of laser-heating, post-perovskite started to crystallize in the diamond-cell at the expense of the ferric perovskite. A mixture of Pv+PPv was stable through the 30 minutes of heating under these conditions.

In a separate sample loading, the $(\text{Mg,Fe}^{3+})(\text{Fe}^{3+},\text{Si})\text{O}_3$ glass was compressed directly to 135 GPa without laser-heating. The sample was then heated for 1.5 hours at 1500-2500 K (139-145 GPa at high temperature). Initially the sample crystallized a mixture of Pv+PPv but continued heating convert all perovskite to post-perovskite and a pure post-perovskite sample was synthesized. This sample was then decompressed and heated at 1800-2600 K for 30 minutes three times, at 125-133 GPa at high-temperature, and pure post-perovskite was found to remain stable at these conditions. Upon decompressing to 111 GPa and heating to 1600-2600 K at 114-121 GPa, perovskite began to crystallize in the first couple minutes of heating.

5.4 Discussion

As shown in Fig. 5-3, Fe^{3+} increases the thickness but to much smaller degree compared to Fe^{2+} and $\text{Fe}^{3+}+\text{Al}$. We note that this sample contains a factor of two more Fe than the other two compositions. When it is normalized for 9 mol% Fe^{3+} for comparison with our data presented in the article, the post-perovskite boundary thickness is 70 ± 100 km. Considering the uncertainties, this means that the post-perovskite boundary remains essentially sharp with Fe^{3+} . This demonstrates that our method of constraining the boundary along both forward and reverse transitional paths is capable of detecting a sharp boundary. In addition, a recent study [Tateno *et al.*, 2009] using the same method also detected a sharp post-perovskite boundary in MgSiO_3 .

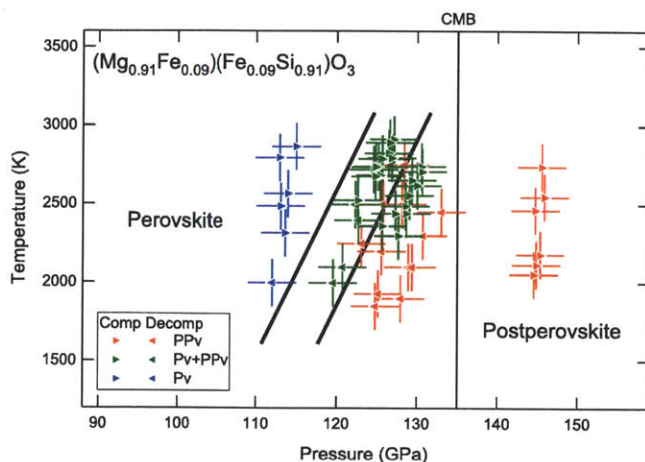


Figure 5-3: Pressure–temperature conditions for the stability of perovskite (blue triangles), Pv+PPv mixture (green triangles), and post-perovskite (red triangles) in $(\text{Mg}_{0.91}\text{Fe}_{0.09}^{3+})(\text{Fe}_{0.09}^{3+}\text{Si}_{0.91})\text{O}_3$. The right and left triangles represent data points measured along the forward and reverse paths, respectively. The solid lines are the phase boundaries determined from our data.

The phase boundary in this system is located at 110–120 GPa and 2500 K. Considering that the post-perovskite transition pressure in MgSiO_3 has been reported to be between 120 and 135 GPa [Murakami *et al.*, 2004; Ono and Oganov, 2005; Hirose *et al.*, 2006; Tateno *et al.*, 2009], our result suggests that Fe^{3+} lowers the post-perovskite transition pressure, which is consistent with a computational study [Ono and Oganov, 2005]. The post-perovskite transition is also found in Fe_2O_3 [Ono *et al.*, 2004; Shim *et al.*, 2008] which is the Fe^{3+} end member of the MgSiO_3 – Fe_2O_3 binary system. In Fe_2O_3 , the post-perovskite transition occurs at much lower pressures, 60–80 GPa [Ono *et al.*, 2004; Shim *et al.*, 2008].

Based on the relatively narrow Pv+PPv mixed phase region in $(\text{Mg}_{0.91}\text{Fe}_{0.09}^{3+})(\text{Fe}_{0.09}^{3+}\text{Si}_{0.91})\text{O}_3$ (Fig. 5-3), Fe^{3+} does not significantly increase the post-perovskite boundary thickness while it decreases the post-perovskite transition pressure significantly. Therefore, the large thickness increase observed in $(\text{Mg}_{0.9}\text{Fe}_{0.1}^{3+})(\text{Al}_{0.1}\text{Si}_{0.9})\text{O}_3$ should be primarily due to Al.

The much denser data coverage in $(\text{Mg}_{0.91}\text{Fe}_{0.09})\text{SiO}_3$ tightly constrains the Clapeyron slope of the $\text{Pv}+\text{PPv}\rightarrow\text{PPv}$ boundary, $+6.7\pm 0.5$ MPa/K, which is in agreement with the seismologic estimation for the D'' discontinuity [Sidorin *et al.*, 1999] and an earlier computational prediction [Tsuchiya *et al.*, 2004]. A larger magnitude Clapeyron slope ($+13.3\pm 1.0$ MPa/K) was reported in MgSiO_3 endmember [Tateno *et al.*, 2009]. However, the pressure scale they used (MgO) is known to yield about a factor of two larger Clapeyron slope compared with the gold scale used here [Hirose *et al.*, 2006] and therefore the discrepancy is largely due to the inconsistency among different pressure scales. However, differences in pressure can be more reliably determined and therefore the measured thickness should be less affected by this issue.

Our data reveal that both 9 mol% Fe^{2+} and 10 mol% $\text{Fe}^{3+}+10$ mol% Al substantially increase the thickness of the post-perovskite boundary to 20 ± 5 GPa (400 ± 100 km) and 30 ± 5 GPa (600 ± 100 km), respectively, which is much greater than the upper bound for the thickness of the D'' discontinuity, 30 km [Lay, 2008]. Some uncertainty sources should be considered. Kinetic effects normally delay a phase transition, resulting in an overestimation in transition pressure along the forward path (low- \rightarrow high-pressure phases) and an underestimation along the reverse path (high- \rightarrow low-pressure phases). In our study, there is a 2–5 GPa mismatch in the $\text{Pv}+\text{PPv} \leftrightarrow \text{PPv}$ boundary between the forward and reverse paths (Fig. 5-2) and therefore the boundary was placed at the mean of these bounds. Because the kinetic effects are opposite along these paths, measurement of the post-perovskite boundary along both transition paths reduces errors from these effects.

Heating to sufficiently high temperature is important for reducing kinetic effects. However, most previous post-perovskite studies heated the samples to less than 2000 K and only a few data points exist at higher temperature [Tateno *et al.*, 2009]. In our study, about half of the heating runs were made between 2500 and 3000 K. Sufficient heating duration is

also important. Although each heating run is limited to 15–50 min in order to prevent overheating of the diamond cell, we repeated heating at a given pressure for a total of 1–2 hrs of heating, whereas heating in many previous studies was limited to 3–30 min. With severe temperature gradients in laser heating, the colder spots suffer more from kinetic effects. In this study, in order to improve homogeneity in the heated spot, we used Ar as an insulation medium and the sample size was similar to that of the heating spot.

Our large boundary thicknesses in $(\text{Mg}_{0.91}\text{Fe}_{0.09}^{2+})\text{SiO}_3$ and $(\text{Mg}_{0.9}\text{Fe}_{0.1}^{3+})(\text{Al}_{0.1}\text{Si}_{0.9})\text{O}_3$ are consistent with earlier estimations for similar compositions [Mao *et al.*, 2004; Tateno *et al.*, 2005; Nishio-Hamane *et al.*, 2007] except for an in-situ study [Hirose *et al.*, 2006] which proposed a negligible post-perovskite boundary thickness in $(\text{Mg,Fe})\text{SiO}_3$. However, these studies did not perform measurements along both transitional paths and the data coverage is sparse. The earlier in-situ study [Hirose *et al.*, 2006] is based on diffraction intensity changes which can also be affected by recrystallization and preferred orientation during heating. They did not observe a complete transformation to pure post-perovskite up to their maximum pressure (122 GPa) but located their boundary at lower pressure based on diffraction intensity changes.

5.5 Geophysical implications

For the seismic detectability of the post-perovskite transition, it is important to consider: (1) the effects of the partitioning of elements among different phases, (2) the shape of the post-perovskite phase fraction profile in the mixed phase region, and (3) the effects of the rapid temperature increase in the D'' layer. In order to investigate the effects of these factors, we calculated the post-perovskite fraction profiles using the ideal solution model [Stixrude, 1997] combined with our thickness measurements and recent element partitioning studies

[Kobayashi *et al.*, 2005; Ono and Oganov, 2005; Auzende *et al.*, 2008; Sinmyo *et al.*, 2008] (Fig. 5-4). Because some discrepancy exists in the measured partition coefficients, we considered all the available data and chose upper bounds for the nonlinear deviations in the post-perovskite phase fraction profile and the Fe buffering effect of ferropericlaase for presentation in Fig. 5-4 [Catalli *et al.*, 2009, supplementary information, SI].

Existing partitioning studies are in agreement that Fe^{2+} content follows ferropericlaase > post-perovskite > perovskite when these phases coexist [Mao *et al.*, 2004; Kobayashi *et al.*, 2005; Ono and Oganov, 2005; Auzende *et al.*, 2008; Sinmyo *et al.*, 2008], and that Fe decreases the post-perovskite transition pressure [Mao *et al.*, 2004; Ono and Oganov, 2005] (See Appendix). As shown in our calculation along the 2500-K isotherm, these factors make the post-perovskite fraction profile nonlinear (dashed line in Fig. 5-4d) in a way that the rate of increase of the post-perovskite phase fraction is high near the bottom of the mixed phase region.

For the measured Fe partition coefficients [Kobayashi *et al.*, 2005; Auzende *et al.*, 2008; Sinmyo *et al.*, 2008], our calculation indicates that Fe buffering by ferropericlaase can reduce the post-perovskite boundary thickness to 80–130 km in $(\text{Mg}_{0.91}\text{Fe}_{0.09})\text{SiO}_3$ with 30% ferropericlaase, which is still larger than the thickness of the D'' discontinuity (<30 km) [Lay, 2008]. In order to match the seismic observation, the ferropericlaase content needs to be substantially higher than the 30% expected for a pyrolitic composition (Fig. 5-4d).

The buffering effect of ferropericlaase also increases the $\text{Pv} \rightarrow \text{Pv} + \text{PPv}$ transition depth, while it has very little effect on the $\text{Pv} + \text{PPv} \rightarrow \text{PPv}$ boundary (Fig. 5-4d). Because the ferropericlaase content increases with an increase in the Mg/Si ratio, this result suggests that the depth of the post-perovskite transition in $(\text{Mg}, \text{Fe}^{2+})\text{SiO}_3$ increases with an increase in the Mg/Si ratio. As shown in Fig. 5-4a, the deepening may result in no intersection between the post-perovskite boundary and the steep geotherm in the D'' layer, and therefore the post-

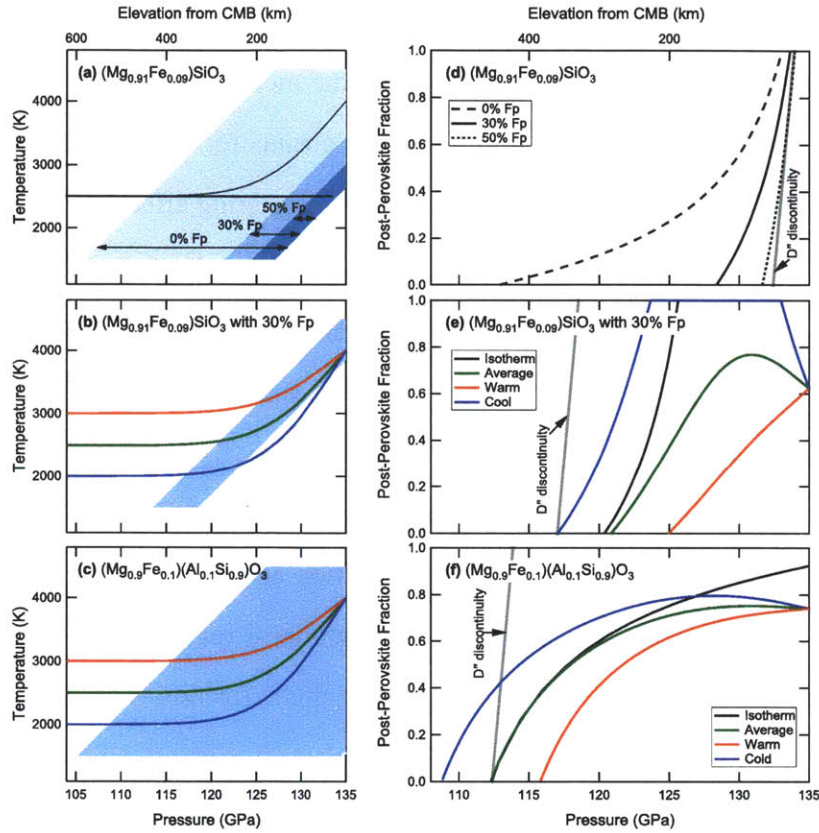


Figure 5-4: The Pv+PPv mixed phase region (blue shaded area) with the mantle geotherms (a-c) and the post-perovskite phase fraction profiles in the mixed phase region (d-f). (a and d) The Fe buffering effect of ferropiclsite on the post-perovskite boundary thickness in $(\text{Mg}_{0.91}\text{Fe}_{0.09})\text{SiO}_3$. Three different cases with different ferropiclsite contents are shown, i.e., 0%, 30%, and 50% ferropiclsite (mixed phase region in (a) with light, medium, and dark blue areas, respectively; the post-perovskite phase fraction profiles along a 2500-K isotherm in (d) with dashed, solid, and dotted lines, respectively). The thick horizontal line is a 2500-K isotherm and the thin curve is a mantle geotherm. (b and e) The post-perovskite boundary thickness and the post-perovskite phase fraction profiles along the mantle geotherms in $(\text{Mg}_{0.91}\text{Fe}_{0.09})\text{SiO}_3$ with 30% ferropiclsite. The boundary is shifted by -8 GPa to generate the maximum overlap between the post-perovskite boundary and the mantle geotherm (see text for detail). (c and f) The post-perovskite boundary thickness and the post-perovskite phase fraction profiles along the mantle geotherms in $(\text{Mg}_{0.9}\text{Fe}_{0.1}^{3+})(\text{Al}_{0.1}\text{Si}_{0.9})\text{O}_3$. The black lines in (e) and (f) are the post-perovskite phase fraction profiles along a 2500-K isotherm. The gray line represents a hypothetical linear post-perovskite phase fraction profile with a thickness consistent with the upper bound of the D'' discontinuity thickness [Lay, 2008]. The mantle geotherms at the lowermost mantle are calculated using the error function combined with temperature estimation for the region [van der Hilst et al., 2007].

perovskite transition may not exist in regions with a pyrolitic Mg/Si ratio.

Because the absolute pressure scale is uncertain (± 5 GPa) over 100 GPa, we do not rule out the possibility of an overlap between the thinned post-perovskite boundary in $(\text{Mg,Fe}^{2+})\text{SiO}_3$ and the geotherm. In Fig. 5-4b, we intentionally shifted the post-perovskite boundary by -8 GPa to produce the maximum overlap. Because of comparable magnitudes between the Clapeyron slope of the post-perovskite boundary and the rate of temperature increase in the D'' layer, the post-perovskite phase fractions along the mantle geotherms do not increase as rapidly as they would along an isotherm (Fig. 5-4e). In other words, the steep mantle geotherm in the D'' region would suppress the nonlinearity of the post-perovskite phase fraction profile and prevent the post-perovskite transition from completing.

Studies [McCammon, 1997; Sinmyo *et al.*, 2006] have found a significant fraction of Fe is Fe^{3+} ($\text{Fe}^{3+}/\Sigma\text{Fe} \simeq 60\%$) in perovskite and post-perovskite through the charge coupled substitution with Al. In the case of Al and Fe^{3+} , there is no effect from partitioning with other phases, such as ferropericlase, because they do not enter ferropericlase and CaSiO_3 perovskite remains nearly pure [Hirose *et al.*, 1999]. Because Fe^{3+} alone does not increase the thickness as shown by our data in $(\text{Mg}_{0.91}\text{Fe}_{0.09}^{3+})(\text{Fe}_{0.09}^{3+}\text{Si}_{0.91})\text{O}_3$, we attribute the large thickness found in $(\text{Mg}_{0.9}\text{Fe}_{0.1}^{3+})(\text{Al}_{0.1}\text{Si}_{0.9})\text{O}_3$ to the effect of Al, which is also consistent with previous studies [Tateno *et al.*, 2005; Nishio-Hamane *et al.*, 2007]. The result reveals that the post-perovskite phase fraction may increase rapidly at the top of the mixed phase region (Fig. 5-4f), which is consistent with the observations that Al increases the post-perovskite transition pressure and partitions into perovskite over post-perovskite [Ono and Oganov, 2005; Tateno *et al.*, 2005]. However, as shown in Fig. 5-4f, the steep temperature increase in the D'' layer decreases the rate of increase of the post-perovskite fraction and prevents the post-perovskite phase transition from completing in the lower

mantle. Therefore, the post-perovskite boundary remains thick.

Mg-silicates in a pyrolitic composition are expected to contain 5–15 mol% of Fe (60% of Fe is Fe^{3+} in the presence of Al) and 7–12 mol% of Al [McCammon, 1997; Mao *et al.*, 2004; Murakami *et al.*, 2005; Sinmyo *et al.*, 2006], which are similar to the compositions studied here. While the post-perovskite boundary thickness in $(\text{Mg},\text{Fe}^{2+})\text{SiO}_3$ may decrease substantially by the Fe buffering of ferropericlase, the thickness of the post-perovskite boundary in a pyrolitic composition would remain much greater than the thickness of the D'' discontinuity [Lay, 2008] because of the large increase in the boundary thickness by Al and the large radial temperature gradient in the D'' layer. In other words, the D'' layer may consist of mixed phases of perovskite + post-perovskite + ferropericlase instead of pure post-perovskite with ferropericlase, if the bulk composition of the lowermost mantle is pyrolitic.

The large thickness of the post-perovskite boundary may profoundly impact dynamics in the D'' layer. The large positive Clapeyron slope of the post-perovskite boundary would increase the density contrast between thermal heterogeneities and bulk mantle, intensifying thermal mantle flow as shown by computer simulations [Nakagawa and Tackley, 2004], which is not compatible with the seismic observations of the large low shear-wave velocity provinces (LLSVP) at the lowermost mantle and the stable large-scale mantle plume model [Garnero *et al.*, 2007]. However, the large thickness of the post-perovskite boundary would spread the effect of the Clapeyron slope over a wide depth range, reducing the effects of the post-perovskite boundary on the density contrast and therefore stabilizing high-temperature anomalies in the D'' region. This effect would be particularly strong in regions with high Al content and/or low Mg/Si ratio (such as basaltic materials), stabilizing the chemical heterogeneities in the D'' layer.

A sharp D'' discontinuity has been observed in some regions of the D'' layer [Lay *et al.*,

2006; *van der Hilst et al.*, 2007]. Therefore, the discrepancy in thickness between the post-perovskite boundary in pyrolite-related compositions and the D'' discontinuity raises important questions about the origin of the D'' discontinuity. According to our results, the detectability of the post-perovskite boundary can be enhanced in regions with a high Mg/Si ratio and low Al content, requiring compositional changes for the observation of a sharp post-perovskite boundary. In addition, it has been proposed that strong texturing of post-perovskite might enhance the detectability of the post-perovskite boundary [*Murakami et al.*, 2005].

It is also notable that multiples of laterally extending reflectors have been identified together with a pair of discontinuities inferred to be the double crossing of the D'' discontinuity within the bottom 400-km of the lower mantle [*Lay et al.*, 2006; *van der Hilst et al.*, 2007; *Hutko et al.*, 2008]. In addition, strongly tilted sharp boundaries have been documented in seismic studies of the LLSVP in the lowermost mantle [*Ni et al.*, 2002]. These observations are difficult to explain by a single isochemical phase transition.

Thickness of the post-perovskite boundary in MORB-type composition

*This data presented in this chapter is in preparation for publication as:
B. Grocholski, K. Catalli, S.-H. Shim, and V.B. Prakapenka. Mineralogical effects on the detectability of the post-perovskite transition.*

Abstract

Based on our previous experiments looking at a perovskitic mineralogy, the thickness of the perovskite \rightarrow post-perovskite phase transition with iron and aluminum contents relevant to pyrolite cannot adequately explain the D'' discontinuity [Catalli *et al.*, 2009]. However, background phases are known to influence the thickness of phase transitions through element partitioning. Here we investigate the depth and thickness of the post-perovskite transition in a basaltic-like (N-MORB) composition. The results reveal a relatively narrow perovskite + post-perovskite mixed phase field of ~ 100 - 300 km at ~ 400 km above the core-mantle boundary, a depth that matches well with the observed depth of the D'' discontinuity. Combined with new results on harzburgite, our results suggest that if the post-perovskite phase transition is the cause of the the D'' discontinuity, it may only be seismically detectable in regions where subducted materials have accumulated.

6.1 Introduction

The D'' layer is defined by a discontinuous increase in shear wave velocity in the lowest 100–400 km of the Earth's mantle [Lay *et al.*, 1998; Wysession *et al.*, 1998]. For years the origin of the discontinuity was under debate. However, in 2004, a phase transition was discovered in Mg-silicate perovskite, the dominant mantle mineral, at pressures that reasonably match those expected for the D'' discontinuity [Murakami *et al.*, 2004; Oganov and Ono, 2004; Shim *et al.*, 2004]. Pure MgSiO₃ was found to transform from the orthorhombic *Pbmn* perovskite (Pv) structure to the post-perovskite (PPv) phase, a layered orthorhombic structure with spacegroup *Cmcm* [Oganov and Ono, 2004].

Many interesting properties had been found for the D'' layer, differentiating it from the overlying mantle. For the perovskite→post-perovskite transition to suitably explain the D'' discontinuity, the physical properties of post-perovskite need to match the properties of D''. The calculated density and shear wave velocity changes associated with the post-perovskite transition [Oganov and Ono, 2004] match well with the seismic observations of the discontinuity [Sidorin *et al.*, 1999]. Multiple studies have demonstrated seismic anisotropy in D'', measured by the splitting of shear wave velocities [Garnero and Lay, 1997]. Recent deformation experiments at D'' conditions show that the deformation mechanisms of post-perovskite are consistent with seismic observations of shear wave splitting in D'' [Miyagi *et al.*, 2010]. Post-perovskite has also been used to explain regions of ultra-low velocities (velocity decreases of ~10%) in D'' [Garnero and Helmberger, 1995] through significant iron enrichment (up to 40% of the FeSiO₃ component) of the phase [Mao *et al.*, 2006]. Topography of the D'' discontinuity and lens-shaped structures have been attributed to the large Clapeyron slope of the transition and the steep temperature profile near the core-mantle boundary, resulting in depression of the perovskite→post-perovskite boundary in

warmer regions or a double-crossing of the boundary in cooler regions, respectively [Hernlund *et al.*, 2005; Lay *et al.*, 2006; van der Hilst *et al.*, 2007]. However, any phase transition with variable composition has a finite pressure interval over which both the low and high pressure phases will coexist. For the post-perovskite transition to satisfactorily explain the D'' transition, the region where perovskite and post-perovskite coexist in a mantle relevant composition must be consistent with seismic observations that give a D'' thickness of less than 70 km [Wysession *et al.*, 1998; Lay, 2008].

In our previous work, we investigated the effect of ferrous iron, ferric iron and aluminum on the depth and thickness of the post-perovskite boundary in a system containing only Mg-silicate [Catalli *et al.*, 2009]. We found that when perovskite contains iron and aluminum contents relevant to pyrolite, the transition takes place over a depth interval of 400–600 km, much too broad of a mixed phase region to match seismic observations [Catalli *et al.*, 2009]. However, based on calculations in aluminum-free, iron-bearing compositions, the inclusion of ferropericlase buffers the iron in the system, thinning the boundary from ~400 km for a 9 mol% iron system with no ferropericlase to ~50 km when 50 mol% ferropericlase is included [Catalli *et al.*, 2009].

In addition to ferropericlase, there are multiple phases that may be important in the lowermost mantle (CaSiO₃ perovskite, silica, calcium ferrite-type phase, etc.) and more compositional space left to explore. In this study, we measure the depth and thickness of the perovskite → post-perovskite transition in a basaltic-like composition (henceforth, the term 'basalt' will refer to the bulk composition and not the actual rock). Results on pyrolitic and harzburgitic-type compositions will also be published by our group [Grocholski *et al.*, 2011]. The measurements presented here have been made to be internally consistent with our group's other work on the post-perovskite transition [Catalli *et al.*, 2009; Grocholski *et al.*, 2011] to allow for direct comparison between compositions.

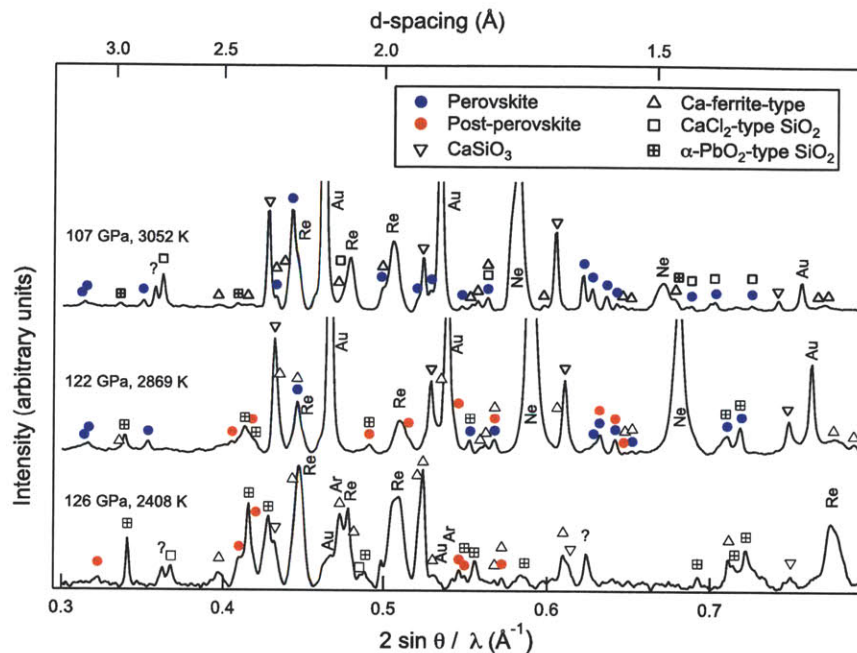


Figure 6-1: Representative X-ray diffraction patterns of basaltic composition at lowermost mantle conditions, in the perovskite (top), Pv+PPv (middle), and post-perovskite (bottom) stability fields.

6.2 Methods

The starting material was a glass synthesized using the laser levitation method. The composition is based on an average of normal mid-ocean ridge basalts collected around the world [Presnall and Hoover, 1987], restricted to the MgO-SiO₂-FeO-CaO-Al₂O₃-Na₂O system. The starting material for the glass was a mixture of synthetic oxides of SiO₂, MgO, FeO, and Al₂O₃, with a CaSiO₃ glass previously synthesized by laser levitation, and NaAlSi₃O₈, a natural Amelia albite (Mineralogical Museum at Harvard University, sample #126680). The composition of the glass was determined by electron microprobe analysis at MIT and is presented in Table 6.1. There was some volatile loss during glass synthesis which resulted in a reduction in the amount of SiO₂ and FeO and enrichment in Al₂O₃, MgO, CaO,

and Na₂O relative to the ideal composition.

Six basalt samples were prepared for determination of the perovskite → post-perovskite phase boundary. Rhenium gaskets were pre-indented with 150 μm culet beveled diamond anvils in symmetric type diamond anvil cells. A pre-pressed sample platelet of basalt glass mixed with 10 weight% gold for use as a pressure standard was placed in a 90 μm hole drilled into the rhenium gasket. The sample platelet was separated from the diamond anvil by a few micron-sized grains of the sample material to allow the pressure medium to flow around the sample and insulate it from the diamonds during laser-heating. In two samples, argon was cryogenically loaded as the pressure medium and thermal insulator. In the remaining four samples, neon was loaded using the gas-loading system at GSECARS; neon-loaded samples also had a ~ 5 μm ruby sphere placed at the edge of the sample chamber for pressure determination during gas loading.

In situ X-ray diffraction and double-sided laser heating using a flat-top laser system [Prakapenka *et al.*, 2008] were performed at the GSECARS sector, beamline 13-IDD, of the Advanced Photon Source. The X-ray beam spot on the sample was 4 × 5 μm² and was coaxially aligned with the laser spots which had a diameter of 20 μm. X-ray diffraction patterns at high temperature were typically collected in 15-30 sec. The temperature of the sample was estimated by fitting the thermal radiation from the sample to Planck's equation [Jeanloz and Heinz, 1984]. Laser heating was performed in cycles of approximately 30 minutes to prevent overheating of the diamond cell. The sample was heated for 60-90 minutes at a given starting pressure before it was determined that the sample was well-crystallized and likely in the equilibrium phase assemblage. All diffraction patterns show clear diffraction from the pressure medium, ensuring quasi-hydrostaticity and good insulation between the sample platelet and the diamonds (Fig. 6-1).

6.3 Results

In basalt, the general lowermost mantle phase assemblage consists of Mg-silicate perovskite and/or post-perovskite, CaSiO₃ perovskite, CaCl₂-type and/or α -PbO₂-type silica, and the Ca-ferrite-type aluminous phase. Based on the starting material, we expect the proportions of phases to be roughly ~35 mol% Mg-silicate, ~35 mol% silica, ~20 mol% CaSiO₃ perovskite, and ~10 mol% of the Ca-ferrite type phase, in agreement with the diffraction patterns (Fig. 6-1). However, due to the higher symmetry of silica and CaSiO₃ perovskite, they are expected to diffract relatively strongly. Because of its low concentration and lower scattering, the diffraction lines of the Ca-ferrite type phase are difficult to distinguish among the other phases (Fig. 6-1).

Six different basalt sample loadings were prepared to investigate the post-perovskite transition (Fig. 6-2). In the first sample, at 105 GPa and 3000 K, perovskite was found to be the stable Mg-silicate. Pressure was then increased on this sample to 114 GPa and 2800 K, where diffraction peaks for the post-perovskite phase grew and coexisted with perovskite. A second sample was taken to 100 GPa and 2500 K, and again perovskite was found to be the stable phase, with no evidence for post-perovskite. Pressure was then increased to 105 GPa and 2800 K, and the sample was still determined to be in the perovskite field. The third sample, was first heated at 115 GPa and 2600 K and found to be in the mixed phase field. The sample was then decompressed to 95 GPa and 2600 K where perovskite diffraction peaks grew and the post-perovskite phase disappeared. In the fourth and fifth samples, the first syntheses were made at 118 GPa and 122 GPa and 3000 K, and were both determined to be in the mixed phase region. In the sixth sample, at 126 GPa and 2500 K, pure post-perovskite was synthesized. After decreasing pressure slightly, and heating the sample to 2500-3000 K, post-perovskite remained the stable phase.

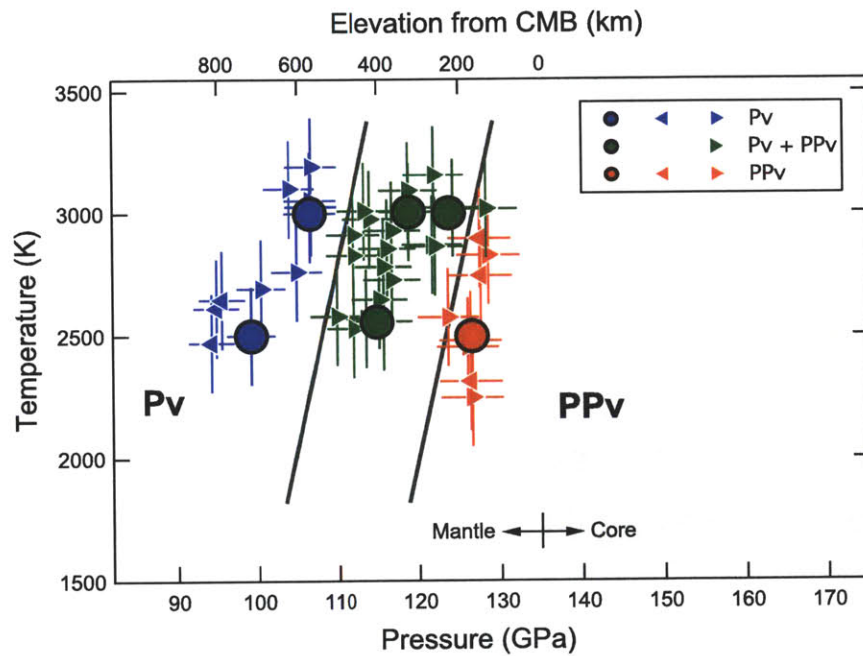


Figure 6-2: Pressure–temperature phase stability for perovskite (Pv) and post-perovskite (PPv) in a basaltic composition. Blue symbols mark the stability field of perovskite, red symbols for post-perovskite, and green for Pv+PPv mixed phase. Right-pointing arrows denote measurements made on compression, left arrows denote measurements made on decompression, and the circles show the first synthesis made from the glass starting material. The Clapeyron slope presented is that determined in *Catalli et al.* [2009].

Our data on the perovskite \rightarrow post-perovskite transition in a basaltic composition show a Pv+PPv mixed phase region spanning between 5–14 GPa (Fig. 6-2). In the lowermost mantle; this corresponds to a depth interval of \sim 100–300 km.

Concurrent with the perovskite \rightarrow post-perovskite phase transition, silica also undergoes a transition from the orthorhombic CaCl_2 -type phase to the orthorhombic $\alpha\text{-PbO}_2$ -type phase. This transition takes place over a wide pressure range. The $\alpha\text{-PbO}_2$ -type phase first appears near 110 GPa, but it persists on decompression down to 95 GPa. The samples synthesized above 122 GPa, in the post-perovskite field, show either no CaCl_2 -type, or only a very little. A notable feature of the phase transition in silica can be seen in the volume relationship between the two phases (Fig. 6-3). The volume of the $\alpha\text{-PbO}_2$ -type phase, the higher pressure phase, is \sim 1.3% larger than the coexisting lower pressure phase at 109 GPa. This is in contrast to pure SiO_2 CaCl_2 and $\alpha\text{-PbO}_2$ where CaCl_2 has a volume 1.6% greater than $\alpha\text{-PbO}_2$. There is a large amount of scatter in the volume data for silica due to diffraction peak overlaps, however, just using the well-separated low angle diffraction lines to compare the phases confirms that the volume difference is robust.

CaSiO_3 perovskite shows strong, clear diffraction lines in the basalt diffraction patterns (Fig. 6-1). During heating, CaSiO_3 perovskite was the first phase to crystallize. At high temperatures it exists in the cubic phase. When the sample is quenched to 300 K, the cubic 200 and 211 diffraction lines split, signaling a reduction in symmetry to a tetragonal perovskite structure [Shim *et al.*, 2002].

Because the diffraction patterns are complicated by the coexistence of 5–7 different phases, unambiguous identification of all diffraction lines and determination of the presence of unknown lines can be difficult. However, there are several unknown lines that can be clearly identified. At 1.6 \AA^{-1} there is an unknown line that is only seen in the presence of post-perovskite (Fig. 6-1, bottom diffraction pattern). This line may be indicative of one

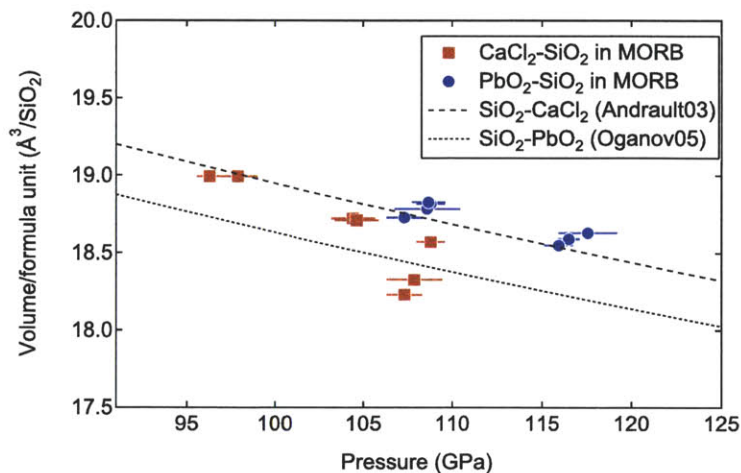


Figure 6-3: Pressure–volume relationship in SiO₂ phases in basaltic composition. Andraut03: *Andraut* [2003]; Oganov05: *Oganov et al.* [2005]. The CaCl₂ and α -PbO₂ volumes measured at 109 GPa were from coexisting phases calculated using the same diffraction pattern. See text for discussion of data scatter.

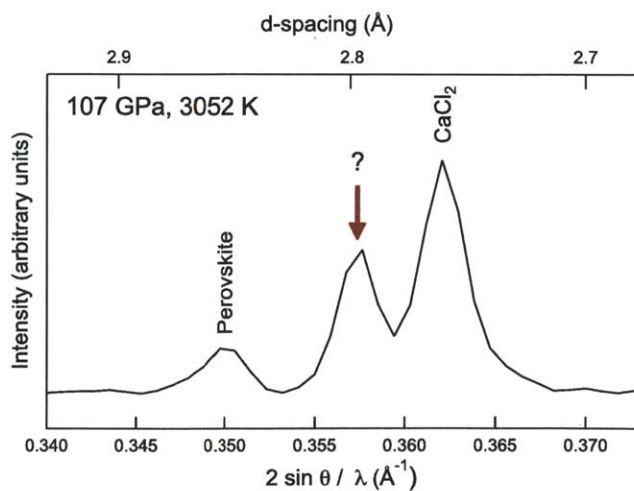


Figure 6-4: Representative X-ray diffraction pattern showing the unknown line associated with CaCl₂-type SiO₂. The unknown line is only seen along with CaCl₂ and appears in 80% of diffraction patterns in the CaCl₂-type.

of the proposed stacking structures of post-perovskite [Tschauner *et al.*, 2007]. There is also an unknown line at $\sim 0.62 \text{ \AA}^{-1}$ that exists as a shoulder of the 110 line of CaCl₂-type silica (Fig. 6-4). This line appears only in conjunction with CaCl₂-type silica, and exists in 80% of those diffraction patterns. In addition, in the 2D diffraction images, the morphology of the line seems to match well with the CaCl₂-type silica. It may be a result of a distortion in the CaCl₂-type structure.

6.4 Discussion

Because of the relatively weak diffraction of Mg-silicate and its overlap with the diffraction lines of the other phases, it can be difficult to distinguish between a sample that is in the mixed phase region but near the phase boundary with a high ratio of one phase to another from a sample that is in the pure phase field. This contributes to the error in the location of the boundaries. In addition, the large number of phases involved and the more complicated chemical composition, increase kinetic problems in determining the equilibrium phase boundaries. Because of this, we consider both an upper and a lower phase boundary for the system (Fig. 6-5) phase relations determined from the first synthesis (circles in Fig. 6-2).

Previous experimental work on the effect of chemical composition on the post-perovskite boundary is shown in Fig. 6-5. All compositions presented in Fig. 6-5, except those for basalt, were measured on perovskitic starting materials. There seems to be a consensus that has developed among the previous work: ferrous iron broadens and shallows the boundary [Mao *et al.*, 2004; Catalli *et al.*, 2009], ferric iron has little effect on the boundary thickness [Catalli *et al.*, 2009], and aluminum broadens the boundary and also pushes it to greater depth [Tateno *et al.*, 2005; Nishio-Hamane *et al.*, 2007; Catalli *et al.*, 2009; Andrault *et al.*,

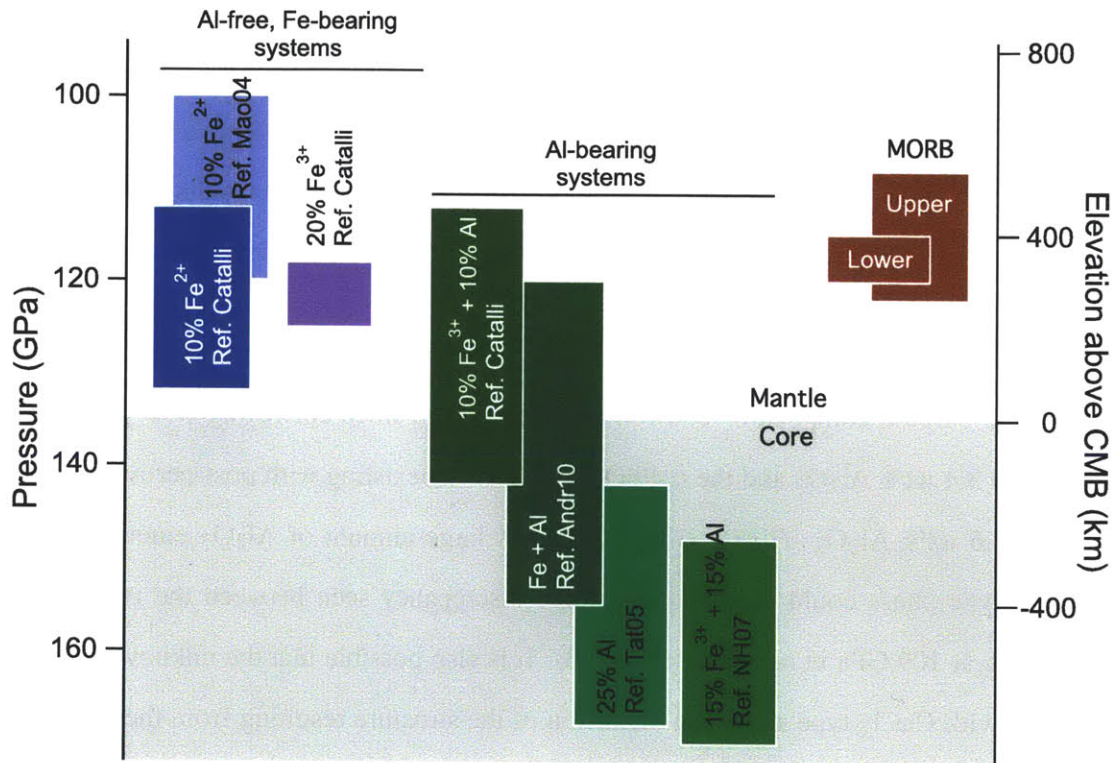


Figure 6-5: Summary of compositional effects on the depth and thickness of the post-perovskite boundary at 2500 K. Catalli: *Catalli et al.* [2009]; Mao04: *Mao et al.* [2004]; Andr10: *Andrault et al.* [2010]; Tat05: *Tateno et al.* [2005]; NH07: *Nishio-Hamane et al.* [2007]. Upper and lower thickness bounds are given for basalt due to the uncertainty in the phase boundary.

2010]. Computational results also agree with these conclusions [Akber-Knutson *et al.*, 2005; Caracas and Cohen, 2005; Mao *et al.*, 2005; Ono and Oganov, 2005]. All of these compositions yield mixed phase regions of hundreds of kilometers (Fig. 6-5), which is in contrast with the seismic thickness of the D'' discontinuity, which is less than 70 km [Wyssession *et al.*, 1998; Lay *et al.*, 1998]. The previous results on perovskitic mineralogy strongly contrast with the results found here: this composition is characterized by high Fe/Mg, low Mg/Si and a significant amount of aluminum, yet still produces a narrow mixed phase region and a relatively low transition pressure. However, these results can be easily reconciled with the previous studies by the buffering effects of the other minerals in basalt.

Silica is capable of containing significant amounts of Al_2O_3 at high pressure. Previous work on a basaltic composition showed that CaCl_2 -type silica coexisting with perovskite contained 3.4 wt% Al_2O_3 and the $\alpha\text{-PbO}_2$ -type silica coexisting with post-perovskite contained 12.6 wt% Al_2O_3 [Hirose *et al.*, 2005]. A large amount of Al_2O_3 entering in the $\alpha\text{-PbO}_2$ -type phase could explain the volume discrepancy seen between the two phases coexisting at 109 GPa in our study (Fig. 6-3). It is also possible that the unknown line associated with CaCl_2 -type silica is a distortion of the structure resulting from the inclusion of Al_2O_3 (Fig. 6-4).

In addition to silica, the Ca-ferrite type phase has a highly variable composition that can accommodate some amount of every component in this system. The Ca-ferrite type phase is expected to carry most of the Na as well as the majority of the aluminum in addition to containing magnesium, iron, and silicon [Hirose *et al.*, 2005]. As a result of these other phases, the Mg-silicates can remain relatively free of these elements. Silica and Ca-ferrite act as buffering phases, narrowing the perovskite \rightarrow post-perovskite phase boundary despite the high Fe/Mg, low Mg/Si and high aluminum concentration in basalt.

6.5 Geophysical implications

Considering the uncertainties in the data and the pressure standard, the following conclusions are the most robust: using the results of *Catalli et al.* [2009] and *Grocholski et al.* [2011] for harzburgitic and pyrolitic compositions, (1) the perovskite→post-perovskite transition occurs at shallower depths in harzburgitic and basaltic compositions compared with pyrolite by 200 and 400 km, respectively, and (2) the mixed phase regions are narrower in harzburgitic (~100 km) and basaltic (100–300 km) compositions than pyrolite (~600 km). Although basalt contains much more aluminum, the presence of phases which can buffer its effects, gives it a significantly narrower boundary than pyrolite. The seismic detectability of the perovskite→post-perovskite transition in basalt may be further enhanced by lattice preferred orientation [*Ammann et al.*, 2010] and/or a nonlinear increase in the post-perovskite phase fraction [*Stixrude*, 1997]. These results suggest that the D'' discontinuity may only exist in regions of the lowermost mantle where basalt and harzburgite, differentiated slab material, may have accumulated.

When oceanic lithosphere is subducted into the Earth's interior, it may not subduct as a cohesive slab throughout the mantle, but may instead separate due to the density differences between the different lithologies that make up the slab. Although the basaltic component has been shown to be positively buoyant in the 600–800 km range, it becomes negatively buoyant again below these depths [*Hirose et al.*, 1999]. Mineralogical and geodynamic modeling of subduction and mixing in the mantle support the accumulation of basaltic composition materials collecting near the core-mantle boundary [*Xu et al.*, 2008]. Subducted slabs have been observed seismically to penetrate into the lowermost mantle [*van der Hilst et al.*, 1997] and have been suggested to form slab graveyards that persist for at least hundreds of millions of years [*Van der Voo et al.*, 1999]. Although global coverage

is limited, large regions of lateral extension of the D'' discontinuity have been documented in the lowermost mantle beneath the Circum-Pacific, regions where subducted slabs would be deposited at the base of the mantle [Lay *et al.*, 1998; Hutko, 2006; van der Hilst *et al.*, 2007].

Table 6.1: Electron microprobe results for the synthetic MORB-like glass used as a starting material. Composition is presented in weight%. *All iron calculated as FeO.

Oxide	wt%
SiO ₂	45.09
Al ₂ O ₃	17.79
FeO*	5.97
MgO	13.14
CaO	13.09
Na ₂ O	4.91

A Crystalline-to-Crystalline Phase Transition in $\text{Ca}(\text{OH})_2$ at 8 GPa and Room Temperature

*K. Catalli, S.-H. Shim, and V.B. Prakapenka (2008). A crystalline-to-crystalline phase transition in $\text{Ca}(\text{OH})_2$ at 8 GPa and room temperature. *Geophysical Research Letters*, 35, L05312. Reproduced/modified by permission of American Geophysical Union.*

Abstract

X-ray diffraction and Raman spectroscopy measurements reveal that $\text{Ca}(\text{OH})_2$ -portlandite transforms to a crystalline phase with an ordered OH sublattice between 8 and 14 GPa at room temperature under quasi-hydrostatic stress conditions in an Ar pressure medium. The amorphization previously reported at 11 GPa under no pressure medium [Meade and Jeanloz, *Geophys. Res. Lett.* **17**, 1157 (1990)] was not observed up to 26 GPa. The width and separation of the fluorescence peaks from the ruby chips embedded in $\text{Ca}(\text{OH})_2$ without a medium suggest that deviatoric stress is responsible for the previously observed amorphization. Our study demonstrates that the behavior of hydrous phases in the subducting slab could be sensitive to local deviatoric stresses. Together with similar reports on quartz, our observation on $\text{Ca}(\text{OH})_2$ indicates that deviatoric stress is an important factor to consider for pressure-induced amorphization reported in a wide range of materials.

A.1 Introduction

Pressure-induced amorphization has been documented in a large number of materials over the last few decades [Sharma and Sikka, 1996]. Ca(OH)₂-portlandite has been regarded as a prime example of pressure-induced amorphization for hydrous materials. The mineral has a simple 2-D structure consisting of layers of CaO₆ octahedra parallel to (001) and O–H bonds oriented parallel to the *c*-axis, making it ideal for studying the role of OH bonding for the stability of crystal structures at high pressure. Also, it provides insight into the behavior of structurally complex hydrous minerals, such as serpentine, the high pressure stability of which is important for understanding the transport of water to the deep interior of the Earth. Additionally, the amorphization of hydrous materials at high pressure has been proposed as the source of deep focus earthquakes at subduction zones [Meade and Jeanloz, 1991].

Meade and Jeanloz [1990] reported the disappearance of diffraction lines of Ca(OH)₂ between 10.7 and 15.4 GPa, suggesting amorphization. A rapid broadening of the OH stretching vibrational modes was observed at the amorphization pressure [Kruger *et al.*, 1989; Duffy *et al.*, 1995], indicating disordering of the OH sublattice. A later diffraction study confirmed the amorphization [Nagai *et al.*, 2000]. However, all of these measurements were conducted without a pressure transmitting medium [Meade and Jeanloz, 1990; Duffy *et al.*, 1995], or with a rigid silicon oil medium [Nagai *et al.*, 2000]. Ekbundit *et al.* [1996] confirmed the amorphization in powder samples but reported a transition to a crystalline phase occurring at 6 GPa and room temperature in single crystal Ca(OH)₂. They attributed the different high-pressure behavior to the effect of grain size.

Here we investigate the high-pressure behavior of powder Ca(OH)₂ samples to 26 GPa under quasi-hydrostatic conditions by X-ray diffraction (XRD) and Raman spectroscopy.

We have found a transition to a crystalline phase at 8 GPa and room temperature. We show that the earlier observations of amorphization were due to deviatoric stress.

A.2 Experimental

Synthetic Ca(OH)_2 (Sigma-Aldrich, 99.995% purity) was gently ground with 10 wt% Au as an internal pressure standard [Shim *et al.*, 2002] for XRD measurements. The sample mixture was pressed to a foil and loaded into a diamond-anvil cell with Ar for use as a pressure medium. Angle dispersive diffraction measurements were performed using a monochromatic X-ray beam (30 keV) and a Mar345 imaging plate at beamline 12.2.2 of the Advanced Light Source (ALS) and the GSECARS sector of the Advanced Photon Source (APS). X-ray semi-transparent cBN seats allow us to measure a diffraction angle up to $22^\circ 2\theta$. Diffraction images were reduced to 1-D diffraction patterns using FIT2D [Hammersley, 1997]. Pressure measurements are based on the fitting of 3-5 gold lines.

Raman spectra were measured with the 514.5-nm beam of an Ar/Kr mixed ion laser and a CCD detector. Low-fluorescence natural diamond anvils were used. The spectrometer was calibrated using the Ne emission spectrum with a wavenumber calibration better than 1 cm^{-1} . Pressure was measured from ruby fluorescence spectra [Mao *et al.*, 1986].

A.3 Results

All diffraction lines below 8 GPa are explained by portlandite, pressure scale (Au), and pressure medium (Ar) (Fig. A-1). We observed smooth, continuous diffraction rings of portlandite, indicating that the sample grain size is much smaller than the X-ray beam size ($10 \times 20 \mu\text{m}^2$). There is a significant volume of Ar in our sample loading, evident in the

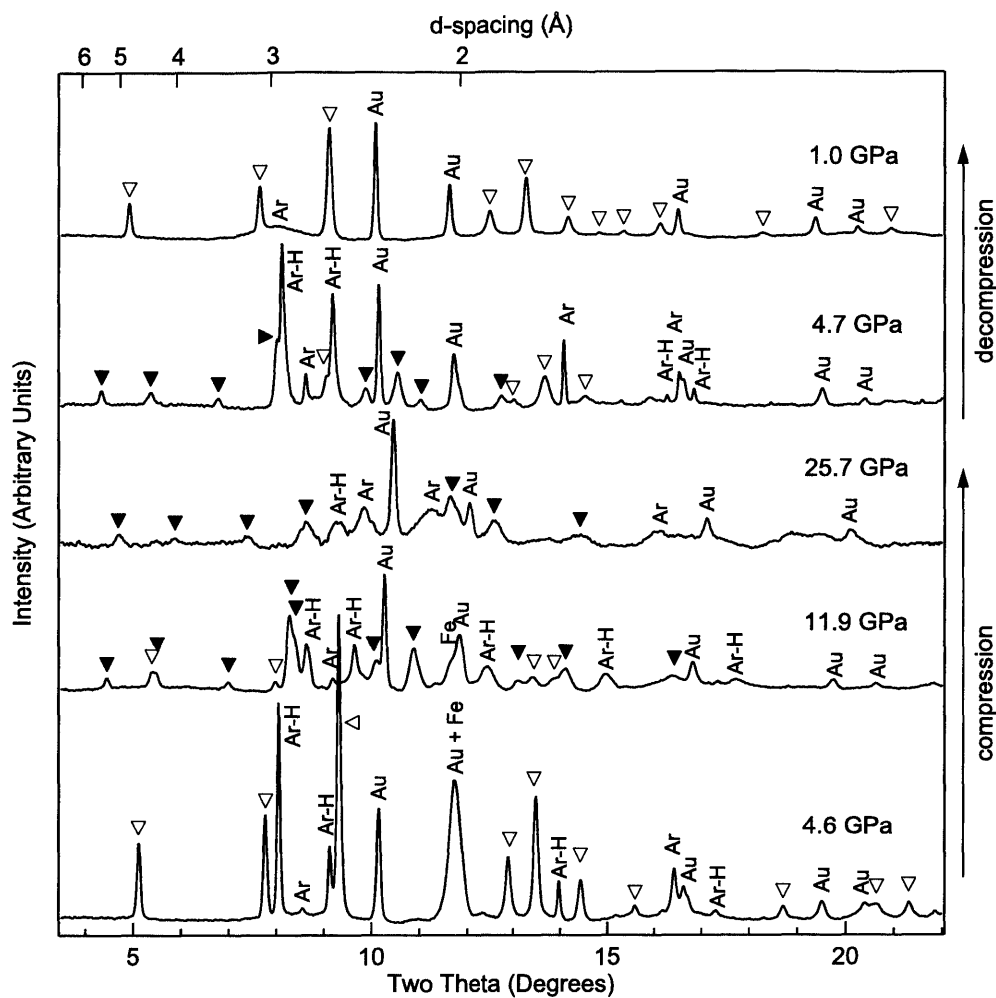


Figure A-1: XRD patterns of $\text{Ca}(\text{OH})_2$ at high pressure. Backgrounds have been subtracted and intensities have been normalized to that of the gold 111 line. Diffraction lines of portlandite and the new high-pressure phase are denoted with open and closed triangles, respectively. Strong diamond and Ar diffraction spots were masked out before integration to 1D patterns. Au: gold pressure standard, Ar: argon pressure medium, Ar-H: diagnostic hcp lines of Ar, Fe: stainless steel gasket.

XRD patterns (Fig. A-1), assuring more hydrostatic conditions than the previous measurements with no pressure medium [Meade and Jeanloz, 1990] or a rigid medium [Nagai *et al.*, 2000]. Our unit-cell parameters and equation of state of portlandite are consistent with the previous measurements within experimental uncertainties up to 10.1 GPa; for example, we obtained $a=3.447(1)$ Å and $c=4.424(2)$ Å at 10.1 GPa which is in agreement with the previous report within 0.8% [Meade and Jeanloz, 1990].

Our Raman observations of portlandite are also in complete agreement with previous studies [Duffy *et al.*, 1995; Ekbundit *et al.*, 1996; Meade *et al.*, 1992] up to 8 GPa (Figs A-2 and A-3). In particular, as observed previously, the OH peak gradually broadens with pressure and is no longer measurable above 10.2 GPa (Fig. A-2b), which has been attributed to disordering of the OH bonds [Kruger *et al.*, 1989; Duffy *et al.*, 1995].

New diffraction lines emerge in XRD patterns between 8.5 and 11.9 GPa and persist to the maximum pressure of this study, 25.7 GPa (Fig. A-1), while the diffraction lines of portlandite weaken with pressure and finally disappear near 11.9 GPa, indicating that $\text{Ca}(\text{OH})_2$ undergoes a phase transition and the new high-pressure phase has long-range order. At 10.1 GPa, the diffraction lines of the high-pressure phase are approximately as broad as the coexisting portlandite lines. The new lines move to lower d -spacing with smaller rates, suggesting that the high-pressure phase is less compressible than portlandite.

Between 9.4 and 12.4 GPa, new lattice modes appear (Figs A-2a and A-3b), again verifying that the high-pressure phase has long-range order. Two new peaks begin to emerge at the OH stretching vibrational frequency range at 9.4 GPa and increase in intensity with pressure to a maximum at 16.2 GPa ($\nu_A(\text{OH})$ and $\nu_B(\text{OH})$ in Figs A-2b, A-3a). The portlandite OH mode coexists up to 10.2 GPa where it finally disappears. The new OH modes have a factor of 3-4 smaller widths than that of portlandite at 10.2 GPa (Fig. A-3c), indicating reordering of the OH sublattice across the phase transition. Both new OH modes

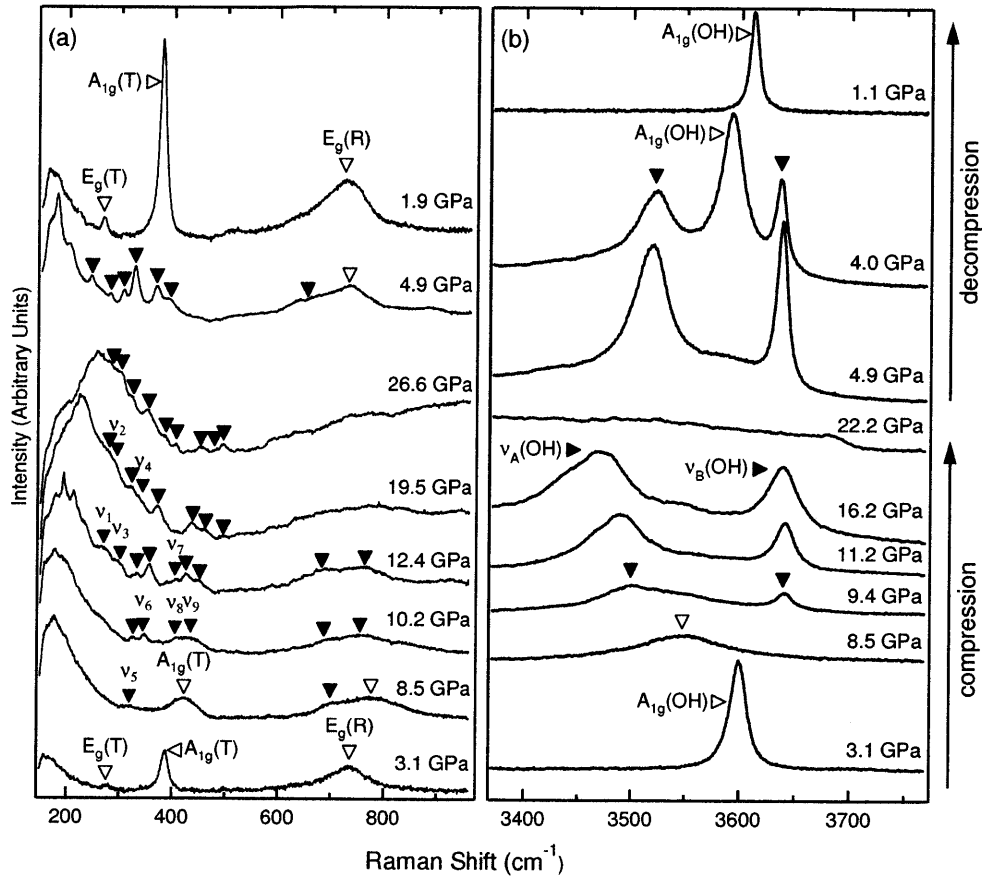


Figure A-2: Raman spectra of $\text{Ca}(\text{OH})_2$ in the regions encompassing the (a) lattice and (b) OH modes. The open and solid triangles represent modes from the low- and high-pressure phases, respectively. Labeling of new modes is in the order of their frequency, v_1 to v_9 . The spectral features below 200 cm^{-1} are from the notch filter.

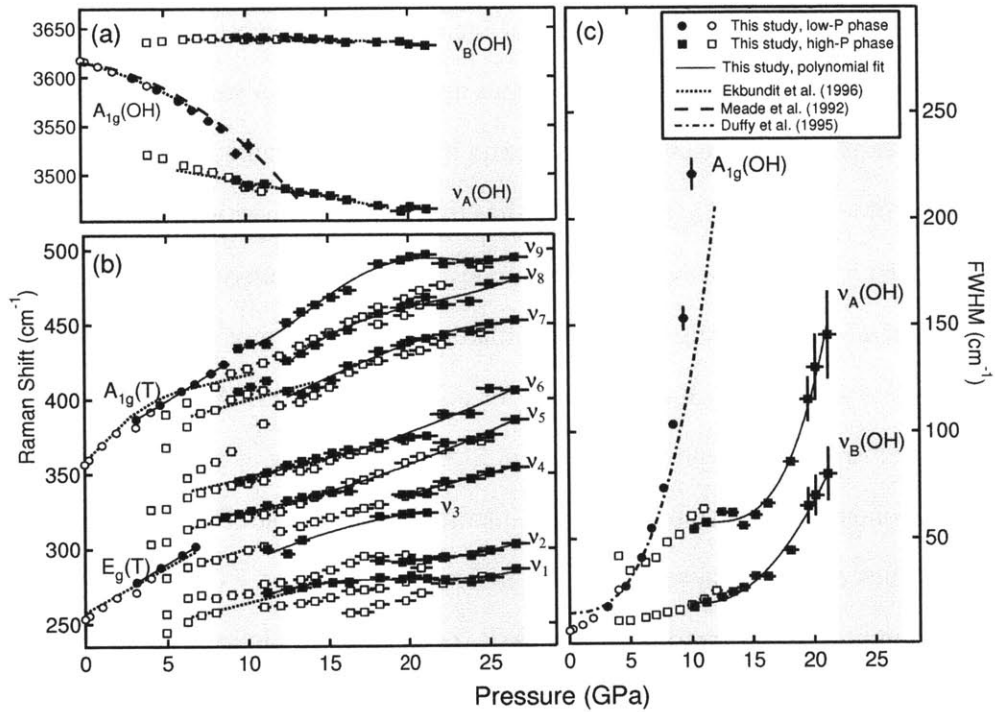


Figure A-3: Pressure-induced Raman mode shifts for $\text{Ca}(\text{OH})_2$ in the (a) OH and (b) lattice regions, along with (c) the FWHM of the OH modes. Solid and open markers denote compression and decompression, respectively. The circles and the squares represent the low- and high-pressure phases, respectively. The first shaded region indicates a mixed low- and high-pressure phase region, while the second shows the pressure range where mode shifts change. For comparison, we show results from other studies [Ekbundit *et al.*, 1996; Meade *et al.*, 1992; Duffy *et al.*, 1995]. A polynomial fit to our data is shown to guide the eye (solid lines in b and c).

show negative pressure shifts and the $\nu_A(\text{OH})$ mode has a much more rapid decrease with pressure. We find a 3- to 4-fold broadening of the OH modes to 21.1 GPa. Above this pressure they are no longer measurable (Figs A-2b and A-3a).

Near 21–22 GPa, coincident with the disappearance of the new OH modes, several lattice modes show a change in their rate of increase in frequency with pressure (Fig. A-3). This may indicate that $\text{Ca}(\text{OH})_2$ undergoes another change in structure at this pressure range. The persistence of the lattice modes and diffraction lines suggest the structure retains long-range order in the Ca-O sublattice but has disordered OH bonds.

During decompression, the two OH modes of the high-pressure phase reappear at 12.0 GPa indicating reordering of the OH sublattice. The lattice modes of the high-pressure phase persist to 4.0 GPa, with no evidence for portlandite modes. At 3.1 GPa, the sample has completely reverted to portlandite. The mode frequencies at ambient pressure after decompression perfectly match those of an uncompressed sample. During decompression, diffraction lines of the high-pressure phase persist until at least 4.7 GPa (Fig. A-1), where the diffraction lines of portlandite appear. At 1.0 GPa, the sample has completely reverted to portlandite. Thus the phase transition observed at 8.5 GPa during compression is reversible.

A.4 Discussion

Both XRD and Raman spectroscopy measurements indicate that the high-pressure phase appearing at 8.5 GPa has long-range order in the Ca-O sublattice with ordered O–H bonds. This is in contrast with previous reports of amorphization at nearly the same pressure [Meade and Jeanloz, 1990; Kruger *et al.*, 1989; Nagai *et al.*, 2000; Duffy *et al.*, 1995]. Furthermore, we do not observe any sign of amorphization up to our maximum pressure

although the O–H bonds disorder at 22.2 GPa. Due to the broadness of its diffraction lines, it is difficult to determine the crystal structure of the high-pressure phase although its d -spacings are consistent with an orthorhombic or monoclinic unit-cell. We compare the XRD patterns of some high-pressure structures reported for brucite-type hydroxides, including $\text{Ca}(\text{OH})_2$ -II reported at 7.2 GPa and 573 K [Kunz *et al.*, 1996] and the $\text{Sr}(\text{OH})_2$ type [Partin and O’Keeffe, 1995]. However, none of these provide satisfactory results for the XRD patterns of the new high-pressure phase. A transition to $\text{Ca}(\text{OH})_2$ -II or $\text{Sr}(\text{OH})_2$ requires major reconstruction of the crystal structure including a coordination number increase for Ca. Therefore, it may be difficult for $\text{Ca}(\text{OH})_2$ to transform directly to these phases at room temperature where the kinetic effects are large.

The most important difference with previous measurements is the use of the soft Ar medium in our study. To evaluate the stress conditions in our sample relative to those in non-hydrostatic experiments, we prepared another sample by filling the sample chamber with the same portlandite powder and a couple of ruby grains without any pressure medium. This is similar to the sample setup of Meade and Jeanloz [1990]. In these measurements, ruby was roughly at the center of the sample chamber, surrounded by portlandite.

In the Ar-loaded sample, the full width at half maximum (FWHM) of R_1 has little change over the pressure range of this experiment (Fig. A-4a). However, in the non-hydrostatic run, the FWHM increases dramatically to about 8 GPa, where it plateaus and then gradually increases above 20 GPa. The R_1 and R_2 lines keep a roughly constant separation in the Ar sample to 26.6 GPa, whereas the non-hydrostatic sample shows a sharp increase in $R_1 - R_2$ to 9 GPa followed by a slight drop and then gradually increases again (Fig. A-4b).

Previous studies have shown that pressure gradients result in broadening of the R_1 ruby line [Chai and Brown, 1996; Shen *et al.*, 2004]. An increase in the $R_1 - R_2$ separation is

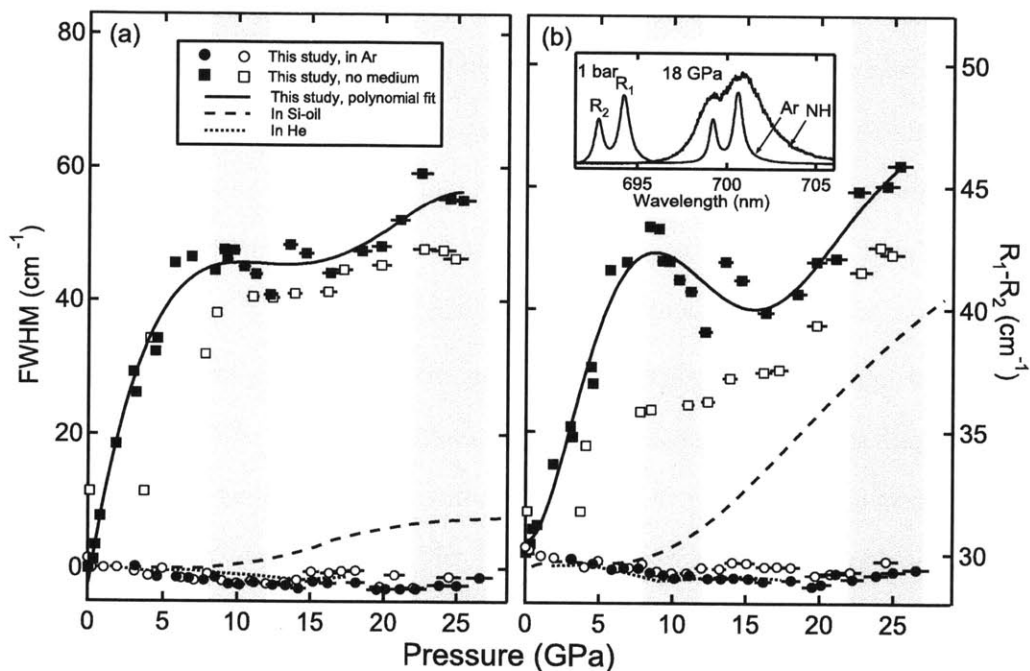


Figure A-4: (a) The R_1 line width and (b) the R_1 and R_2 separation of ruby fluorescence spectra. Circles are from our Raman study with an Ar medium while squares are from a sample loaded with $\text{Ca}(\text{OH})_2$ without a pressure medium (closed and open symbols represent data taken on compression and decompression, respectively). The solid line is a polynomial fit to the non-hydrostatic compression data. We also present measurements in other media [Takemura, 2001; Shen *et al.*, 2004]. The inset shows ruby fluorescence spectra in an Ar medium at 1 bar and 18 GPa, and in no medium (NH) at 18 GPa.

indicative of the development of deviatoric stress because the wavelength of R_2 is only sensitive to the local mean stress while R_1 is affected by deviatoric stress in the sample [Chai and Brown, 1996; Shen *et al.*, 2004]. Therefore, the steep increase in the FWHM of the R_1 ruby line and the $R_1 - R_2$ separation to about 9 GPa without a pressure medium indicate increases in both the pressure gradients and the deviatoric stress with pressure. The flattening, or even decrease in the values, occur over the pressure range reported for the amorphization of non-hydrostatically loaded $\text{Ca}(\text{OH})_2$ [Meade and Jeanloz, 1990; Nagai *et al.*, 2000]. This indicates that deviatoric stresses are responsible for the earlier observation of amorphization. In other words, the deviatoric stress reinforces the system to bypass a transition to an energetically more favorable phase which has long-range order.

Ekbundit et al. [1996] found that single crystal $\text{Ca}(\text{OH})_2$ transforms to a crystalline phase at 6-8 GPa whereas powder samples undergo amorphization at 11 GPa, regardless of the existence of a pressure medium. They attributed the different behaviors to a grain size effect. The Raman spectra of our high-pressure phase are similar to those they found for single crystals in an Ar medium. However, their high-pressure phase observed in single crystal without a pressure medium shows more modes than that in an Ar medium. In addition, they found that single crystal $\text{Ca}(\text{OH})_2$ amorphizes without a pressure medium at 22 GPa, where we clearly see that our sample remains crystalline. Therefore, deviatoric stress still plays a role for their observations, in addition to the grain size effect. The powder results of *Ekbundit et al.* [1996] are in disagreement with our observations. We note that bridging of the sample between the diamond anvils can result in severe deviatoric stress even under an Ar medium.

Pressure-induced amorphization was also reported in serpentine, an important hydrous mineral with a layered structure in subducting slabs, at 6–25 GPa and 300–900 K, with associated acoustic emissions at pressures that coincided with the depths of deep-focus

earthquakes in the down-going slab [Meade and Jeanloz, 1991]. This measurement was conducted without a pressure medium. A subsequent study [Irifune *et al.*, 1996] using a multi-anvil press found a transition to a crystalline phase, instead of amorphization. Based on our results, it is likely that the discrepancy results from deviatoric stress. In addition, the cases of serpentine and portlandite may indicate that the high-pressure behavior of hydrous phases in subducting slabs could be very sensitive to local deviatoric stresses.

Besides Ca(OH)₂, many other materials with different bonding types have been shown to undergo pressure-induced amorphization [Sharma and Sikka, 1996]. An interesting case is quartz. Earlier studies reported a transition to a crystalline phase at 21 GPa and subsequent amorphization at pressures over 30 GPa [Hemley *et al.*, 1988]. However, a more recent study with a quasi-hydrostatic medium, He, has shown that quartz transforms to a crystalline phase at 40 GPa instead [Haines *et al.*, 2001]. The Si–O bond in quartz is both ionic and covalent [Gibbs *et al.*, 1994], whereas Ca(OH)₂ has ionic bonding in the Ca–O sublattice and van der Waals bonding between the Ca–O layers. Nevertheless, they both show extreme sensitivity to deviatoric stresses at high pressure. This implies that pressure-induced amorphization observed in a wide range of materials should be carefully investigated under controlled stress conditions.

Bibliography

- Akahama, Y., and H. Kawamura, Pressure calibration of diamond anvil Raman gauge to 310 GPa, *Journal of Applied Physics*, 100, 043,516, 2006.
- Akber-Knutson, S., G. Steinle-Neumann, and P. D. Asimow, Effect of Al on the sharpness of the MgSiO₃ perovskite to post-perovskite phase transition, *Geophysical Research Letters*, 32(14), 2005.
- Alp, E. E., W. Sturhahn, and T. Toellner, Synchrotron Mössbauer spectroscopy of powder samples, *Nuclear Instruments and Methods in Physics Research Section B*, 97, 526–529, 1995.
- Ammann, M. W., J. P. Brodholt, J. Wookey, and D. P. Dobson, First-principles constraints on diffusion in lower-mantle minerals and a weak D'' layer, *Nature*, 465, 462–465, 2010.
- Andrault, D., Cationic substitution in MgSiO₃ perovskite, *Physics of the Earth and Planetary Interiors*, 136(1-2), 67–78, 2003.
- Andrault, D., and N. Bolfan-Casanova, High-pressure phase transformations in the MgFe₂O₄ and Fe₂O₃-MgSiO₃ systems, *Physics and Chemistry of Minerals*, 28(3), 211–217, 2001.
- Andrault, D., N. Bolfan-Casanova, and N. Guignot, Equation of state of lower mantle (Al,Fe)-MgSiO₃ perovskite, *Earth and Planetary Science Letters*, 193(3-4), 501–508, 2001.
- Andrault, D., M. Munoz, N. Bolfan-Casanova, N. Guignot, J. P. Perillat, G. Aquilanti, and S. Pascarelli, Experimental evidence for perovskite and post-perovskite coexistence throughout the whole D'' region, *Earth and Planetary Science Letters*, 293, 90–96, 2010.

Bibliography

- Auzende, A.-L., J. Badro, F. J. Ryerson, P. K. Weber, S. J. Fallon, A. Addad, J. Siebert, and G. Fiquet, Element partitioning between magnesium silicate perovskite and ferropericlase: New insights into bulk lower-mantle geochemistry, *Earth and Planetary Science Letters*, 269(1-2), 164–174, 2008.
- Badro, J., V. V. Struzhkin, J. F. Shu, R. J. Hemley, and H.-K. Mao, Magnetism in FeO at megabar pressures from X-ray emission spectroscopy, *Physical Review Letters*, 83(20), 4101–4104, 1999.
- Badro, J., G. Fiquet, V. V. Struzhkin, M. Somayazulu, H.-K. Mao, G. Shen, and T. Le Bihan, Nature of the high-pressure transition in Fe₂O₃ hematite, *Physical Review Letters*, 89(20), 205,504, 2002.
- Badro, J., G. Fiquet, F. Guyot, J. P. Rueff, V. V. Struzhkin, G. Vanko, and G. Monaco, Iron partitioning in Earth's mantle: Toward a deep lower mantle discontinuity, *Science*, 300, 789–791, 2003.
- Badro, J., J.-P. Rueff, G. Vankó, G. Monaco, G. Fiquet, and F. Guyot, Electronic transitions in perovskite: Possible nonconvecting layers in the lower mantle, *Science*, 305, 383–386, 2004.
- Bancroft, G. M., A. G. Maddock, and R. G. Burns, Applications of the Mössbauer effect to silicate mineralogy – I. Iron silicates of known crystal structure, *Geochimica Et Cosmochimica Acta*, 31, 2219–2246, 1967.
- Bell, P. M., H.-K. Mao, and J. A. Xu, Error analysis of parameter-fitting in equations of state for mantle minerals, in *High Pressure Research in Mineral Physics*, edited by M. H. Manghnani and Y. Syono, pp. 447–454, Terra Scientific Publishing Company, 1987.
- Bengtson, A., K. Persson, and D. Morgan, Ab initio study of the composition dependence of the pressure-induced spin crossover in perovskite (Mg_{1-x}Fe_x)SiO₃, *Earth and Planetary Science Letters*, 265, 535–545, 2008.
- Bengtson, A., J. Li, and D. Morgan, Mössbauer modeling to interpret the spin state of iron in (Mg,Fe)SiO₃ perovskite, *Geophysical Research Letters*, 36, L15,301, 2009.
- Brodholt, J. P., Pressure-induced changes in the compression mechanism of aluminous perovskite in the Earth's mantle, *Nature*, 407, 620–622, 2000.
- Bullen, K. E., The problem of the Earth's density variation, *Bulletin of the Seismological Society of America*, 30, 235–250, 1940.
- Bullen, K. E., Compressibility–pressure hypothesis and the Earth's interior, *Monthly Notices of the Royal Astronomical Society – Geophysical Supplement*, 5(9), 354–368, 1949.

- Burns, R. G., *Mineralogical Applications of Crystal Field Theory*, second ed., Cambridge University Press, 1993.
- Caracas, R., Elasticity of AlFeO_3 and FeAlO_3 perovskite and post-perovskite from first-principles calculations, *Geophysical Research Letters*, 37, L20,306, 2010.
- Caracas, R., and R. E. Cohen, Effect of chemistry on the stability and elasticity of the perovskite and post-perovskite phases in the MgSiO_3 - FeSiO_3 - Al_2O_3 system and implications for the lowermost mantle, *Geophysical Research Letters*, 32(16), 2005.
- Catalli, K., S.-H. Shim, and V. B. Prakapenka, A crystalline-to-crystalline transition in $\text{Ca}(\text{OH})_2$ at 8 GPa and room temperature, *Geophysical Research Letters*, 35, L05,312, 2008.
- Catalli, K., S.-H. Shim, and V. Prakapenka, Thickness and Clapeyron slope of the post-perovskite boundary, *Nature*, 462, 782–785, 2009.
- Catalli, K., S.-H. Shim, V. B. Prakapenka, J. Zhao, and W. Sturhahn, X-ray diffraction and mössbauer spectroscopy of Fe^{3+} -bearing Mg-silicate post-perovskite at 128–138 GPa, *American Mineralogist*, 95, 418–421, 2010a.
- Catalli, K., et al., Spin state of ferric iron in MgSiO_3 perovskite and its effect on elastic properties, *Earth and Planetary Science Letters*, 289, 68–75, 2010b.
- Chai, M., and J. M. Brown, Effects of static non-hydrostatic stress on the R lines of ruby single crystals, *Geophysical Research Letters*, 23, 3539–3542, 1996.
- Cohen, R. E., I. I. Mazin, and D. G. Isaak, Magnetic collapse in transition metal oxides at high pressure: Implications for the Earth, *Science*, 275, 654–657, 1997.
- Courtier, A. M., and J. Revenaugh, Slabs and shear wave reflectors in the midmantle, *Journal of Geophysical Research*, 113, B08,312, 2008.
- Duffy, T. S., R. J. Hemley, and H.-K. Mao, Structure and bonding in hydrous minerals at high pressure: Raman spectroscopy of alkaline earth hydroxides, in *Volatiles in the Earth and Solar system*, vol. 341, edited by K. A. Farley, pp. 211–220, American Institute of Physics, 1995.
- Dyar, M. D., D. G. Agresti, M. W. Schaefer, C. A. Grant, and E. C. Sklute, Mössbauer spectroscopy of Earth and planetary materials, *Annual Review of Earth and Planetary Sciences*, 34, 83–125, 2006.
- Dziewonski, A. M., and D. L. Anderson, Preliminary reference Earth model, *Physics of the Earth and Planetary Interiors*, 25(4), 297–356, 1981.

Bibliography

- Eggert, J. H., K. A. Goettel, and I. F. Silvera, Elimination of pressure-induced fluorescence in diamond anvils, *Applied Physics Letters*, 53(25), 2489–2491, 1988.
- Ekbundit, S., K. Leinenweber, J. L. Yarger, J. S. Robinson, M. Verhelst-Voorhees, and G. H. Wolf, New high-pressure phase and pressure-induced amorphization of $\text{Ca}(\text{OH})_2$: Grain size effect, *Journal of Solid State Chemistry*, 126, 300–307, 1996.
- Fei, Y., J. Li, K. Hirose, W. Minarik, J. Van Orman, C. Sanloup, W. van Westrenen, T. Komabayashi, and K. Funakoshi, A critical evaluation of pressure scales at high temperatures by in situ X-ray diffraction measurements, *Physics of the Earth and Planetary Interiors*, 143-144, 515–526, 2004.
- Fei, Y., L. Zhang, A. Corgne, H. Watson, A. Ricolleau, Y. Meng, and V. B. Prakapenka, Spin transition and equation of state of $(\text{Mg,Fe})\text{O}$ solid solution, *Geophysical Research Letters*, 34, L17,307, 2007.
- Fiquet, G., A. Dewaele, D. Andrault, M. Kunz, and T. Le Bihan, Thermoelastic properties and crystal structure of MgSiO_3 perovskite at lower mantle pressure and temperature conditions, *Geophysical Research Letters*, 27(1), 21–24, 2000.
- Frost, D. J., C. Liebske, F. Langenhorst, C. A. McCammon, R. G. Trønnnes, and D. C. Rubie, Experimental evidence for the existence of iron-rich metal in the Earth's lower mantle, *Nature*, 428(6981), 409–412, 2004.
- Gamblin, S. D., and D. S. Urch, Metal $K\beta$ X-ray emission spectra of first row transition metal compounds, *Journal of Electron Spectroscopy and Related Phenomena*, 113, 179–192, 2001.
- Garnero, E., Heterogeneity of the lowermost mantle, *Annual Review of Earth and Planetary Sciences*, 28, 509–537, 2000.
- Garnero, E., T. Lay, and A. McNamara, Implications of lower-mantle structural heterogeneity for the existence and nature of whole-mantle plumes, in *Plates, Plumes, and Planetary Processes*, pp. 79–101, Geological Society of America, 2007.
- Garnero, E. J., and D. Helmberger, A very slow basal layer underlying large-scale low-velocity anomalies in the lower mantle beneath the Pacific: evidence from core phases, *Physics of the Earth and Planetary Interiors*, 91, 161–176, 1995.
- Garnero, E. J., and T. Lay, Lateral variations in lowermost mantle shear wave anisotropy beneath the north Pacific and Alaska, *Journal of Geophysical Research*, 102(B4), 8121–8135, 1997.

- Gibbs, G. V., J. W. Downs, and M. B. Boisen, Jr., The elusive SiO bond, in *Silica, Reviews in Mineralogy*, vol. 29, edited by P. J. Heaney, C. T. Prewitt, and G. V. Gibbs, chap. 10, pp. 331–368, Mineralogical Society of America, Washington, D.C., 1994.
- Goncharov, A. F., B. D. Haugen, V. V. Struzhkin, P. Beck, and S. D. Jacobsen, Radiative conductivity in the Earth's lower mantle, *Nature*, 456(13), 231–234, 2008.
- Grocholski, B., S.-H. Shim, W. Sturhahn, J. Zhao, Y. Xiao, and P. C. Chow, Spin and valence states of iron in $(\text{Mg}_{0.8}\text{Fe}_{0.2})\text{SiO}_3$ perovskite, *Geophysical Research Letters*, 36, L24,303, 2009.
- Grocholski, B., K. Catalli, S.-H. Shim, and V. B. Prakapenka, Mineralogical effects on the detectability of the post-perovskite boundary, *in preparation*, 2011.
- Guignot, N., D. Andraut, G. Morard, N. Bolfan-Casanova, and M. Mezouar, Thermoelastic properties of post-perovskite phase MgSiO_3 determined experimentally at core-mantle boundary $P - T$ conditions, *Earth and Planetary Science Letters*, 256(1-2), 162–168, 2007.
- Haines, J., J. Leger, F. Gorelli, and M. Hanfland, Crystalline post-quartz phase in silica at high pressure, *Physical Review Letters*, 87(15), 155,503, 2001.
- Hammersley, A. P., FIT2D: An introduction and overview, *ESRF internal report*, ESRF, 1997.
- Hawthorne, F. C. (Ed.), *Spectroscopic Methods in Mineralogy and Geology, Reviews in Mineralogy*, vol. 18, 698 pp., Mineralogical Society of America, 1988.
- Heinz, D. L., E. Knittle, J. S. Sweeney, Q. Williams, and R. Jeanloz, High-pressure melting of $(\text{mg,fe})\text{siO}_3$ -perovskite, *Science*, 264(5156), 279–280, 1994.
- Hemley, R. J., A. P. Jephcoat, H.-K. Mao, L. C. Ming, and M. H. Manghnani, Pressure-induced amorphization of crystalline silica, *Nature*, 334, 52–54, 1988.
- Hernlund, J. W., and C. Houser, The statistical distribution of seismic velocities in Earth's deep mantle, *Earth and Planetary Science Letters*, 265, 423–437, 2008.
- Hernlund, J. W., C. Thomas, and P. J. Tackley, A doubling of the post-perovskite phase boundary and structure of the Earth's lowermost mantle, *Nature*, 434(7035), 882–886, 2005.
- Hirose, K., Y. W. Fei, Y. Z. Ma, and H. K. Mao, The fate of subducted crust in Earth's lower mantle, *Nature*, 397(6714), 53–56, 1999.

Bibliography

- Hirose, K., N. Takafuji, N. Sata, and Y. Ohishi, Phase transition and density of subducted MORB crust in the lower mantle, *Earth and Planetary Science Letters*, 237(1-2), 239–251, 2005.
- Hirose, K., R. Sinmyo, N. Sata, and Y. Ohishi, Determination of post-perovskite phase transition boundary in MgSiO_3 using Au and MgO pressure standards, *Geophysical Research Letters*, 33(1), L01,310, 2006.
- Hofmeister, A. M., Is low-spin Fe^{2+} present in Earth's mantle?, *Earth and Planetary Science Letters*, 243(1-2), 44–52, 2006.
- Holland, T. J. B., and S. A. T. Redfern, Unit cell refinement from powder diffraction data: The use of regression diagnostics, *Mineralogical Magazine*, 61, 65–77, 1997.
- Holmes, N. C., J. A. Moriarty, G. R. Gathers, and W. J. Nellis, The equation of state of platinum to 660 GPa (6.6 Mbar), *Journal of Applied Physics*, 66, 2962–2967, 1989.
- Horiuchi, H., E. Ito, and D. J. Weidner, Perovskite-type MgSiO_3 : single-crystal X-ray diffraction study, *American Mineralogist*, 72, 357–360, 1987.
- Hsu, H., K. Umemoto, P. Blaha, and R. M. Wentzcovitch, Spin states and hyperfine interactions of iron in $(\text{Mg,Fe})\text{SiO}_3$ perovskite under pressure, *Earth and Planetary Science Letters*, 294, 19–26, 2010.
- Hsu, H., P. Blaha, M. Cococcioni, and R. M. Wentzcovitch, Spin states and hyperfine interactions of ferric iron in MgSiO_3 perovskite, *Physical Review Letters*, p. in print, 2011.
- Hutko, A., T. Lay, J. Revenaugh, and E. Garnero, Anticorrelated seismic velocity anomalies from post-perovskite in the lowermost mantle, *Science*, 320, 1070–1074, 2008.
- Hutko, A. R., Seismic detection of folded, subducted lithosphere at the core-mantle boundary, *Nature*, 441, 333–336, 2006.
- Irifune, T., K. Kuroda, N. Funamori, T. Uchida, T. Yagi, T. Inoue, and N. Miyajima, Amorphization of serpentine at high pressure and high temperature, *Science*, 272, 1468–1470, 1996.
- Jackson, J. M., W. Sturhahn, G. Y. Shen, J. Y. Zhao, M. Y. Hu, D. Errandonea, J. D. Bass, and Y. W. Fei, A synchrotron Mössbauer spectroscopy study of $(\text{Mg,Fe})\text{SiO}_3$ perovskite up to 120 GPa, *American Mineralogist*, 90(1), 199–205, 2005.
- Jamieson, J., J. Fritz, and M. Manghnani, Pressure measurement at high temperature in X-ray diffraction studies: gold as a primary standard, in *High-pressure Research in Geophysics*, edited by S. Akimoto and M. Manghnani, Advances in Earth and Planetary Sciences, pp. 27–48, Center for Academic Publications Japan, 1982.

- Jeanloz, R., and D. L. Heinz, Experiments at high temperature and pressure: laser heating through the diamond cell, *Journal de Physique Colloques*, 45, 83–92, 1984.
- Jeffreys, H., The times of *P*, *S* and *SKS*, and the velocities of *P* and *S*, *Monthly Notices of the Royal Astronomical Society – Geophysical Supplement*, 4, 498–533, 1939.
- Kawakatsu, H., and F. Niu, Seismic evidence for a 920-km discontinuity in the mantle, *Nature*, 371, 301–305, 1994.
- Keppler, H., L. S. Dubrovinsky, O. Narygina, and I. Kantor, Optical absorption and radiative conductivity of silicate perovskite to 125 gigapascals, *Science*, 322, 1529–1532, 2008.
- Kesson, S. E., J. D. Fitzgerald, and J. M. Shelley, Mineralogy and dynamics of a pyrolite lower mantle, *Nature*, 393, 252–255, 1998.
- Kingma, K. J., R. E. Cohen, R. J. Hemley, and H.-K. Mao, Transformation of stishovite to a denser phase at lower-mantle pressures, *Nature*, 374, 243–245, 1995.
- Knittle, E., and R. Jeanloz, Synthesis and equation of state of (Mg,Fe)SiO₃ perovskite to over 100 gigapascals, *Science*, 235(4789), 668–670, 1987.
- Kobayashi, Y., T. Kondo, E. Ohtani, N. Hirao, N. Miyajima, T. Yagi, T. Nagase, and T. Kikegawa, Fe–Mg partitioning between (Mg,Fe)SiO₃ post-perovskite, perovskite, and magnesiowüstite in the Earth's lower mantle, *Geophysical Research Letters*, 32(19), 2005.
- Kruger, M. B., Q. Williams, and R. Jeanloz, Vibrational spectra of Mg(OH)₂ and Ca(OH)₂ under pressure, *Journal of Chemical Physics*, 91, 5910–5915, 1989.
- Kunz, M., K. Leinenweber, J. B. Parise, T. C. Wu, W. A. Bassett, K. Brister, D. J. Weidner, M. T. Vaughan, and Y. Wang, The baddeleyite-type high pressure phase of Ca(OH)₂, *High Pressure Research*, 14, 311–319, 1996.
- Lay, T., Sharpness of the *D''* discontinuity beneath the Cocos Plate: Implications for the perovskite to post-perovskite phase transition, *Geophysical Research Letters*, 35, 2008.
- Lay, T., Q. Williams, and E. J. Garnero, The core-mantle boundary layer and deep Earth dynamics, *Nature*, 392, 461–468, 1998.
- Lay, T., J. Hernlund, E. J. Garnero, and M. S. Thorne, A post-perovskite lens and *D''* heat flux beneath the central pacific, *Science*, 314(5803), 1272–1276, 2006.

Bibliography

- Lee, K. K. M., B. O'Neill, W. R. Panero, S.-H. Shim, L. R. Benedetti, and R. Jeanloz, Equations of state of the high-pressure phases of a natural peridotite and implications for the Earth's lower mantle, *Earth and Planetary Science Letters*, 223(3-4), 381–393, 2004.
- Li, J., W. Sturhahn, J. M. Jackson, V. V. Struzhkin, J. F. Lin, J. Zhao, H. K. Mao, and G. Shen, Pressure effect on the electronic structure of iron in (Mg,Fe)(Si,Al)O₃ perovskite: a combined synchrotron Mössbauer and X-ray emission spectroscopy study up to 100 GPa, *Physics and Chemistry of Minerals*, 33, 575–585, 2006.
- Li, J., et al., Electronic spin state of iron in lower mantle perovskite, *Proceedings of the National Academy of Sciences of the United States of America*, 101(39), 14,027–14,030, 2004.
- Li, L., J. P. Brodholt, S. Stackhouse, D. J. Weidner, M. Alfredsson, and G. D. Price, Electronic spin state of ferric iron in Al-bearing perovskite in the lower mantle, *Geophysical Research Letters*, 32, L17,307, 2005a.
- Li, L., J. P. Brodholt, S. Stackhouse, D. J. Weidner, M. Alfredsson, and G. D. Price, Elasticity of (Mg,Fe)(Si,Al)O₃-perovskite at high pressure, *Earth and Planetary Science Letters*, 240, 529–536, 2005b.
- Lin, J. F., V. V. Struzhkin, S. D. Jacobsen, M. Y. Hu, P. Chow, J. Kung, H. Z. Liu, H. K. Mao, and R. J. Hemley, Spin transition of iron in magnesiowustite in the Earth's lower mantle, *Nature*, 436(7049), 377–380, 2005.
- Lin, J.-F., G. Vankó, S. D. Jacobsen, V. Iota, V. V. Struzhkin, V. B. Prakapenka, A. Kuznetsov, and C.-S. Yoo, Spin transition zone in Earth's lower mantle, *Science*, 317, 1740–1743, 2007.
- Lin, J.-F., et al., Intermediate-spin ferrous iron in lowermost mantle post-perovskite and perovskite, *Nature Geoscience*, 1, 688–691, 2008.
- Liu, L.-G., Post-oxide phases of forsterite and enstatite, *Geophysical Research Letters*, 2(10), 417–419, 1975.
- Loper, D. E., and T. Lay, The core-mantle boundary region, *Journal of Geophysical Research*, 100, 6397–6420, 1995.
- Lundin, S., K. Catalli, J. Santillán, S.-H. Shim, V. B. Prakapenka, M. Kunz, and Y. Meng, Effect of Fe on the equation of state of mantle silicate perovskite over 1 Mbar, *Physics of the Earth and Planetary Interiors*, 168, 97–102, 2008.
- Mao, H.-K., J. Xu, and P. M. Bell, Calibration of the ruby pressure gauge to 800 kbar under quasihydrostatic conditions, *Journal of Geophysical Research*, 91, 4673–4676, 1986.

- Mao, W. L., G. Y. Shen, V. B. Prakapenka, Y. Meng, A. J. Campbell, D. L. Heinz, J. F. Shu, R. J. Hemley, and H. K. Mao, Ferromagnesian postperovskite silicates in the D'' layer of the Earth, *Proceedings of the National Academy of Sciences of the United States of America*, *101*(45), 15,867–15,869, 2004.
- Mao, W. L., H. K. Mao, W. Sturhahn, J. Y. Zhao, V. B. Prakapenka, Y. Meng, J. F. Shu, Y. W. Fei, and R. J. Hemley, Iron-rich post-perovskite and the origin of ultralow-velocity zones, *Science*, *312*(5773), 564–565, 2006.
- Mao, W. L., et al., Iron-rich silicates in the Earth's D'' layers, *Proceedings of the National Academy of Sciences of the United States of America*, *102*(28), 9751–9753, 2005.
- McCammon, C., Perovskite as a possible sink for ferric iron in the lower mantle, *Nature*, *387*, 694–696, 1997.
- McCammon, C., The paradox of mantle redox, *Science*, *308*, 807–808, 2005.
- McCammon, C., M. Hutchison, and J. Harris, Ferric iron content of mineral inclusions in diamonds from Sao Luiz: A view into the lower mantle, *Science*, *278*(5337), 434–436, 1997.
- McCammon, C., I. Kantor, O. Narygina, J. Rouquette, U. Ponkratz, I. Sergueev, M. Mezouar, V. Prakapenka, and L. Dubrovinsky, Stable intermediate-spin ferrous iron in lower-mantle perovskite, *Nature Geoscience*, *1*(10), 684–687, 2008.
- Meade, C., and R. Jeanloz, Static compression of Ca(OH)₂ at room temperature: Observations of amorphization and equation of state measurements to 10.7 GPa, *Geophysical Research Letters*, *17*, 1157–1160, 1990.
- Meade, C., and R. Jeanloz, Deep-focus earthquakes and recycling of water into the Earth's mantle, *Science*, *252*, 68–72, 1991.
- Meade, C., R. Jeanloz, and R. J. Hemley, Spectroscopic and X-ray diffraction studies of metastable crystalline-amorphous transitions in Ca(OH)₂ and serpentine, in *High Pressure Research in Mineral Physics: Application to Earth and Planetary Sciences*, edited by Y. Syono and M. H. Manghnani, pp. 485–492, Terra Scientific Publishing Company, Tokyo and Washington, D.C., 1992.
- Miyagi, L., W. Kanitpanyacharoen, P. Kaercher, K. K. M. Lee, and H. R. Wenk, Slip systems in MgSiO₃ post-perovskite: implications for D'' anisotropy, *Science*, *329*, 1639–1641, 2010.
- Murakami, M., K. Hirose, K. Kawamura, N. Sata, and Y. Ohishi, Post-perovskite phase transition in MgSiO₃, *Science*, *304*(5672), 855–858, 2004.

Bibliography

- Murakami, M., K. Hirose, N. Sata, and Y. Ohishi, Post-perovskite phase transition and mineral chemistry in the pyrolitic lowermost mantle, *Geophysical Research Letters*, 32(3), 2005.
- Nagai, T., T. Hattori, and T. Yamanaka, Compression mechanism of brucite: An investigation by structural refinement under pressure, *American Mineralogist*, 85, 760–764, 2000.
- Nakagawa, T., and P. J. Tackley, Effects of a perovskite-post perovskite phase change near core-mantle boundary in compressible mantle convection, *Geophysical Research Letters*, 31(16), 2004.
- Navrotsky, A., A lesson from ceramics, *Science*, 284, 1788–1789, 1999.
- Navrotsky, A., M. Schoenitz, H. Kojitani, H. W. Xu, J. Z. Zhang, D. J. Weidner, and R. Jeanloz, Aluminum in magnesium silicate perovskite: Formation, structure, and energetics of magnesium-rich defect solid solutions, *Journal of Geophysical Research*, 108(B7), 2330, 2003.
- Ni, S., E. Tan, M. Gurnis, and D. Helmberger, Sharp sides to the African superplume, *Science*, 296, 1850–1852, 2002.
- Nishio-Hamane, D., K. Fujino, Y. Seto, and T. Nagai, Effect of the incorporation of FeAlO₃ into MgSiO₃ perovskite on the post-perovskite transition, *Geophysical Research Letters*, 34(12), 2007.
- Nishio-Hamane, D., Y. Seto, K. Fujino, and T. Nagai, Effect of FeAlO₃ incorporation into MgSiO₃ on the bulk modulus of perovskite, *Physics of the Earth and Planetary Interiors*, 166, 219–225, 2008.
- Oganov, A. R., and S. Ono, Theoretical and experimental evidence for a post-perovskite phase of MgSiO₃ in Earth's D'' layer, *Nature*, 430, 445–448, 2004.
- Oganov, A. R., M. J. Gillan, and G. D. Price, Structural stability of silica at high pressures and temperatures, *Physical Review B*, 71, 064,104, 2005.
- Olsen, J. S., S. S. G. Cousins, L. Gerward, H. Jhans, and B. J. Sheldon, A study of the crystal structure of Fe₂O₃ in the pressure range up to 65 GPa using synchrotron radiation, *Physica Scripta*, 43, 327–330, 1991.
- Ono, S., and A. Oganov, In situ observations of phase transition between perovskite and CaIrO₃-type phase in MgSiO₃ and pyrolitic mantle composition, *Earth and Planetary Science Letters*, 236, 914–932, 2005.

- Ono, S., T. Kikegawa, and Y. Ohishi, High-pressure phase transition of hematite, Fe_2O_3 , *Journal of Physics and Chemistry of Solids*, *65*, 1527–1530, 2004.
- Partin, D. E., and M. O’Keeffe, The crystal structure of $\text{Sr}(\text{OD})_2$, *Journal of Solid State Chemistry*, *119*, 157–160, 1995.
- Prakapenka, V. B., A. Kubo, A. Kuznetsov, A. Laskin, O. Shkurikhin, P. Dera, M. Rivers, and S. Sutton, Advanced flat top laser heating system for high pressure research at GSECARS: application to the melting behavior of germanium, *High Pressure Research*, *28*(3), 225–235, 2008.
- Presnall, D., and J. Hoover, High pressure phase equilibrium constraints on the origin of mid-ocean ridge basalts, in *Magmatic Processes: Physiochemical Principles*, vol. 1, edited by B. Mysen, pp. 75–80, Geochemical Society, 1987.
- Ringwood, A. E., Phase transformations and the constitution of the mantle, *Physics of the Earth and Planetary Interiors*, *3*, 109–155, 1970.
- Ringwood, A. E., *Composition and Petrology of the Earth’s Mantle*, McGraw-Hill, New York, 1975.
- Sata, N., G. Shen, M. L. Rivers, and S. R. Sutton, Pressure-volume equation of state of the high-pressure $B2$ phase of NaCl , *Physical Review B*, *65*, 104,114, 2002.
- Shannon, R. D., Revised effective ionic radii and systematic studies of interatomic distances in halides and chalcogenides, *Acta Crystallographica A*, *A32*, 751–767, 1976.
- Sharma, S. M., and S. K. Sikka, Pressure induced amorphization of materials, *Progress in Materials Science*, *40*, 1–77, 1996.
- Shen, Y., C. J. Wolfe, and S. C. Solomon, Seismological evidence for a mid-mantle discontinuity beneath Hawaii and Iceland, *Earth and Planetary Science Letters*, *214*, 143–151, 2003.
- Shen, Y., R. S. Kumar, M. Pravica, and M. F. Nicol, Characteristics of silicone fluid as a pressure transmitting medium in diamond anvil cells, *Review of Scientific Instruments*, *75*, 4450–4454, 2004.
- Shieh, S. R., T. S. Duffy, A. Kubo, G. Y. Shen, V. B. Prakapenka, N. Sata, K. Hirose, and Y. Ohishi, Equation of state of the postperovskite phase synthesized from a natural $(\text{Mg,Fe})\text{SiO}_3$ orthopyroxene, *Proceedings of the National Academy of Sciences of the United States of America*, *103*(9), 3039–3043, 2006.
- Shim, S.-H., The postperovskite transition, *Annual Review of Earth and Planetary Sciences*, *36*, 569–599, 2008.

Bibliography

- Shim, S.-H., and T. S. Duffy, Constraints on the $P - V - T$ equation of state of MgSiO_3 perovskite, *American Mineralogist*, 85(2), 354–363, 2000.
- Shim, S.-H., and T. S. Duffy, Raman spectra of Fe_2O_3 to 62 GPa: Implications for thermodynamics and phase transformation, *American Mineralogist*, 87, 318–326, 2002.
- Shim, S.-H., T. S. Duffy, and G. Y. Shen, Stability and structure of MgSiO_3 perovskite to 2300-kilometer depth in Earth's mantle, *Science*, 293(5539), 2437–2440, 2001.
- Shim, S.-H., T. S. Duffy, and T. Kenichi, Equation of state of gold and its application to the phase boundaries near the 660-km depth in the mantle, *Earth and Planetary Science Letters*, 203, 729–739, 2002.
- Shim, S.-H., T. S. Duffy, R. Jeanloz, and G. Shen, Stability and crystal structure of MgSiO_3 perovskite to the core-mantle boundary, *Geophysical Research Letters*, 31(10), L10,603, 2004.
- Shim, S.-H., K. Catalli, J. Hustoft, A. Kubo, V. B. Prakapenka, and M. Kunz, Crystal structure and thermoelastic properties of $(\text{Mg}_{0.91}\text{Fe}_{0.09})\text{SiO}_3$ postperovskite up to 135 GPa and 2700 K, *Proceedings of the National Academy of Sciences of the United States of America*, 105(21), 7382–7386, 2008.
- Shim, S.-H., A. Bengtson, D. Morgan, W. Sturhahn, K. Catalli, J. Zhao, M. Lerche, and V. B. Prakapenka, Electronic and magnetic structures of the postperovskite-type Fe_2O_3 – Implications for planetary magnetic records and deep interior transitions, *Proceedings of the National Academy of Sciences of the United States of America*, 106, 5508–5512, 2009.
- Sidorin, I., M. Gurnis, and D. Helmberger, Evidence for a ubiquitous seismic discontinuity at the base of the mantle, *Science*, 286, 1326–1331, 1999.
- Sinmyo, R., K. Hirose, H. S. O'Neill, and E. Okunishi, Ferric iron in Al-bearing post-perovskite, *Geophysical Research Letters*, 33(12), L12S13, 2006.
- Sinmyo, R., K. Hirose, D. Nishio-Hamane, Y. Seto, K. Fujino, N. Sata, and Y. Ohishi, Partitioning of iron between perovskite/postperovskite and ferropericlasite in the lower mantle, *Journal of Geophysical Research*, 113, B11,204, 2008.
- Speziale, S., C. S. Zha, T. S. Duffy, R. J. Hemley, and H. K. Mao, Quasihydrostatic compression of magnesium oxide to 52 GPa: Implications for the pressure-volume-temperature equation of state, *Journal of Geophysical Research*, 106(B1), 515–528, 2001.

- Speziale, S., A. Milner, V. E. Lee, S. M. Clark, M. P. Pasternak, and R. Jeanloz, Iron spin transition in Earth's mantle, *Proceedings of the National Academy of Sciences of the United States of America*, 102(50), 17,918–17,922, 2005.
- Stackhouse, S., J. P. Brodholt, and G. D. Price, Electronic spin transitions in iron-bearing MgSiO₃ perovskite, *Earth and Planetary Science Letters*, 253(1-2), 282–290, 2007.
- Stixrude, L., Structure and sharpness of phase transitions and mantle discontinuities, *Journal of Geophysical Research*, 102, 14,835–14,852, 1997.
- Stixrude, L., R. J. Hemley, Y. Fei, and H.-K. Mao, Thermoelasticity of silicate perovskite and magnesiowüstite and stratification of Earth's mantle, *Science*, 257, 1099–1101, 1992.
- Stunff, Y. L., C. W. W. Jr., and B. Romanowicz, *P'P'* precursors under Africa: Evidence for mid-mantle reflectors, *Science*, 270, 74–78, 1995.
- Sturhahn, W., CONUSS and PHOENIX: Evaluation of nuclear resonant scattering data, *Hyperfine Interactions*, 125(1-4), 149–172, 2000.
- Sturhahn, W., and J. M. Jackson, Geophysical applications of nuclear resonant spectroscopy, in *Advances in High-Pressure Mineralogy*, edited by E. Ohtani, pp. 157–174, The Geological Society of America, 2007.
- Sturhahn, W., J. M. Jackson, and J. F. Lin, The spin state of iron in minerals of Earth's lower mantle, *Geophysical Research Letters*, 32(12), L12,307, 2005.
- Sun, L., A. Ruoff, and G. Stupian, Convenient optical pressure gauge for multimegabar pressures calibrated to 300 GPa, *Applied Physics Letters*, 86, 014,103, 2005.
- Takemura, K., Evaluation of the hydrostaticity of a helium-pressure medium with powder X-ray diffraction techniques, *Journal of Applied Physics*, 89, 662–668, 2001.
- Tangeman, J. A., B. L. Phillips, A. Navrotsky, J. K. R. Weber, A. D. Hixson, and T. S. Key, Vitreous forsterite (Mg₂SiO₄): Synthesis, structure, and thermochemistry, *Geophysical Research Letters*, 28(13), 2517–2520, 2001.
- Tateno, S., K. Hirose, N. Sata, and Y. Ohishi, Phase relations in Mg₃Al₂Si₃O₁₂ to 180 GPa: Effect of Al on post-perovskite phase transition, *Geophysical Research Letters*, 32(15), 2005.
- Tateno, S., K. Hirose, N. Sata, and Y. Ohishi, Determination of the post-perovskite phase transition boundary up to 4400 K and implications for the thermal structure in D'' layer, *Earth and Planetary Science Letters*, 277, 130–136, 2009.

Bibliography

- Trampert, J., F. Deschamps, J. Resovsky, and D. Yuen, Probabilistic tomography maps chemical heterogeneities throughout the lower mantle, *Science*, *306*, 853–856, 2004.
- Tschauner, O., B. Kiefer, and H. Z. Liu, Crystal chemical aspects and polymorphism in post-perovskite, *Geochimica Et Cosmochimica Acta*, *71*, A1039–A1039, 2007.
- Tsuchiya, T., First-principles prediction of the $P - V - T$ equation of state of gold and the 660-km discontinuity in Earth's mantle, *Journal of Geophysical Research*, *108*(B10), 2462, 2003.
- Tsuchiya, T., J. Tsuchiya, K. Umemoto, and R. A. Wentzcovitch, Phase transition in MgSiO_3 perovskite in the Earth's lower mantle, *Earth and Planetary Science Letters*, *224*(3-4), 241–248, 2004.
- Tsuchiya, T., R. M. Wentzcovitch, C. R. S. da Silva, and S. de Gironcoli, Spin transition in magnesiowüstite in Earth's lower mantle, *Physical Review Letters*, *96*, 198,501, 2006.
- Umemoto, K., R. M. Wentzcovitch, Y. G. Yu, and R. Requist, Spin transition in $(\text{Mg,Fe})\text{SiO}_3$ perovskite under pressure, *Earth and Planetary Science Letters*, *276*, 198–206, 2008.
- van der Hilst, R. D., S. Widiyantoro, and E. R. Engdahl, Evidence for deep mantle circulation from global tomography, *Nature*, *386*, 578–584, 1997.
- van der Hilst, R. D., M. V. de Hoop, P. Wang, S.-H. Shim, P. Ma, and L. Tenorio, Seismostratigraphy and thermal structure of Earth's core-mantle boundary region, *Science*, *315*, 1813–1817, 2007.
- Van der Voo, R., W. Spakman, and H. Bijwaard, Mesozoic subducted slabs under Siberia, *Nature*, *397*, 246–249, 1999.
- Vankó, G., T. Neisius, G. Molnár, F. Renz, S. Kárpáti, A. Shukla, and M. F. de Groot, Probing the 3d spin momentum with X-ray emission spectroscopy: The case of molecular-spin transitions, *Journal of Physical Chemistry B*, *110*, 11,647–11,653, 2006.
- Vanpeteghem, C. B., R. J. Angel, N. L. Ross, S. D. Jacobsen, D. P. Dobson, K. D. Litasov, and E. Ohtani, Al, Fe substitution in the MgSiO_3 perovskite structure: A single-crystal X-ray diffraction study, *Physics of the Earth and Planetary Interiors*, *155*, 96–103, 2006a.
- Vanpeteghem, C. B., J. Zhao, R. J. Angel, N. L. Ross, and N. Bolfan-Casanova, Crystal structure and equation of state of MgSiO_3 perovskite, *Geophysical Research Letters*, *33*, L03,306, 2006b.

- Wittlinger, J., R. Fischer, S. Werner, J. Schneider, and H. Schulz, High-pressure study of hcp-argon, *Acta Crystallographica B*, 53(5), 745–749, 1997.
- Wood, B. J., M. J. Walter, and J. Wade, Accretion of the Earth and segregation of its core, *Nature*, 441, 825–833, 2006.
- Wookey, J., S. Stackhouse, J. M. Kendall, J. Brodholt, and G. D. Price, Efficacy of the post-perovskite phase as an explanation for lowermost-mantle seismic properties, *Nature*, 438(7070), 1004–1007, 2005.
- Wyssession, M. E., T. Lay, J. Revenaugh, Q. Williams, E. J. Garnero, R. Jeanloz, and L. H. Kellogg, The D'' discontinuity and its implications, in *The Core-Mantle Boundary Region*, edited by M. Gurnis, M. E. Wyssession, E. Knittle, and B. A. Buffett, pp. 273–297, American Geophysical Union, Washington, D.C., 1998.
- Xu, W., O. Naaman, G. Rozenberg, M. Pasternak, and R. Taylor, Pressure-induced breakdown of a correlated system: The progressive collapse of the Mott-Hubbard state of RFeO₃, *Physical Review B*, 64, 094,411, 2001.
- Xu, W., C. Lithgow-Bertelloni, L. Stixrude, and J. Ritsema, The effect of bulk composition and temperature on mantle seismic structure, *Earth and Planetary Science Letters*, 275, 70–79, 2008.
- Xu, Y., C. McCammon, and B. T. Poe, The effect of alumina on the electrical conductivity of silicate perovskite, *Science*, 282, 922–924, 1998.
- Yagi, T., K. Okabe, N. Nishiyama, A. Kubo, and T. Kikegawa, Complicated effects of aluminum on the compressibility of silicate perovskite, *Physics of the Earth and Planetary Interiors*, 143-144, 81–91, 2004.
- Zha, C. S., H. K. Mao, and R. J. Hemley, Elasticity of MgO and a primary pressure scale to 55 GPa, *Proceedings of the National Academy of Sciences of the United States of America*, 97(25), 13,494–13,499, 2000.
- Zhang, F. W., and A. R. Oganov, Valence state and spin transitions of iron in Earth's mantle silicates, *Earth and Planetary Science Letters*, 249(3-4), 436–443, 2006.